Molecular Structure of Solid-Confined Ionic Liquids and Their Applications as Media Lubricants in Hard Disk Drives

by

Bingchen Wang

B.S. in Applied Chemistry, Dalian University of Technology, 2014

Master's degree in Chemical Engineering, University of Florida, 2016

Submitted to the Graduate Faculty of the

Swanson School of Engineering in partial fulfillment

of the requirements for the degree of

Doctor of Philosophy

University of Pittsburgh

2021

UNIVERSITY OF PITTSBURGH

SWANSON SCHOOL OF ENGINEERING

This dissertation was presented

by

Bingchen Wang

It was defended on

March 12, 2021

and approved by

Dr. Susan Fullerton, Associate Professor, Department of Chemical and Petroleum Engineering

Dr. Haitao Liu, Professor, Department of Chemistry

Dr. Sachin Velankar, Professor, Department of Chemical and Petroleum Engineering

Dissertation Director: Dr. Lei Li, Associate Professor, Department of Chemical and Petroleum Engineering

Copyright © by Bingchen Wang

2021

Molecular Structure of Solid-Confined Ionic Liquids and Their Applications as Media Lubricants in Hard Disk Drives

Bingchen Wang, PhD

University of Pittsburgh, 2021

Media lubricants are critical to the reliability of hard disc drives (HDDs). Ionic liquids (ILs) are promising candidates as the next-generation media lubricants because of their excellent physiochemical properties. Both the fundamental understandings of the interfacial molecular structure at the IL/solid interfaces and the novel designs of the IL chemical structures are critical to the application of ILs as media lubricants.

First, we have investigated the molecular structure of mica-confined ILs. Experimental evidence from ATR-FTIR, contact angle measurement, and AFM shows that tuning relative humidity (RH) is an effective approach manipulating the molecular arrangement and macroscopic wettability of ILs on mica. More water adsorbs on mica at higher RH, which mobilizes the surface K^+ and consequently initiates the layering of IL cations/anions. Additionally, unique quantized growths of mica-confined ILs with various cation alkyl chain lengths have been directly observed under AFM. The IL nanofilms initially cover more solid surface areas at the constant thickness of 2 monolayers (ML) until a quantized thickness increase by 2 ML. A double-layer building block of IL cations/anions is proposed. Time-dependent AFM results reveal the slower spreading of ILs with longer alkyl chains due to the stronger dispersive interactions.

Second, we have assessed the potential of nanometer-thick ILs as media lubricants. The TGA results indicate the commercially-available [Bmim][FAP] has higher thermal stability than the state-of-the-art perfluoropolyether (PFPE) lubricants. More importantly, AFM surface

roughness results demonstrate that ILs have much lower ML thickness than PFPEs on carbon overcoat (COC) due to the smaller molecular sizes, which provides the opportunity to scale down the lubricant thickness and increase the areal density. Then a fluorinated IL (FIL) with a highly fluorinated cation alkyl chain has been synthesized to realize a reduced surface tension that is comparable to PFPEs. To enhance the bonding of ILs on COC and further reduce the surface tension, we have synthesized a novel IL, HFIL-OH, containing a hydroxyl endgroup and a fluorinated alkyl chain in the cation and a highly fluorinated anion. The successful development of the IL lubricants is a major step forward for ILs to be utilized as the next-generation media lubricants.

Table of Contents

Preface xix

1.0 Introduction 1

2.0 From Molecular Arrangement to Macroscopic Wetting of Ionic Liquids on the Mica Surface: Effect of Humidity 5

2.1 Introduction 5

2.2 Experimental Section 8

2.2.1 Materials 8

2.2.2 Relative Humidity (RH) Control Using Saturated Salt Solutions 9

2.2.3 Fabrication and Topography Characterization of the Nanoscale BMIM-FAP/Mica 10

2.2.4 Other Characterizations 10

2.3 Results and Discussion 12

2.3.1 Water Adsorption under Various RH 12

2.3.2 Macroscopic Wettability under Various RH 14

2.3.3 Molecular Arrangement under Various RH 17

2.4 Conclusions 21

3.0 Direct Observations of the Double-Layering Molecular Structures of Mica-Confined Ionic Liquids 23

3.1 Introduction 23

3.2 Experimental Section 25

3.2.1 Materials 25

3.2.2 Thin Film Fabrication 26

3.2.3 AFM Characterization 27

3.2.4 Surface Tension Measurement 28

3.3 Results and Discussion 28

3.3.1 Quantized Growth of [Emim][FAP] on Mica 28

3.3.2 Double-Layering Interfacial Molecular Structure 30

3.3.3 Different Spreading Kinetics of ILs on Mica 39

3.4 Conclusions 46

4.0 Nanometer-Thick Fluorinated Ionic Liquid Films as Lubricants in Data-Storage Devices 48

4.1 Introduction 48

4.2 Experimental Section 51

4.2.1 Materials 51

4.2.2 Fabrication of Nanometer-Thick Films 52

4.2.3 Other Characterizations 54

4.3 Results and Discussion 58

4.3.1 Monolayer Thickness Determined by Surface Roughness 58

4.3.2 Monolayer Thickness Determined by Friction 62

4.4 Conclusions 66

5.0 Highly Fluorinated Ionic Liquid Films as Nanometer-Thick Media Lubricants for Hard Disk Drives 67

5.1 Introduction 67

5.2 Experimental Section 69

5.2.1 Chemicals and Materials 69

5.2.2 Synthesis of FIL 70

5.2.3 Nanofilm Fabrication and Thickness Measurement 71

5.2.4 Characterization of FIL 72

5.2.5 Assessment of Lubrication Performance 73

5.3 Results and Discussion 74

5.3.1 Characterization of FIL 74

5.3.2 Reduced Surface Tension of FIL 76

5.3.3 Nanometer-Thick FIL as Media Lubricant 78

5.4 Conclusions 86

6.0 Novel Highly Fluorinated Ionic Liquid with Functional Endgroups as Nanometer-Thick Media Lubricants for Hard Disk Drives 88

6.1 Introduction 88

6.2 Experimental Section 90

6.2.1 Chemicals and Materials 90

6.2.2 Characterization of IL Products 91

6.2.3 Dipcaoting and Ellipsometry 92

6.2.4 Assessment of Nanometer-Thick Lubricants 92

6.3 Results and Discussion 93

6.3.1 Synthesis and Characterizations of ILs 93

6.3.2 Reduced Surface Tension and Enhanced Bonding 98

6.3.3 Nanometer-Thick ILs as Media Lubricant 102

6.4 Conclusions 106

7.0 Summary and Future Work 107

7.1 Summary 107

7.1.1 Molecular Structure of Solid-Confined ILs 107

7.1.2 Nanometer-Thick ILs as Novel Media Lubricants 108

7.2 Future Work 110

7.2.1 Molecular Structure of Solid-Confined ILs 110

7.2.2 Nanometer-Thick ILs as Novel Media Lubricants 111

Appendix A 3D-Printed Repeating Re-Entrant Topography to Achieve On-Demand Wettability and Separation 112

Appendix A.1 Introduction 112

Appendix A.2 Experimental Section 114

Appendix A.2.1 Fabrication of the Re-Entrant Structures 114

Appendix A.2.2 Modification of Surface Chemistry 115

Appendix A.2.3 Fabrication of the Holder for the Separation Membrane 115

Appendix A.2.4 Chemicals and Materials 115

Appendix A.2.5 Imaging 116

Appendix A.2.6 Contact Angle Measurement 116

Appendix A.3 Results and Discussion 117

Appendix A.3.1 Design and Fabrication of the Surface Texture 117

Appendix A.3.2 On-Demand Wettability on the Single Re-Entrant Surface 119

Appendix A.3.3 Enhanced Water Repellency on the Repeating Re-Entrant Surface 121

Appendix A.3.4 On-Demand Separation by the Repeating Re-Entrant Membrane 125

Appendix A.4 Conclusions 128

Appendix B Uncovering the Underlying Mechanisms of the Fouling in Maleic Anhydride Condensers 130

Appendix B.1 Introduction 130

Appendix B.2 Experimental Section 132

Appendix B.2.1 Materials 132

Appendix B.2.2 Modification of Surface Chemistry 133

Appendix B.3 Results and Discussions 135

Appendix B.3.1 Mechanisms of Fouling.....135

Appendix B.3.2 Surface Engineering 138

Appendix B.4 Conclusions 142

Bibliography 143

List of Tables

Table 1. RH of various saturated salt solutions 9

Table 2. Physical properties of BMIM-FAP 11

Table 3. Surface tension values of the ILs 35

Table 4. RMS surface roughness results of the three IL nanofilms fabricated from the concentration of 0.75 g/L at various lead time 42

Table 5. Chemical compositions of FIL 75

Table 6. Surface tension (γ) of FIL, [Hmim][NTf_2], Zdol, and Ztetraol at RT 77

Table 7. Surface tension (γ) of FIL-OH and HFIL-OH at RT, with [Bmim][FAP], Zdol and Ztetraol as control 99

Appendix Table 1. Chemical compositions of the alloys by energy-dispersive X-ray (EDX) spectroscopy (15kV accelerating voltage) 133

Appendix Table 2. Roll-off angles of maleic anhydride drops on Monel with different surface textures 141

List of Figures

Figure 1. XPS of freshly cleaved mica surface under different RH. (a) Survey scan. (b) High-resolution C1s spectra..... 13

Figure 2. ATR-FTIR spectrum of mica surfaces under various RH. 14

Figure 3. ATR-FTIR spectrum of mica surfaces under various RH. 15

Figure 4. AFM images and line profile of [Bmim][FAP] on freshly cleaved mica. (a) at RH=20%, (b) at RH=35%, (c) at RH=50%, and (d) RH=99%. Images are 20 μm × 20 μm and the height bar is 20 nm. 19

Figure 5. AFM images and line profile of [Bmim][FAP] on freshly cleaved mica..... 19

Figure 6. The proposed mechanisms illustrating the effect of adsorbed water on the molecular arrangement and wetting of ILs on the mica surface. (a) Dry mica (Top). (b) Wet mica (bottom). 20

Figure 7. 3D chemical structures of the imidazolium cations with various alkyl chain length and the [FAP] anion. Energy minimization was performed using the MMFF94 force field. 26

Figure 8. (a) AFM image and the corresponding line profile of the fresh mica surface. The scan area is 2 μm by 2 μm, and the inset scale bar is for the z-direction. (b) Fabrication of IL nanofilms on mica by dipcoating. 27

Figure 9. AFM images and their corresponding line profiles of mica-confined [Emim][FAP] fabricated from the concentration of (a) 0.25 g/L, (b) 0.5 g/L, (c) 0.75 g/L, (d) 1 g/L, and (e) 1.5 g/L. The AFM scan areas are 10 μm by 10 μm, and the inset scale bar is for the z-direction. The x-axis and y-axis for the line profiles are the distance along

the cut in the horizontal direction (μm) and the height in the vertical direction (nm), respectively. 29

Figure 10. AFM images and their corresponding line profiles of mica-confined [Bmim][FAP] fabricated from the concentration of (a) 0.25 g/L, (b) 0.75 g/L, (c) 1 g/L, (d) 1.5 g/L, and (e) 2 g/L. The AFM scan areas are 10 μm by 10 μm, and the inset scale bar is for the z-direction. The x-axis and y-axis for the line profiles are the distance along the cut in the horizontal direction (μm) and the height in the vertical direction (nm), respectively. 32

Figure 11. AFM images and their corresponding line profiles of mica-confined [Hmim][FAP] fabricated from the concentration of (a) 0.25 g/L, (b) 0.5 g/L, (c) 0.75 g/L, and (d) 1 g/L. The AFM scan areas are 10 μm by 10 μm, and the inset scale bar is for the z-direction. The x-axis and y-axis for the line profiles are the distance along the cut in the horizontal direction (μm) and the height in the vertical direction (nm), respectively. 33

Figure 12. AFM images and their corresponding line profiles of mica-confined [Hmim][FAP] fabricated from the concentration of (a) 0.25 g/L, (b) 0.5 g/L, (c) 0.75 g/L, and (d) 1 g/L. The scans were taken 1 week after the sample fabrications, and the relative humidity (RH) was higher than 30% the whole time. The AFM scan areas are 10 μm by 10 μm, and the inset scale bar is for the z-direction. The x-axis and y-axis for the line profiles are the distance along the cut in the horizontal direction (μm) and the height in the vertical direction (nm), respectively..... 36

Figure 13. Double-layering interfacial structure of IL molecules on the mica surface. 39

Figure 14. AFM images and their corresponding line profiles of time-dependent nanofilms of [Emim][FAP] fabricated from the concentration of 0.75 g/L. The RH was lower than 20% the whole time. The AFM scan areas are 10 μm by 10 μm, and the inset scale bar is for the z-direction. The x-axis and y-axis for the line profiles are the distance along the cut in the horizontal direction (μm) and the height in the vertical direction (nm), respectively. 41

Figure 15. AFM images and their corresponding line profiles of time-dependent nanofilms of (a) [Bmim][FAP] and (b) [Hmim][FAP] fabricated from the concentration of 0.75 g/L. All AFM scan areas are 10 μm by 10 μm, and the inset scale bars are for the z-direction. The x-axis and y-axis for the line profiles are the distance along the cut in the horizontal direction (μm) and the height in the vertical direction (nm), respectively. 44

Figure 16. AFM images and their corresponding line profiles of mica-confined [Hmim][FAP] fabricated from the concentration of 0.75 g/L. The scans were taken 1 week and 3 weeks after the sample fabrications, and the RH was lower than 20% the whole time. The AFM scan areas are 10 μm by 10 μm, and the inset scale bar is for the z-direction. 45

Figure 17. Chemical structures of [Bmim][FAP] and Z-tetraol. 52

Figure 18. Nanofilm thickness of [Bmim][FAP] and Z-tetraol on COC at various concentrations. 54

Figure 19. Friction traces of (a) Z-tetraol and (b) [Bmim][FAP] with varying thicknesses on COC. One trial is randomly selected to be displayed for each nanometer-thick film. 56

Figure 20. TGA results of the bulk IL and PFPE. 57

Figure 21. RMS of the nanometer-thick films with varying thicknesses on COC. 58

Figure 22. AFM images of (a) bare COC, (b) [Bmim][FAP], and (c) Z-tetraol with different thicknesses on COC. 60

Figure 23. COF of the nanometer-thick films with varying thicknesses on COC. 63

Figure 24. COF of the ML of Z-tetraol and [Bmim][FAP] on COC at different duration, normal load, and maximum linear speed. Standard testing parameters are 50 cycles, 10 mN, and 0.2 cm/s. 63

Figure 25. Bonded ratio of the nanometer-thick films on COC. 65

Figure 26. COF of the nanometer-thick films before and after Vertrel washing. 65

Figure 27. ^{1}H NMR spectrum of 1-1H,1H,2H,2H-perfluorohexyl-3-methylimidazolium bis(trifluoromethylsulfonyl)imide. The peak assignments are labeled. 75

Figure 28. TGA results of bulk Ztetraol and FIL. 76

Figure 29. CA results on the nanometer-thick FIL films. 78

Figure 30. Surface roughness results of the nanometer-thick lubricants on COC. The insets are AFM images of the FIL nanofilms at various thicknesses (10 µm by 10 µm scan size). 81

Figure 31. 2D AFM images and the line profiles of nanometer-thick FIL on COC at (a) 0.72 nm, (b) 0.9 nm, (c) 1.1 nm, (d) 1.39 nm, (e) 1.75 nm. The scan sizes are 10 µm by 10 µm. 82

Figure 32. Estimated dimensions of the FIL cation and anion from van der Waals radii... 83

Figure 33. Friction results of the nanometer-thick lubricants on COC..... 84

Figure 34. Thicknesses of the nanometer-thick FIL lubricants on COC before and after Vertrel XF washing. 86

Figure 35. TOC figure. 87

Figure 36. ^{1}H NMR spectrum of (a) FIL-OH and (b) HFIL-OH. The peak assignments are labeled. 97

Figure 37. TGA results of bulk FIL-OH and HFIL-OH. Ztetraol and FIL are used as control. 98

Figure 38. Nanofilm thicknesses of (a) FIL-OH and (b) HFIL-OH before and after Vertrel washing. FIL nanofilms and bare COC are used as reference. 101

Figure 39. CA results on the FIL-OH and HFIL-OH nanofilms. 101

Figure 40. Surface roughness results of the nanometer-thick lubricants of (a) FIL-OH and (b) HFIL-OH on COC. The insets are AFM images of the IL nanofilms at various thicknesses. 104

Figure 41. Friction results of the nanometer-thick FIL-OH and HFIL-OH lubricants on COC. 105

Appendix Figure 1. Design and fabrication of the re-entrant surface. (a) Physics of a liquid being repelled at the re-entrant structure. (b) Optical microscope image of the top view of the single re-entrant surface. (c) Tilted SEM image of the single re-entrant surface. (d) Tilted SEM image highlighting the details of the re-entrant structure. 119

Appendix Figure 2. On-demand wettability on the single re-entrant surface. The dotted line indicates the 30º re-entrant angle ($\theta Re - etrant$) in the current design. A sharp increase of the CA on the single re-entrant surface ($\theta Apparent$) occurs when the CA on the flat surface (θLS) is higher than $\theta Re - entrant$. The insets illustrate the

physics of liquids wetting the re-entrant surface when $\theta LS < \theta Re - entrant$, and being repelled by the re-entrant surface when $\theta LS > \theta Re - entrant$. 121

Appendix Figure 3. Repeating re-entrant topography inducing more robust surface wettability. (a) Cross-section view of the microscale repeating re-entrant structure. (b) Tilted SEM image of the repeating re-entrant surface. (c) Optical microscope image of the top view of the repeating re-entrant surface. (d) The repeating re-entrant surface repelling a 5 μL water drop. (e) A repeating re-entrant surface fully covered with water immediately followed by WCA measurement with a 20 μL drop on the post-rinsing surface. (f) A repeating re-entrant surface submerged in water at 0.25 cm, 1 cm, and 2 cm deep for 1 minute, and at 0.5 cm deep for 30 min, immediately followed by WCA measurements with 5 μL drops. 124

Appendix Figure 4. Optical microscope images of the repeating re-entrant surface. (a) Top layer. (b) Bottom layer. 125

Appendix Figure 5. On-demand separation enabled by the re-entrant topography. (a) Separation of liquid mixture L1/L2 with the re-entrant membrane. (b) CAD image of the 3D cross-section view of the repeating re-entrant membrane. (c) 2D cross-section analysis of the repeating re-entrant membrane. (d) Optical microscope images of the front and bottom of the re-entrant membrane. (e) Separation of bromobenzene and water (θLS: 19.3°/71.0°), chlorobenzene and water (θLS: 19.6°/71.0°), and bromobenzene and ethylene glycol (θLS: 19.3°/52.6°) with the repeating re-entrant membrane ($\theta Re - entrant = 45°$). 127

Appendix Figure 6. Separation of partially miscible liquid mixtures with the repeating re-entrant membrane. (a) Design of a 3D-printed repeating re-entrant separation

membrane fitted into a 3D-printed liquid container. (b) Separation of partially miscible benzyl alcohol and DI water using the repeating re-entrant membrane.. 128

Appendix Figure 7. TOC figure. 129

Appendix Figure 8. Severe fouling in the maleic anhydride condenser in Lubrizol. 131

Appendix Figure 9. In-situ interface characterization apparatus. 134

Appendix Figure 10. Evolution of the maleic anhydride-stainless steel interface at 102 °C. 135

Appendix Figure 11. ^{1}H NMR spectra of the solid particles (as shown in Figure S8) dissolved in DMSO-d_6. 136

Appendix Figure 12. The melting of the solid particles from Figure S8. 136

Appendix Figure 13. Possible reaction scheme to form maleic acid. 137

Appendix Figure 14. Proposed fouling mechanism of maleic anhydride condenser. 138

Appendix Figure 15. No roll-off of the maleic anhydride droplet at 88° tilting angle (100 °C). 139

Appendix Figure 16. Effect of dynamic contact angles on the roll-off angle. 139

Appendix Figure 17. Optical microscope images of as-received, polished, ground, and machined Monel. 140

Preface

First of all, I would like to sincerely thank my advisor, Dr. Lei Li, for his instruction, support, patience, and encouragement in my research and life during the past five years. I would like to thank my committee members, Dr. Susan Fullerton, Dr. Haitao Liu, and Dr. Sachin Velankar, for the technical advice on my dissertation. I would also like to thank all my colleagues, Dr. Xiao Gong, Dr. Andrew Kozbial, Catherine Moran, Anne Lertola, Yihan Song, Fan Yang, Aigerim Baimoldina, Dr. Corey Clifford, Darren Lin, and all my co-authors of my publications, for their time and help on my research. Additionally, I would like to thank Dr. Susheng Tan, Dr. Jun Chen, Dr. Daniel Lamont, Mike McDonalds, and Dr. Joel Gillespie for their help in teaching me how to operate the instruments in NFCF, and Patricia Park and Rita Leccia for helping with purchasing orders on chemicals and labware. Last but not least, I would like to thank my parents for providing me the opportunity to go to graduate school in the United States, and my girlfriend Shen for her endless support in our daily lives. Finally, I would like to dedicate the dissertation to my family.

My dissertation is originated significantly based on my first-author publications. The publications have been cited appropriately.

1.0 Introduction

Ionic liquids (ILs) are salts composed of bulky and large organic cations and anions. Unlike common inorganic salts, ILs are in the thermodynamically favorable liquid phase at room temperature (RT) due to the Coulombic attractions disrupted and the lattice structure not formed. ILs have attracted extensive research interests because of their exceptional physiochemical properties. They have high thermal stability, extremely low volatility, wide liquidus range, excellent capability of dissolving materials,[1-3] making them ideal candidates for applications in separations, solvents for chemical synthesis, etc.[4-8] The interface between ILs and solids are especially crucial to many promising applications, such as electrolytes for energy storage devices,[9, 10] lubricants for nano- and microelectromechanical systems (NEMS/MEMS) and hard disk drives (HDD),[11-15] absorbents for CO_2 capture,[16, 17] and green catalysis.[18, 19] Since the IL/solid interface always plays a fundamental role in these applications, it is crucial to study the molecular structure and the potential industrial applications of ILs confined to solid surfaces. As the model solid, muscovite mica has been frequently utilized in the study of IL wettings due to its well-defined surface chemistry, atomically smooth surface, broad applications, and availability.[20-25] Atkin et al. found that extended solid-like layering of ILs on the mica surface based on AFM force-distance study.[20] Perkin et al. used surface force apparatus (SFA) to study the oscillation distances from the squeeze-out of ion pairs for $[C_nMIm][NTf_2]$ between two mica sheets, and concluded that ILs form layered structure on the mica surface.[26-28] Bovio et al. reported a different observation that there is only solid-like layering for $[Bmim][NTf_2]$ on mica.[29] Later, Yokota et al. detected inhomogeneous layering structures of $[Bmim][NTf_2]$ and $[Bmim][BF_4]$ at the IL/mica interface using frequency-modulation AFM (FM-AFM).[30] In contrast, Deyko et al. reported that complete dewetting occurs

when ILs are deposited on the mica surface in high vacuum based on X-ray Photoelectron Spectroscopy (XPS) study.[31] Liu et al. noticed the coexistence of the liquid phase and the stable solid-like phase of [Bmim][PF_6] on the mica surface at room temperature (RT) under tapping mode AFM.[32] It is unclear why ILs exhibit different molecular arrangement on the mica surface, i.e., layering vs. dewetting droplets, based on the extensive controversy in various previous reports. Further research is essential to uncover the comprehensive picture and the underlying mechanisms of the interfacial molecular arrangement of cations and anions of mica-confined ILs.

The application of ILs as the next-generation boundary lubricants is especially promising among all the potential applications that involve the IL/solid interfaces. The physical contact between adjacent solid surfaces has been a huge concern when operating nanoscale devices with contacting components during operation, e. g., HDD and NEMS/MEMS, as it could cause the failure of the devices.[33-35] The use of nanometer-thick boundary lubricants on solid surfaces to reduce friction and wear is critical to the efficiency and reliability of these devices.[36, 37] For instance, a lower thickness of the lubricant nanofilm is desired to achieve higher areal density for HDD. Additionally, the lubricants should have excellent tribological properties, i.e., low surface tension, and load-carrying and self-healing capabilities.[37] The lubricants should also have high thermal stability due to the heating from tribology contacts and the increasing need for heated-assisted magnetic recording (HAMR).[11] Compared to the state-of-the-art media lubricant, perfluoropolyether (PFPE), Ionic liquids (ILs) are promising candidates for the next-generation media lubricants for HDD due to their excellent physiochemical properties, relatively low costs, and much smaller molecular sizes that provide the opportunity to reduce the lubricant thicknesses.[1-3, 11-13, 15, 35, 38] There are very limited previous reports on the applications of ILs as lubricants for data storage devices. Palacio et al. studied [Bmim][PF_6] and [Bmim][$OctSO_4$] as

ultrathin lubricants for potential applications in HDDs because of the excellent electrical and thermal conductivity of the ILs.[35, 39-41] Hatsuda et al. investigated the lubrication of magnetic media using thin DBU- and TBD-based protic ILs.[42, 43] Gong et al. demonstrated the potential of nanometer-thick ILs with fluorinated tris(pentafluoroethyl)trifluorophosphate ([FAP]) anions for lubrication in heat-assisted magnetic recording (HAMR).[11] Nonetheless, to date, no major breakthroughs on reducing the nanofilm thicknesses and enhancing the tribological performances have been made that could lead to the next-generation IL media lubricants.

Both the fundamental understandings of the molecular structures at the IL/solid interfaces and the novel designs of the molecular structure of IL lubricants are critical to the application of ILs as next-generation media lubricants. The current dissertation consists of two major parts. The first part aims to uncover the detailed molecular structure of mica-confined ILs. The second part aims to demonstrate the applications of ILs as media lubricants in hard disk drives. Chapter 2 provides experimental evidence that the molecular arrangement and the macroscopic wettability of ILs on the mica surface can be affected by RH and discusses the mechanism of the water-enabled ion exchange between K^+ and the IL cation and the resulting layering of ILs. Chapter 3 reports direct observations of unusual quantized growths of mica-confined ILs, a double-layer molecular structure of IL cations and anions, and the spreading kinetics for ILs with various alkyl chain lengths. Chapter 4 indicates the potential of the commercially-available [Bmim][FAP] as novel media lubricants due to its higher thermal stability and lower monolayer (ML) thickness. Chapter 5 shows the successful synthesis of a novel fluorinated IL containing a highly fluorinated cation alkyl chain and the reduction of the surface tension of the IL lubricant. Chapter 6 highlights the successful development of a novel IL lubricant with a hydroxyl endgroup and a fluorinated alkyl chain in the cation and a highly fluorinated anion, and demonstrates the significant reduction

in the surface tension and the enhanced bonding on carbon overcoat (COC). Besides, Appendix A reports a novel repeating re-entrant topography that can achieve on-demand wettability and separation by two-photon polymerization 3D-printing, and Appendix B uncovers the governing mechanisms of the fouling in maleic anhydride condensers and provides the resolutions.

2.0 From Molecular Arrangement to Macroscopic Wetting of Ionic Liquids on the Mica Surface: Effect of Humidity

The material in this chapter is based upon the published work *Langmuir* 2018, 34, 40, 12167–12173.[44]

2.1 Introduction

ILs have many potential applications because of their exceptional physiochemical properties.[4, 45] Among those, the applications at the liquid-solid interface, including lubrication[11, 12, 46], catalysis[47], and energy storage[48], are especially promising. In these applications, the wetting of ILs on the solid substrate is essential to the performance. For example, ILs are promising nanometer-thick media lubricants for HAMR[11, 49] and Gong *et al.*[11] recently showed that better wettability of ILs will reduce the friction. In catalysis application, immobilization of ILs on the silica nanoparticles is required[50] and the good wettability of ILs on the solid support is also critical to the success of the process. ILs are promising electrolytes for super-capacitors due to their broad electrochemical window, low volatility and non-flammability [51] Here the double-layer capacitance is proportional to the electrode/IL interfacial area. To increase the interfacial area and thus increase the capacitance, nanoporous carbon electrodes are being utilized now[51]. However, if the wettability of ILs on the electrode surface is poor, the desired increase of the capacitance will not be achieved. Clearly, manipulating the molecular arrangement of ILs on a solid surface is crucial to optimize the wettability of ILs. As the model solid, mica has been extensively utilized in the study of ILs

due to its well-defined surface chemistry, atomic flatness and availability.[20-25] Atkin *et al.* found that there is extended layering of ILs on the mica surface based on AFM force-distance profiles.[20] Liu *et al.* and Bovio *et al.* reported coexistence of droplet and layering structure of ILs on the mica surface by AFM topography analysis, respectively.[21, 22] Using surface force apparatus, Perkin *et al.* concluded that ILs form layered structure on the mica surface.[25] Yokota *et al.* observed extended layering structure of ILs on the mica surface by frequency-modulation AFM.[23] In contrast, Deyko *et al.* reported that complete dewetting occurs when ILs are deposited on the mica surface in high vacuum based on X-ray Photoelectron Spectroscopy (XPS) study.[31] Recent simulation results also indicated the layering structure of ILs on the mica surface.[24] It is not clear why ILs exhibit different molecular arrangement on the mica surface, i.e., layering vs. dewetting droplets, and further research is still required to uncover the mechanisms.[52, 53] It is worth noting that even for the same IL, i.e., 1-butyl-3-methylimidazolium bis(trifluoromethylsulfonyl)imide, different research groups[12, 31] reported different results, which indicates some key parameter is missing here. Therefore, it is not a surprise that controlling the molecular arrangement and wettability of ILs on the solid surface is currently very challenging.

Recently, using AFM and ATR-FTIR, Gong *et al.*[54, 55] showed that the adsorption of water on the mica surface under the ambient air condition promotes the extended layering of ILs on the mica surface while dewetting of ILs occurs when the water is removed by heating. Meanwhile, Cheng *et al.*[56, 57] showed that the addition of the water in the IL also promotes the extended layering of ILs on the mica surface based on AFM force-distance profile results. These findings suggest that the surface-adsorbed water might be the missing key parameter and therefore the humidity control could be an effective method controlling the molecular arrangement and macroscopic wettability of ILs on the mica and other solid surfaces. Gong *et al.*[54, 55] proposed two possible

mechanisms explaining the effect of the adsorbed water on mica. The first mechanism is "water-enabled surface charging". ILs have low dielectric constants[7, 58, 59] and therefore cannot effectively dissolve K^+ ions on the mica surface and induce the surface charging. Only when water is adsorbed on the mica surface, K^+ ions will be dissolved and leave the mica surface and thus the surface will be negatively charged. As a result, the IL cations are able to occupy the "empty" site left by K^+, initiating the layering of cations/anions. The second proposed mechanism is "water-assisted self-assembling". In bulk ILs, it has been reported[60, 61] that the water induces the stronger self-assembling of ILs by coupling with IL ions via H-bonding and thus leading to a more extended polar network that enhances the segregation of polar and non-polar domains. The similar mechanism could work at the IL/mica interface as well. Because the mica surface serves as a flat template to initiate the packing of ILs, the water-assisted self-assembling of ILs is expected to result in the extended layering structure. The mechanism of "water-enabled surface charging" was echoed by Cheng *et al.*[56, 57] based on their AFM based 2-dimension-force-distance experiments, where they concluded that the presence of water induces the hydration and dissolution of interfacial K^+ and thus results in the surface charging. However, there have been different voices. Sakai *et al.*[62], Wang *et al.*[63] and Jurado *et al.*[64] reported that addition of water into ILs disrupted the layering of ILs on the mica surface based on the AFM force-distance profile. McDonald also argued that electrification of mica already occurs in dry ILs.[65] Meanwhile, the study on the effect of water on the macroscopic wettability of ILs on the mica is very limited. Wang *et al.*[63] reported that addition of water into ILs increases the contact angle of ILs on the mica. Interestingly, in a more recent study, Wang *et al.*[66] showed that the contact angle of ILs decreases with the increase of RH. The extensive controversy suggests that more research is needed to uncover the underlying mechanisms of the effect of the water.

Here we report ATR-FTIR, contact angle and AFM results showing that, indeed, tuning humidity is a facile and effective approach manipulating the molecular arrangement and macroscopic wettability of ILs on the mica surface. ATR-FTIR studies indicated that more water is adsorbed on the mica surface with the increase of the humidity. Contact angle tests showed that the contact angle of ILs on the mica decrease with the increase of the humidity. Moreover, at higher humidity, the contact angle decreases with time up to five minutes. AFM results showed that, with the increase of the humidity, the nanoscale IL on the mica surface transitions from droplet to molecular layers gradually. All these findings, at different length scale, can be rationalized by the following proposed mechanism. With the increase of the humidity, more water adsorbs on the mica surface, which dissolves and mobilizes K^+ on the mica. As a result, the cations of ILs occupy the empty spots left by the K^+ and initiate the layering of ILs. The water-enabled ion exchange and IL layering processes result in not only the increase in nanoscale wetting but also the decrease of the macroscopic IL contact angle on the mica surface.

2.2 Experimental Section

2.2.1 Materials

1-butyl-3-methylimidazolium tris(pentafluoroethyl) trifluorophosphate (BMIM-FAP) (high purity grade, >99%; mp, 3 °C; viscosity, 93 cP) was purchased from EMD Millipore Corporation and utilized as received. 2,3-Dihydrodecafluoropentane, commercially known as Vertrel XF, was obtained from Miller Stephenson Chemical Corporation and used as received. Muscovite mica (grade V1; thickness of 0.18 - 0.25 mm) was purchased from Ted Pella and cut

into small sheets (1.5 cm × 2 cm). To produce the fresh mica surfaces, a sharp razor blade was inserted into the edge of the mica sheet and then the sheet was gently separated into two pieces.

2.2.2 Relative Humidity (RH) Control Using Saturated Salt Solutions

Different relative humidity, ranging from 7% to 99%, was created by using a series of saturated salt solutions in a closed system.[34] The closed system was produced by sealing bi-compartment petri dishes with aluminum foils, where the saturated salt solution and the freshly cleaved mica were placed into two compartments. The vent between the compartments ensured the same RH within the close system. Table 1 shows the measured RH values over saturated salt solutions, which were recorded with the Fisher brand traceable humidity meter, along with the literature values.[34]

Table 1. RH of various saturated salt solutions

	Literature[67]	Experimental
NaOH	7.0%	7.0%
CH_3COOK	22.2%	28.0%
NaI	39.2%	48.0%
NaBr	58.2%	60.0%
$(NH_4)_2SO_4$	80.2%	80.0%
K_2SO_4	97.0%	99.0%

2.2.3 Fabrication and Topography Characterization of the Nanoscale BMIM-FAP/Mica

Nanoscale BMIM-FAP was applied on the freshly cleaved mica surface by dip coating at room temperature, using Vertrel XF as the solvent. Right before the dip coating, the mica was cleaved in the ambient environment and the ambient RH was recorded using a Fisher brand traceable humidity meter. The dip coating was conducted using a KSV Instruments dip-coater at a constant "dip-withdrawal" speed of 60 mm/min. The fabrication was conducted multiple times in the time duration of twelve months with the ambient RH changing from ~15% to ~55%. The topography of the BMIM-FAP/mica samples was characterized by AFM right after dip coating. The AFM characterization was conducted under tapping mode with a Veeco Dimension V SPM.

2.2.4 Other Characterizations

Karl Fischer titration was conducted to characterize the water content in bulk BMIM-FAP. A HYDRANAL moisture test kit from Honeywell Research Chemicals was used as received, and the end points were determined upon color change from colorless to light brown. The surface tension of BMIM-FAP was determined by pendant drop analysis with a VCA Optima XE system using the software supplied with the equipment. Table 2 summarizes some physical properties of BMIM-FAP. It is worth noting that the water content of bulk BMIM-FAP is only 276 ppm, which indicates that BMIM-FAP is very hydrophobic.

Table 2. Physical properties of BMIM-FAP

Water content (ppm)	Surface tension (mJ/m2)	Molecular dimension (nm)
276	31.1 ± 0.4	0.84

The macroscopic contact angle of BMIM-FAP on the mica was measured with a VCA Optima XE system using 2 μL drop size. Right after being cleaved, fresh mica was placed into the closed system at the desired RH for at least 6 hours before the contact angle measurement to ensure that the equilibrium condition was reached. In the contact angle test, the needle penetrating the aluminum foil dispensed the BMIM-FAP droplet onto the mica surface so as to maintain the desired RH within the closed system. Droplet images were taken by a charged coupled device (CCD) camera and analyzed with the vendor-supplied software. To study the time-dependence of wetting behavior of BMIM-FAP on the mica surface, contact angles were measured up to 30 minutes.

ATR-FTIR measurements were conducted with a Bruker Vertec-70 LS FTIR and a Bruker Hyperion 2000 microscope in reflectance mode with Ge 20x ATR objectives and a liquid nitrogen cooled mid-band MCT A detector (7000 - 600 cm^{-1} spectral range). Before measurements, the system was purged for 20 minutes with nitrogen gas and a background spectrum was collected without having the ATR crystal contacting the sample. The freshly cleaved mica was stored in the closed system at the desired RH (with saturated salt solutions) for at least 6 hours. Right before the test, a tiny opening was created in the aluminum foil to allow the ATR crystal to be in contact

with the mica sample. The spectrums were collected for 160 scans at 4 cm^{-1} resolution within the spectrum range of 1000 cm^{-1} to 4000 cm^{-1}.

2.3 Results and Discussion

2.3.1 Water Adsorption under Various RH

To investigate the effect of water adsorption on the mica surface, ATR-FTIR characterization was conducted on the mica under three different RHs: 7% RH, 48% RH and 99% RH. The ATR-FTIR results are shown in Figure 1. Since ATR crystal material is Germanium with the penetration depth of 650 nm at 45°, some near-surface "substrate" information could also be detected. To address this concern, the same piece of mica was utilized in all three RH conditions. In this way, any observed difference cannot be attributed to the mica substrate. This conclusion is further supported by XPS characterization. XPS survey scan was carried out on the freshly cleaved mica under different RH. All elements of mica, including Si, K, Al, and O, were clearly observed in the XPS survey spectra (Figure 1). It was found that the intensities of elements associated with mica were independent of RH changes, showing that the structure of mica does not change with RH.

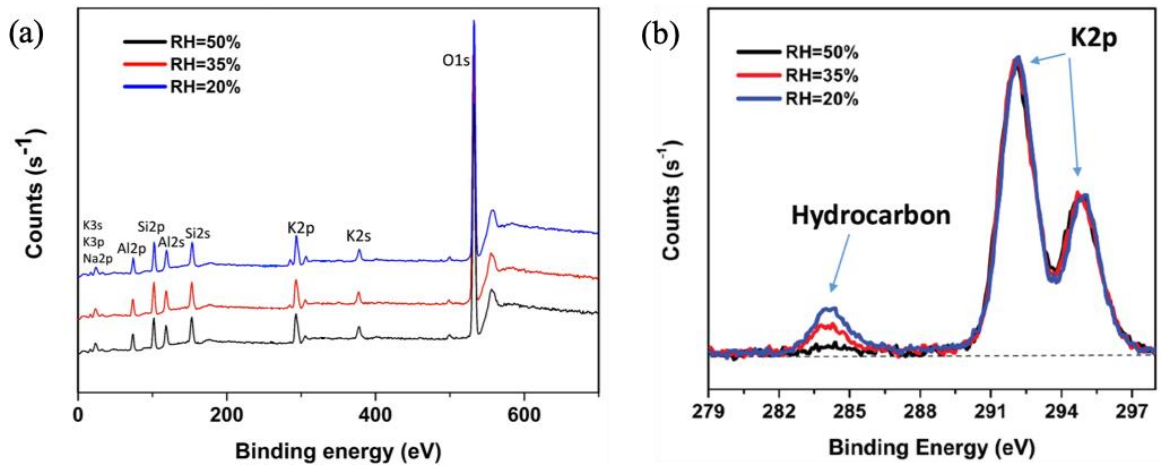

Figure 1. XPS of freshly cleaved mica surface under different RH. (a) Survey scan. (b) High-resolution C1s spectra.

Since mica has strong signal in the region of 3500 cm^{-1} to 3700 cm^{-1},[68] only the region below 3500 cm^{-1} is shown in Figure 2. The broad peak located from 3200 cm^{-1} to 3500 cm^{-1} can be attributed to water adsorption.[68] As expected, at 99% RH, there is significantly more water adsorbed on the mica surface than at 7% RH and 48% RH. Interestingly, ATR-FTIR results indicate that the amount of adsorbed water at 7% and 48% are comparable. This can be attributed to two factors. First, previous IR[68], ellipsometry[69] and transmission interferometric adsorption sensor[70] studies all showed that, at ~7% RH and ~48% RH, the difference of the water adsorption on the mica is limited, i.e., ~0.1 nm vs. ~0.2 nm. Second, in our ATR-FTIR measurement, an opening was created to enable the ATR crystal to be in contact with the mica sample. As a result, the ambient RH could impact the water adsorption on the mica. Nevertheless, the significantly higher water adsorption at 99% RH is in line with previous studies[68, 69] and indicates that water adsorption increases with RH.

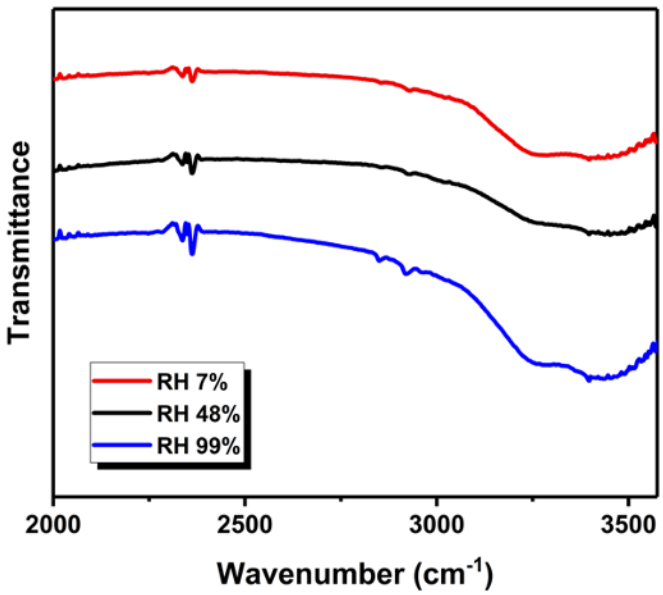

Figure 2. ATR-FTIR spectrum of mica surfaces under various RH.

2.3.2 Macroscopic Wettability under Various RH

Figure 3 shows the contact angles of [Bmim][FAP] on mica under different RH. Right after the [Bmim][FAP] droplet is placed on the mica surface, the contact angle of [Bmim][FAP] under 7% RH is 22° and the contact angle decreases with the increase of the RH. When RH is 99%, the contact angle is only 14°. Interestingly, the time-dependence of the contact angle also changes significantly with RH. At 7% RH, the contact angle does not change with time. At 23% RH, the contact angle marginally decreases with time up to 5 minutes. When RH is above 23%, the contact angle decreases significantly with time and the decrease increases with RH. At 99% RH, the contact angle drops to 0° after 5 minutes. At all RHs, the contact angles level off after 5 minutes, which is ~3 orders of the magnitude of the time scale estimated using Voinov's model of dynamic wetting[71, 72]. In other words, the time-dependent contact angle observed here cannot be explained

by the spreading of the bulk liquid. It is also noteworthy that the [Bmim][FAP] is thermally very stable and it will not evaporate at room temperature.[11] As a result, the change of the contact angle with time cannot be attributed to the evaporation of [Bmim][FAP] as well. Since [Bmim][FAP] is so hydrophobic, the decrease of the contact angle with the increase of the RH cannot be attributed to the water adsorbed on the mica surface because the adsorbed water is expected to increase the contact angle. Moreover, the water content of [Bmim][FAP] after exposure under 99% RH for half day is only 326 ppm from Karl Fischer titration, which is comparable to the bulk water content of 276 ppm under ambient condition as shown in Table 1. This result indicates that adsorption of water in IL at high RH is not the root-cause for the decreased contact angle, either.

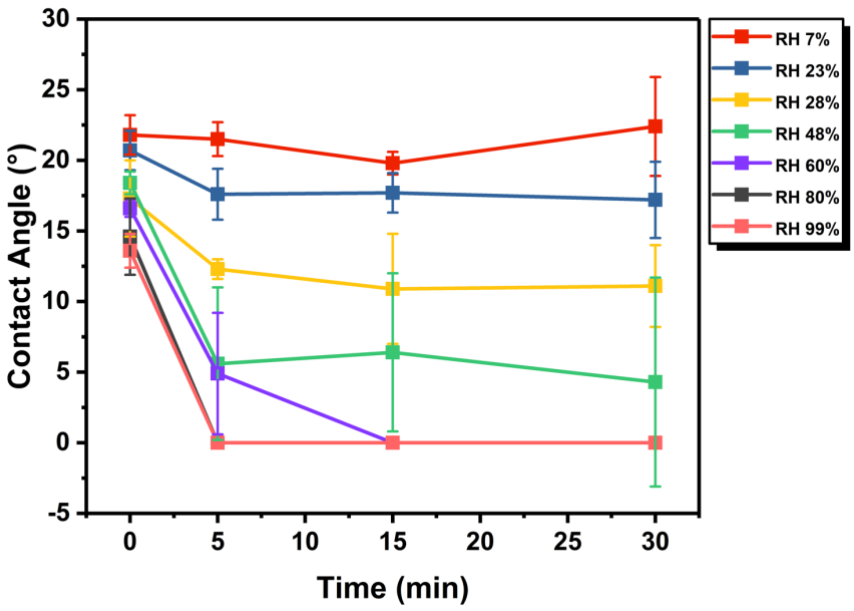

Figure 3. ATR-FTIR spectrum of mica surfaces under various RH.

The RH-dependence of the contact angle of [Bmim][FAP] can be attributed to the water-enabled ion exchange between K^+ on the mica surface and the [Bmim] cation and the resulting

water-assisted layering of [Bmim][FAP] as previously proposed[54, 55]. It was reported that K^+ ions on the mica surfaces dissociate[73-75] when the freshly cleaved mica is in contact with water. Under ambient conditions, water adsorption on the mica readily occurs and the amount of the adsorbed water is dependent on RH. [68-70, 76] Previously, IR[68], ellipsometry[69] and transmission interferometric adsorption sensor[70] results suggested that a statistical monolayer of water, i.e., ~0.2 nm, is formed on the mica when the RH is ~ 20%. Scanning polarization force microscopy (SPFM)[76], which measures the force induced by the electrical polarization when a charged object approaches a substrate, implied that such monolayer is strongly bound to the mica. SPFM study[76] also suggested that, between ~20% and ~50% RH, more water is adsorbed and the film forms hexagonal domains in epitaxial relationship with the mica substrate and is solid-like in nature. Above ~50% RH, the adsorbed water is bulk-like and much more mobile.[76] SPFM study[77] also indicated that the mobility of K^+ on the mica surface exhibits an exponential increase with RH. A reasonable explanation is that RH has two effects. First, with the increase with RH, more water is adsorbed on the mica surface and thus more K^+ are dissociated from the mica. Second, with the increase of RH, the adsorbed water transitions from strongly bound water to more mobile bulk-like water. Therefore, the mobility of K^+ increases with RH. Accordingly, at very low RH, i.e., ~7%, few K^+ is dissociated and the mobility of K^+ is low. As a result, the ion exchange between K^+ and [Bmim] cation is hindered and the contact angle of [Bmim][FAP] on the mica is relatively high. With the increase of RH, more K^+ is dissociated and the mobility of K^+ is higher, which promotes the ion exchange between K^+ and [Bmim] at the IL/mica interface. When RH is above ~50-60 %, [Bmim] initiates the extended layering of [Bmim][FAP][54, 55], where water is also critical since it could induce the stronger self-assembling of [Bmim][FAP] by coupling with ions via H-bonding forming[55]. As a result, the layering of [Bmim][FAP] facilitates the wetting process of

[Bmim][FAP] on the mica and results in complete wetting of the IL on the mica. As shown in Figure 3, the final contact angle of [Bmim][FAP] are zero when RH is above ~60%.

Indeed, the water-enabled ion exchange between K^+ on the mica and [Bmim] cation is also critical to the time-dependence of the contact angle. The key evidence is that, as shown in Figure 3, the contact angle does not change with time at 7% RH while it decreases significantly with time at higher RH. We propose a mechanism as follows. The time-dependence results from the ion exchange between K^+ and [Bmim] and the resulting layering of [Bmim][FAP] at molecular-level. At high RH, the K^+ is readily dissociated and has high mobility, which enables the ion exchange and layering process. At 7% RH, the water adsorption and thus the dissociation of K^+ is very limited, which renders the ion exchange and the resulting layering of [Bmim][FAP] impossible. As a result, the contact angle does not change with time at low RH. Previously, Wang and Priest[72] reported the similar time-dependence of the contact angles of different ionic liquids on the mica surface and attributed the slow change of the contact angles to the precursor film formation. However, to date, the underlying mechanisms governing the formation of the precursor films has yet to be uncovered. Our results suggest that the ion exchange between K^+ on the mica and the [Bmim] initiates the layering of [Bmim][FAP], which is the process of creating the precursor film. This idea is in line with a recent report that ionic liquids spread faster on the mica with higher RH.[66]

2.3.3 Molecular Arrangement under Various RH

To test the above-mentioned hypothesis, the morphology of nanoscale [Bmim][FAP] on the mica was characterized by AFM. Typical AFM results are shown in Figure 4 and more AFM results can be found in Figure 5. As shown in Figure 4, similar to macroscopic contact angle, the

wetting behavior at nanoscale changes dramatically with RH. At 20% RH, a droplet structure was clearly revealed by AFM as shown in Figure 4a. The diameter of the droplets ranges from hundreds of nanometers to a few micrometers and the height of the droplets are between a few nanometers to tens of nanometers. Interestingly, when the RH increases to 35%, isolated "pancakes" with the diameter of a few micrometers and the height from 4 to 8 nanometers were observed (Figure 4b). The result suggests that the increase in RH promotes the wetting of nanoscale [Bmim][FAP]. When the RH increases to 50%, a network-like "terraces" with the steps of up to 2 nanometers were clearly visible in the AFM image (Figure 4c), which are typical extended layering structure of [Bmim][FAP] on the mica surface. As the RH rises to 99% (when applying saturated K_2SO_4 environment), most of the mica surface is covered with IL layer with thickness of ~2 nanometers, which indicates more complete wetting of nanoscale [Bmim][FAP]. The nanoscale AFM results are in line with the macroscale contact angle results. In both cases, when RH is lower than ~20% where adsorbed water is less than statistical monolayer, [Bmim][FAP] has relatively low wettability. While RH is higher than ~50% where adsorbed water is more and more bulk-like, [Bmim][FAP] wets the mica completely.

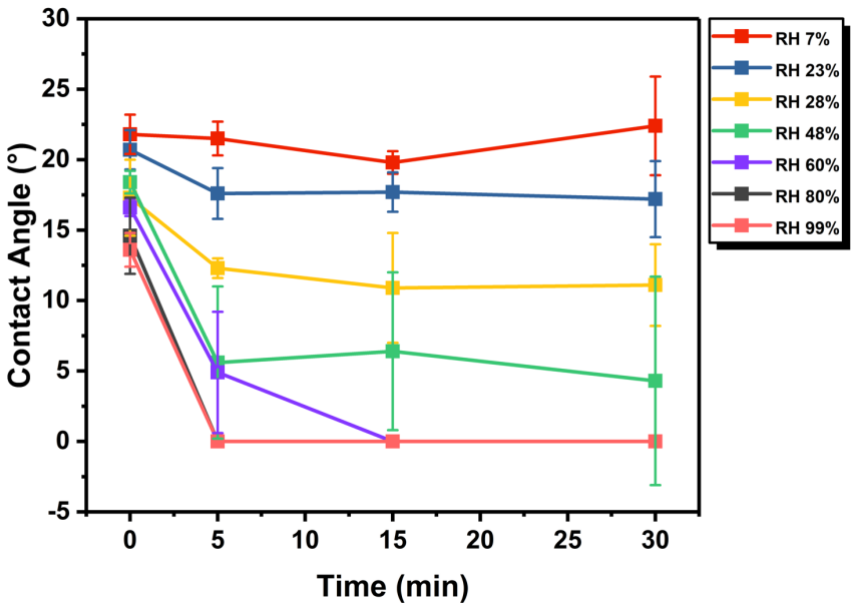

Figure 4. AFM images and line profile of [Bmim][FAP] on freshly cleaved mica. (a) at RH=20%, (b) at RH=35%, (c) at RH=50%, and (d) RH=99%. Images are 20 μm × 20 μm and the height bar is 20 nm.

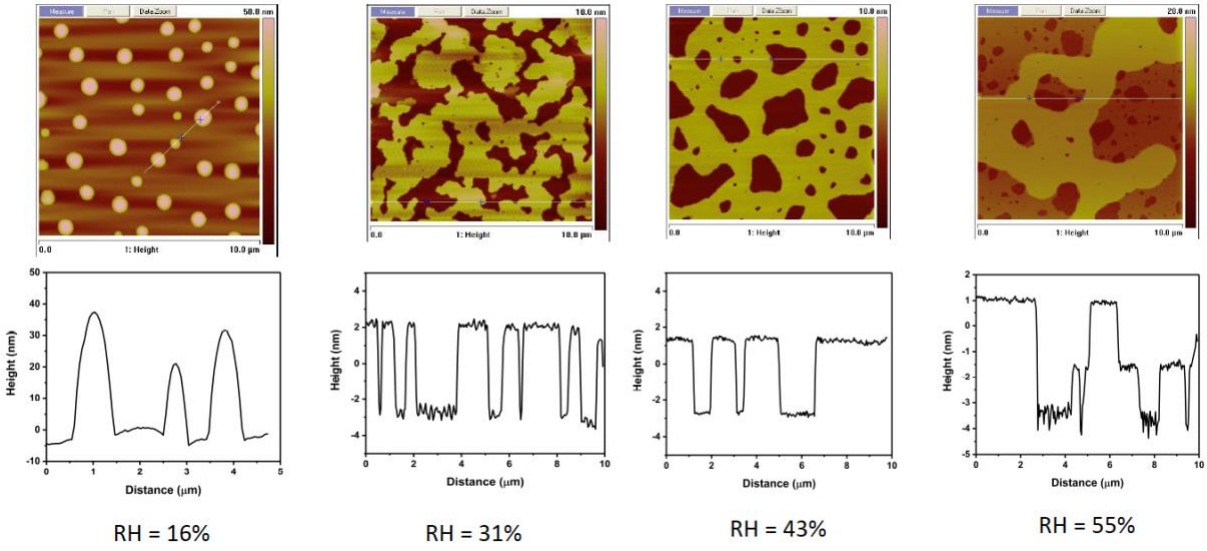

Figure 5. AFM images and line profile of [Bmim][FAP] on freshly cleaved mica.

The AFM results provide the direct evidence that the molecular-level layering of [Bmim][FAP], i.e., likely the formation of the precursor film, readily occurs at high RH, which indicates that the ion exchange between K^+ and [Bmim] and the resulting layering is the key mechanisms governing the molecular arrangement and macroscale wetting. This mechanism is further illustrated in Figure 6. On dry mica, hydration of K^+ is impossible and K^+ is immobile. As a result, contact angle of ILs is relatively high and it does not change with time. On wet mica, K^+ is hydrated/dissolved and has higher mobility, which enables the ion exchange between K^+ and [Bmim] and the subsequent IL layering. Therefore, the contact angle decreases with time and wettability is enhanced.

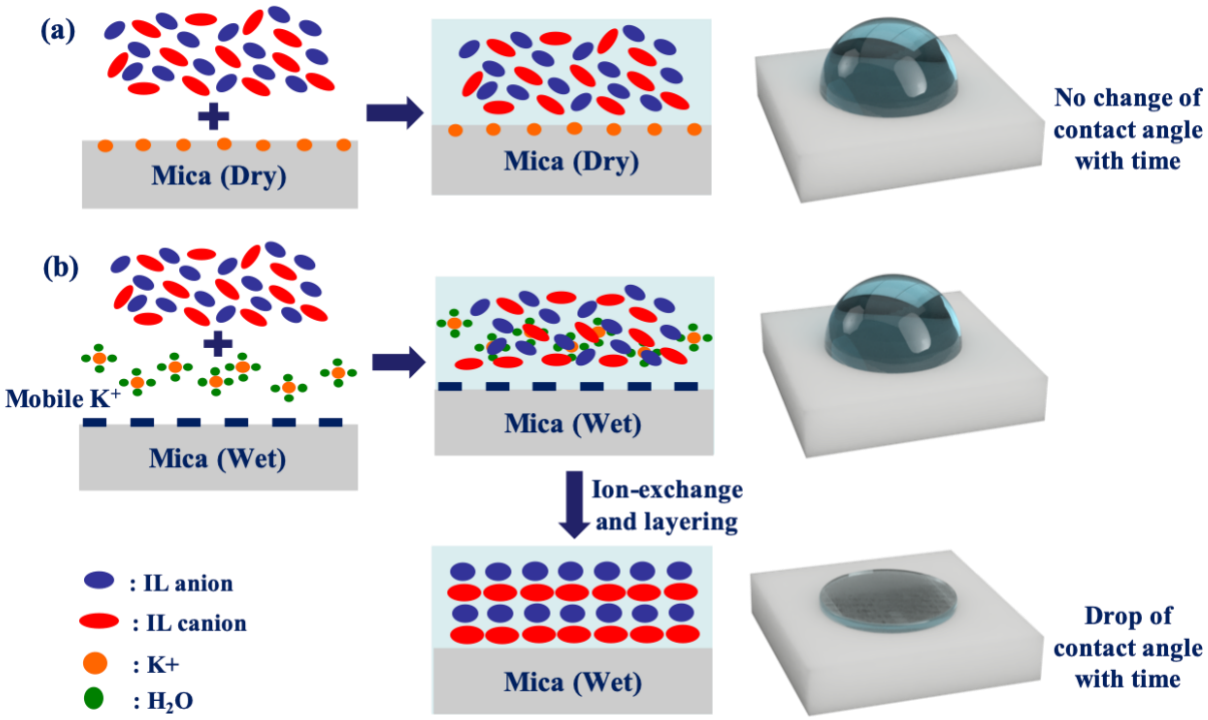

Figure 6. The proposed mechanisms illustrating the effect of adsorbed water on the molecular arrangement and wetting of ILs on the mica surface. (a) Dry mica (Top). (b) Wet mica (bottom).

IL/Metal interface is practically important in lubrication and energy storage. Previous studies[78-81] showed the solid-like layering structure of ILs at the IL/gold interface, which is similar to our findings on the mica surface. Such layering has also been attributed to the strong electrostatic attraction between ILs and the gold substrate.[78-81] However, to date the effect of water has not been extensively studied. Cheng *et al.*[56] reported the significant water effects on gold electrodes at positive electrochemical potentials. They[56] concluded that the influence of water is via the interactions within the IL layers and is not due to the adsorption of water on the polarized electrode. Meanwhile, molecular dynamics (MD) simulations[82] showed that water is greatly enriched at IL-electrode interface when the electrode is slightly electrified even if the ILs are hydrophobic. It was found that[82] the local packing of IL ions, the water-IL anion interactions, and the nature of electrode material are all important in determining the interfacial enrichment of water. The above-mentioned results indicate that water could be a key parameter at IL-metal interfaces though more research is required to uncover the underlying mechanisms.

2.4 Conclusions

In conclusion, we report that tuning humidity is a facile and effective approach manipulating the molecular arrangement and macroscopic wettability of ILs on the mica surface. We have provided direct experimental evidence showing that, under different humidity, the molecular arrangement of ILs on the mica surface could be droplet, "pancake", or extended layering. Meanwhile, the macroscopic wettability increases with the relative humidity. The experimental results suggest that the underlying mechanism is the water-enabled ion exchange between K^+ and the IL cation and the resulting layering of ILs. At low humidity (low water

adsorption), the K^+ dissolution is very limited and thus the ion exchange is hindered. As a result, the IL takes a droplet structure at nanoscale and the macroscopic wettability is lower. At high humidity (high water adsorption), the K^+ is dissolved and mobilized, which enables the ion exchange between K^+ and IL cations and initiates the layering of ILs. Therefore, the IL takes an extended layering structure at nanoscale and the macroscopic wettability is higher. Since the similar phenomenon is likely to occur at other IL/solid interfaces, the current research potentially provides a new dimension controlling the performance of ILs at the IL/solid interface in many important applications.

3.0 Direct Observations of the Double-Layering Molecular Structures of Mica-Confined Ionic Liquids

The material in this chapter is based upon a manuscript for submission to *Small* or *Chemical Science*.

3.1 Introduction

Ionic liquids (ILs) have drawn more and more research interests because of their extraordinary physiochemical properties. Unlike common inorganic salts, the liquid phase is thermodynamically favorable for ILs under ambient conditions, since the Coulombic attractions are disrupted due to the large and bulky organic cations and anions.[37, 78, 83] Their excellent properties, which include high thermal stability, negligible volatility, wide liquidus range, excellent capability of dissolving materials,[1-3] make them ideal candidates for applications in separations, solvents for chemical synthesis, etc.[4-8] The interface between ILs and solids are especially crucial to many promising applications, such as electrolytes for energy storage devices,[9, 10] lubricants for nano- and microelectromechanical systems (NEMS/MEMS) and hard disk drives (HDD),[11-15] absorbents for carbon capture,[16, 17] and green catalysis.[18, 19] Since the IL/solid interface always plays a fundamental role, it is critical to understand the molecular structure of ILs confined to solid surfaces. Muscovite mica has been frequently used as the model solid because of its atomically smooth surface and well-studied surface chemistry.[84, 85] Muscovite mica exhibits layered structure along the (001) basal plane, with interlayered K^+ between two aluminosilicate

layers to balance the negatively charged crystals.[84] Upon cleavage at the interlayer, statistically equal amounts of K^+ are distributed on both mica surfaces.[86].

A handful of studies on the molecular structure of ILs on the mica surface have been previously reported. Atkin et al. performed the AFM force-distance study for a tip approaching and leaving the mica surface in two protic ILs, EAN and PAN, and an aprotic [Emim][Ac], and concluded that ILs form solid-like extended layering structure on mica.[20, 78, 87] Perkin et al. used surface force apparatus (SFA) to study the oscillation distance from the squeeze-out of an ion pair for [C_nMIm][NTf_2] between two mica sheets.[26-28] They proposed that the ILs with shorter alkyl chains form monolayer structures with the alkyl chains parallel to mica, while the ILs with longer alkyl chains form tail-to-tail bilayer structures with the alkyl chains perpendicular to mica. However, the complicated AFM force-distance and SFA processes can only indirectly characterize the nanofilms by deciphering the force-distance profiles. Liu et al. noticed the coexistence of the liquid phase and the stable solid-like phase of [Bmim][PF_6] on the mica surface at RT under tapping mode AFM.[32] Bovio et al. reported different observation that there is only solid-like layering for [Bmim][NTf_2] on mica.[29] Later, Yokota et al. detected inhomogeneous layering structures of [Bmim][NTf_2] and [Bmim][BF_4] at the IL/mica interface using frequency-modulation AFM (FM-AFM).[30] While they observed the extended layering structure of ILs on the mica surface, a comprehensive picture of the interfacial arrangement of IL cations and anions at the molecular has not yet been uncovered.

In this study, the interfacial molecular structures of mica-confined ILs with various alkyl chain lengths in the cations, i.e., [Emim][FAP], [Bmim][FAP], and [Hmim][FAP], were investigated by AFM. It was directly observed under RH > 30% that the IL nanofilms grow discontinuously on mica by the thickness of ~2 ML. A double-layering interfacial molecular

arrangement of IL cations and anions on the mica surface has been proposed based on the equilibrium nanofilm topographies. Time-dependent AFM results at RH < 20% also reveal the slower spreading for ILs with longer alkyl chains when confined to the mica surface.

3.2 Experimental Section

3.2.1 Materials

The imidazolium ILs utilized were a series of ILs with the same [FAP] anions and three different alkyl chain lengths in the cations, i.e., 1-ethyl-3-methylimidazolium tris(pentafluoroethyl)trifluorophosphate ([Emim][FAP]), 1-butyl-3-methylimidazolium tris(pentafluoroethyl)trifluorophosphate ([Bmim][FAP]), and 1-hexyl-3-methylimidazolium tris(pentafluoroethyl)trifluorophosphate ([Hmim][FAP]). They were acquired from Millipore Sigma and used as received, and the purities are higher than 98%. Their molecular structures are shown in Figure 7. The solvent for ILs was 2,3-Dihydrodecafluoropentane (marketed as Vertrel XF), which was purchased from Fisher Scientific and used as received. Muscovite mica sheets (highest quality grade V1) were purchased from Ted Pella.

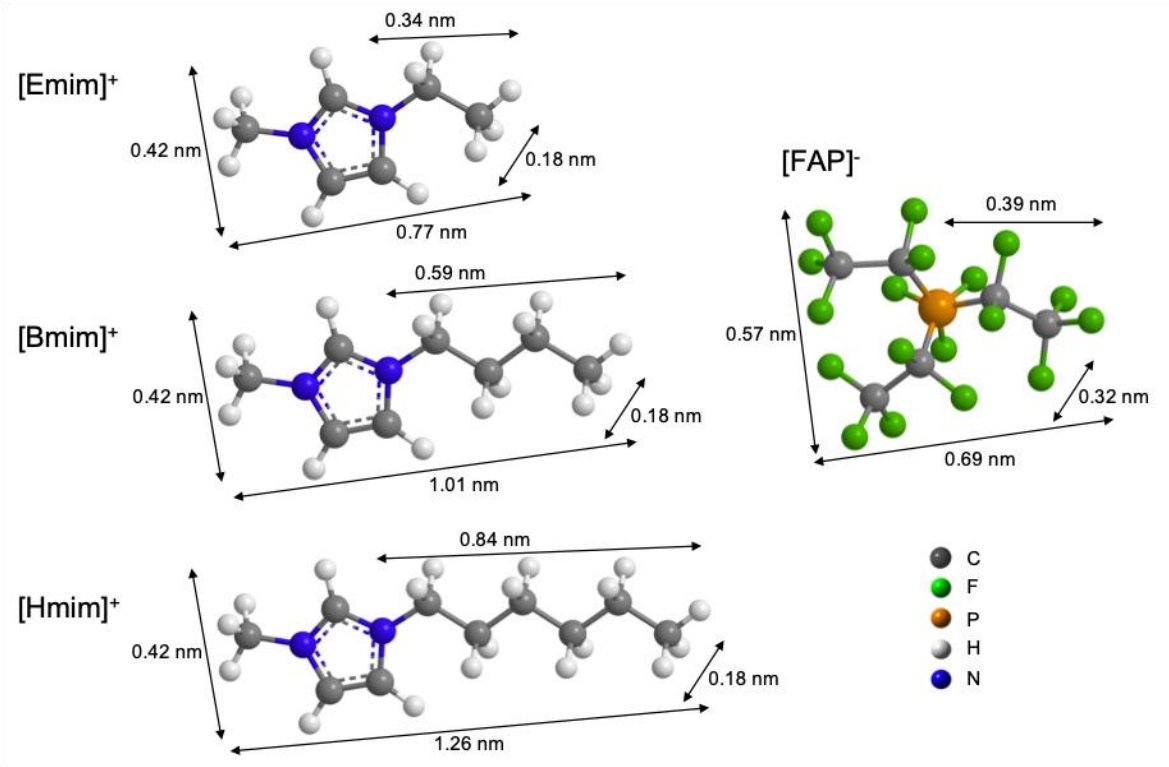

Figure 7. 3D chemical structures of the imidazolium cations with various alkyl chain length and the [FAP] anion. Energy minimization was performed using the MMFF94 force field.

3.2.2 Thin Film Fabrication

Nanometer-thick IL films on mica were fabricated with a KSV Instruments dipcoater based on a previously established approach in our lab.[88, 89] IL solutions were made by dissolving ILs in Vertrel XF at a series of concentrations. Mica sheets were cleaved by a sharp tweezer right before the dipcoating process to make fresh mica surfaces. The AFM image and the corresponding line profile of the atomically smooth mica surface are shown in Figure 8a as control. The cleaved mica pieces were dipped into and pulled out from the IL solutions at a constant speed of 60 mm/min

using the dipcoater, as shown in Figure 8b. The growths of the IL nanofilms in this study were controlled by sequentially increasing the concentrations of the IL solutions.

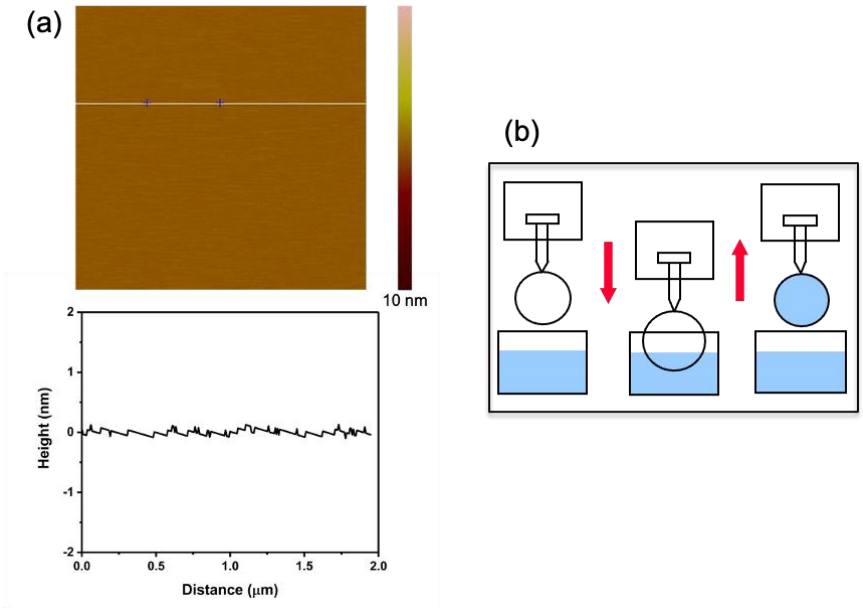

Figure 8. (a) AFM image and the corresponding line profile of the fresh mica surface. The scan area is 2 μm by 2 μm, and the inset scale bar is for the z-direction. (b) Fabrication of IL nanofilms on mica by dipcoating.

3.2.3 AFM Characterization

The surface topography of the IL nanofilms on mica was characterized by tapping-mode AFM using a Veeco Dimension V Scanning Probe Microscope. The AFM probe used (MikroMasch NSC14/AL BS) has an 8 nm aluminum tip on an n-type silicon cantilever, a resonance frequency of 160 kHz, and a force constant of 5.0 N/m. The scan area was set at 10 μm by 10 μm with a pixel density of 256 by 256, so the lateral resolution was 39 nm.

3.2.4 Surface Tension Measurement

The liquid-air surface tension values of the bulk ILs were measured by the pendant drop analysis with a VCA Optima XE contact angle machine at room temperature.

3.3 Results and Discussion

3.3.1 Quantized Growth of [Emim][FAP] on Mica

When confined to a solid surface, ILs often form interfacial molecular structures dramatically different from the bulk structure.[3, 28, 90] In the current study, a quantized growth of [Emim][FAP] nanofilms was first directly observed in the AFM results at RH higher than 30%. The growth of the nanofilms was controlled by sequentially increasing the concentration of the IL solutions during thin film fabrications, and the surface characterizations were performed within half an hour after the thin film fabrications. Initially, the IL film only covers more solid surface areas at the constant film thickness. At a critical stage of film growth, there is a sharp increase in the overall film thickness. The nanofilm thickness remains constant again afterward as the IL film grows. The film thickness was taken as the average distance between the top of the film and the mica surface for each film growth stage.

As shown in Figure 9a-c, when fabricated from solutions at lower concentrations, i.e., 0.25 g/L to 0.75 g/L, the average thickness of [Emim][FAP] nanofilms remains constant at ~1.8 nm. As the nanofilm grows, the IL films only cover more solid surface areas at this stage. The film topography changes from small islands to more closely packed islands to connected sponges.

Interestingly, when the IL concentration increased from 0.75 g/L to 1 g/L, a quantized increase in the thickness of the sponge-like nanofilm to ~4.4 nm was observed, as seen in Figure 9d. It is worth noting that the hydrocarbon adsorption on mica is expected to induce low surface energy at some local surface areas, which in turn leads to the uneven coverage of the IL nanofilms.[91] As the concentration increased from 1 g/L to 1.5 g/L, the overall thickness of the growing IL nanofilms remained at ~3.5 nm (Figure 9e). However, the film topography switches to one loosely connected film sitting on another smooth film upon the film growth. The thicknesses of the top and bottom layers are ~1.6 nm and ~1.8 nm, respectively.

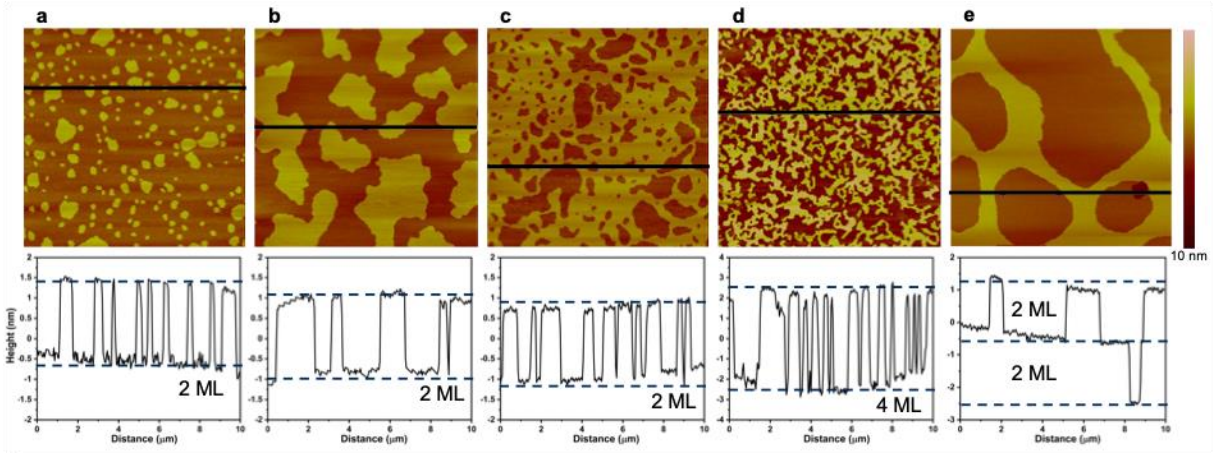

Figure 9. AFM images and their corresponding line profiles of mica-confined [Emim][FAP] fabricated from the concentration of (a) 0.25 g/L, (b) 0.5 g/L, (c) 0.75 g/L, (d) 1 g/L, and (e) 1.5 g/L. The AFM scan areas are 10 μm by 10 μm, and the inset scale bar is for the z-direction. The x-axis and y-axis for the line profiles are the distance along the cut in the horizontal direction (μm) and the height in the vertical direction (nm), respectively.

If the bulk [Emim][FAP] molecules are assumed to be cubes,[13, 92] the edge length can be calculated by $(\frac{M/N_A}{\rho})^{\frac{1}{3}}$, where ρ is the bulk density (1.71 g/cm^3 at RT), M is the molecular weight (556.17 g/mol), and N_A is the Avogadro constant. The edge length of [Emim][FAP] molecules is calculated as 0.81 nm, which is roughly half of the thickness of [Emim][FAP] nanofilms fabricated from low concentrations. Assuming one monolayer (ML) of the IL nanofilm is one layer of [Emim][FAP] molecules densely packed in the lateral direction, the starting thickness of [Emim][FAP] nanofilms is the thickness of ~2 ML. Interestingly, the film thicknesses did not grow consecutively with the increasing concentration of the IL solutions. Instead, the thicknesses increased by ~2 ML from 0.75 g/L to 1 g/L. Except for the quantized increase, the film thickness remained constant at ~2 ML for thinner films and ~4 ML for thicker films.

3.3.2 Double-Layering Interfacial Molecular Structure

Similar to the quantized growth of [Emim][FAP] nanofilms, the nanofilms of [Bmim][FAP], which has a longer alkyl chain in the imidazolium cation, also exhibit quantized growth of layers on the mica surface at RH higher than 30%. The AFM images and the line profiles in Figure 10 present the quantized growth of mica-confined [Bmim][FAP]. The edge length of the [Bmim][FAP] molecule is estimated to be 0.84 nm based on its bulk density of 1.63 g/cm^3 at RT and its molecular weight of 584.23 g/mol. When the solution concentrations are low, i.e., from 0.25 g/L to 0.75 g/L (Figure 10a-b), the film thickness remains constant at ~1.5-1.7 nm that is the thickness of ~2ML. As the nanofilm grows, it only covers more solid surface areas, with the islands growing bigger and bigger until they are connected. Similar to the growth of [Emim][FAP], as the concentration increases from 0.75 g/L to 1 g/L, the [Bmim][FAP] nanofilm on mica stops growing

with the film thickness constant at ~2 ML thick. Instead, a quantized growth in the film thickness from ~1.7 nm to ~4.4 nm was observed (Figure 10c). The increase in the film thickness is again about the thickness of 2 ML. The overall thickness remains at ~4.4-4.6 nm for the nanofilms of [Bmim][FAP] fabricated from the concentration of 1 g/L to 1.5 g/L (Figure 10c-d). During this stage of film growth, the overall film thickness remained at ~4 ML thick, similar to the [Emim][FAP] nanofilms at this stage. Upon the growth of the films, [Bmim][FAP] covers more mica surfaces to form smoother nanofilms. For the nanofilm fabricated from the concentration of 1.5 g/L (Figure 10d), the film topography again switches to one film with a thickness of ~2.4 nm sitting on another smooth film with a thickness of ~2.2 nm. The thicknesses of both layers are ~2 ML thick. As the dipcoating concentration increases to 2 g/L, the top layer grows in full, resulting in one smooth film on the solid surface. The film thickness is ~4.1 nm, which is about the thickness of 4 ML. The holes within the smooth film could again be contributed to the hydrocarbon absorption on the mica surface from ambient air.

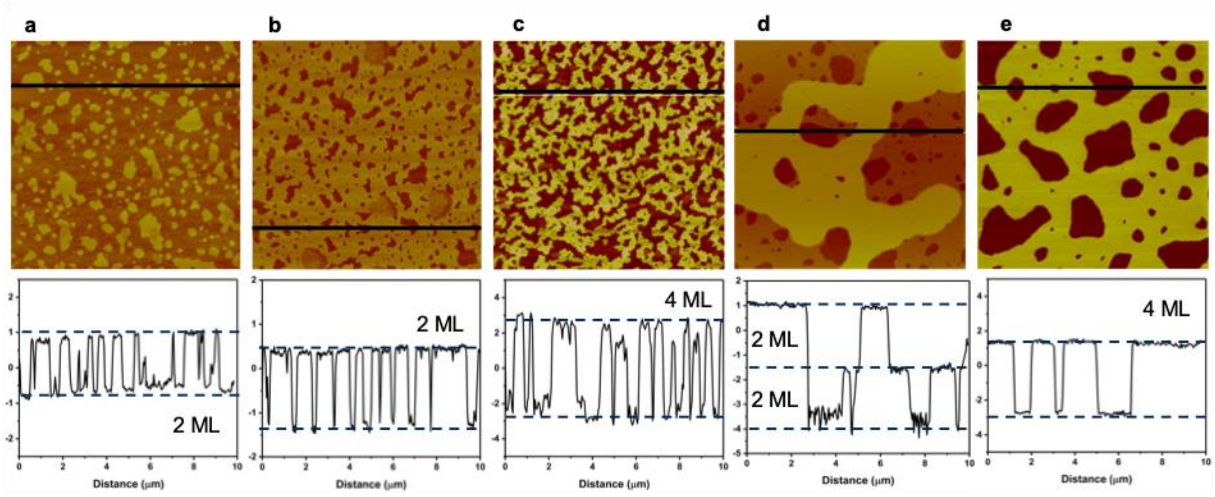

Figure 10. AFM images and their corresponding line profiles of mica-confined [Bmim][FAP] fabricated from the concentration of (a) 0.25 g/L, (b) 0.75 g/L, (c) 1 g/L, (d) 1.5 g/L, and (e) 2 g/L. The AFM scan areas are 10 μm by 10 μm, and the inset scale bar is for the z-direction. The x-axis and y-axis for the line profiles are the distance along the cut in the horizontal direction (μm) and the height in the vertical direction (nm), respectively.

The growth of [Hmim][FAP], which has the longest alkyl chain in the cation among the three ILs, acts very differently from the growth of the other two ILs on mica under RH higher than 30%. Instead of the layering structures, [Hmim][FAP] forms nanodroplet structures when confined on the mica surface as nanofilms. As shown in Figure 11, when the nanofilm was initially fabricated from the most dilute solution (0.25 g/L), one nanodroplet with a height of ~30 nm and a diameter of ~1 nm was observed within the scan area. As the [Hmim][FAP] nanofilm grows (Figure 11b-d), the density of the IL nanodroplets becomes higher and higher, which is again very different from the quantized growth of layers of [Emim][FAP] and [Bmim][FAP]. No layering structure was observed at all for all stages of film growth.

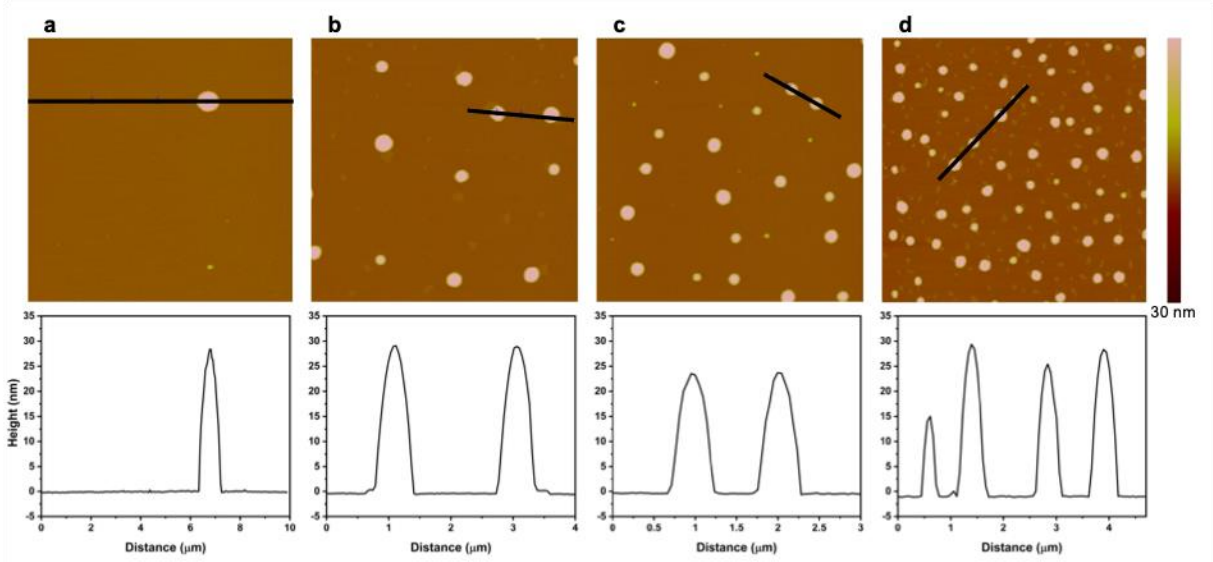

Figure 11. AFM images and their corresponding line profiles of mica-confined [Hmim][FAP] fabricated from the concentration of (a) 0.25 g/L, (b) 0.5 g/L, (c) 0.75 g/L, and (d) 1 g/L. The AFM scan areas are 10 μm by 10 μm, and the inset scale bar is for the z-direction. The x-axis and y-axis for the line profiles are the distance along the cut in the horizontal direction (μm) and the height in the vertical direction (nm), respectively.

The surface tension results of the series of ILs measured by the pendant drop analysis are shown in Table 3. The results are also consistent with previous reports.[93, 94] There is an inverse correlation between the measured surface tension and the alkyl chain length of the cations. Almeida et al.[95] and Zhou et al.[96] claimed that the longer alkyl chain leads to the lower surface tension because the stronger steric effect between ions with longer alkyl chains induces the lower electrostatic interaction. Kolbeck et al.[97] and Pensado et al.[98] proposed that the nonpolar alkyl chains prefer to orient toward air at the liquid-air interface for ILs with longer alkyl chains, which results in the lower surface tension. Our results show that the nanofilms of [Emim][FAP] and [Bmim][FAP], which have ethyl chains and butyl chains in the cations, respectively, act in the

layering structures on mica, and the growth of the layers are discontinuous. However, the nanofilms of [Hmim][FAP], which has the longest hexyl chain in the cations and the lowest surface tension, perform as the nanodroplet structures on mica. Based on Young's equation,[99] a liquid with lower surface tension is expected to have better wettability on a solid surface. However, the nanoscopic wettability of [Hmim][FAP] with the lowest surface tension is the worst among the three ILs on mica. The nanoscopic structures of solid-confined ILs are very different from the bulk structures of ILs on solids.[46, 78] For ILs confined to the mica surface, it is expected that there is a competition between the solid/liquid interaction and the liquid/liquid interaction. Previous ATR-FTIR and AFM results suggest that water absorbed on the mica surface from ambient humidity dissolves and mobilizes the surface K^+, as water has a high dielectric constant.[44, 100] At the solid/liquid interface, ion exchange between the IL cations and K^+ is thus enabled, and layered packing of ILs could be initiated. As a result, layering structures were observed for the nanofilms of [Emim][FAP] and [Bmim][FAP] under RH > 30%. However, [Hmim][FAP] has a longer C_6 alkyl chain in the cation than [Emim][FAP] and [Bmim][FAP]. The strong dispersive force between the nonpolar C_6 alkyl chains enhances the cohesive interaction within the IL molecules, so nanodroplet structures were observed for the [Hmim][FAP] nanofilms as a result of the strong liquid/liquid cohesion. Similar differences in the interfacial structures between imidazolium ILs with C_6 alkyl chains and imidazolium ILs with shorter alkyl chains were also reported based on the AFM force measurement results.[101, 102] [Hmim][FAP] on both highly ordered pyrolytic graphite (HOPG) and Au(111) was found to have stronger interfacial structures against the push-through force than [Emim][FAP], because the longer cation alkyl chain leads to enhanced solvophobic interactions.

Table 3. Surface tension values of the ILs

	[Emim][FAP]	[Bmim][FAP]	[Hmim][FAP]
Surface tension [mN/m]	34.3 ± 0.08	32.3 ± 0.07	31.5 ± 0.05

Interestingly, after the films sit for 1 week under the RH higher than 30%, layering structures were again observed for mica-confined [Hmim][FAP] at various stages of film growth, i.e., nanofilms fabricated from the concentration of 0.25 g/L, 0.5 g/L, 0.75 g/L, and 1 g/L. As shown in Figure 12, the molecular structures of the series of [Hmim][FAP] nanofilms after 1 week were very similar to the quantized layering structures of the nanofilms of [Emim][FAP] and [Bmim][FAP] within half an hour after the thin film fabrications. Only layering structures of [Hmim][FAP] were observed for all series, while no nanodroplets remained on the mica surface anymore. The edge length of the cubic [Hmim][FAP] molecule is estimated to be 0.87 nm based on its bulk density of 1.56 g/cm^3 at RT and its molecular weight of 612.28 g/mol. For nanofilms fabricated from the concentration of 0.25 g/L, 0.5 g/L, and 0.75 g/L after one week, the nanodroplets spread into layers with film thicknesses ~1.5-1.8 nm of ~2 ML, equal to the thickness of ~2ML. The film morphology changes from spikes to more connected islands. As the concentration increases from 0.75 g/L to 1 g/L, another layer with a thickness of ~2 ML grows on the bottom layer. A quantized increase in the overall film thickness from ~2 ML to ~4 ML (~3.3 nm) was again observed. These findings imply that the alkyl chain length in the IL cations may have little impact on the equilibrium states of the morphology of the IL nanofilms confined on

mica, while the spreading kinetics of the IL films could vary significantly with the change of alkyl chain length.

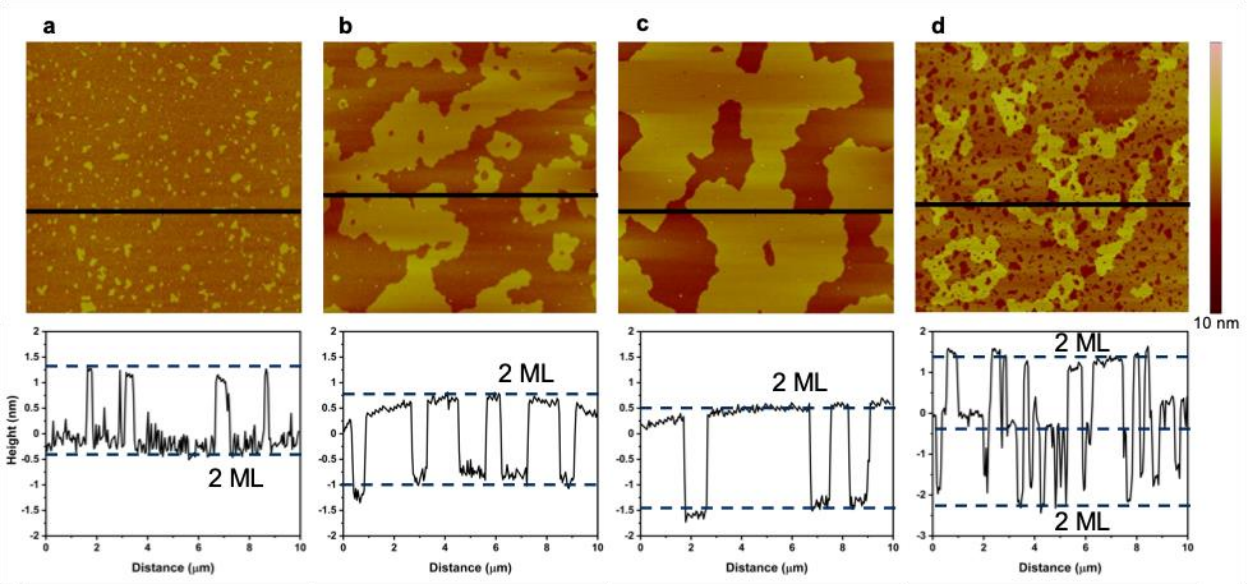

Figure 12. AFM images and their corresponding line profiles of mica-confined [Hmim][FAP] fabricated from the concentration of (a) 0.25 g/L, (b) 0.5 g/L, (c) 0.75 g/L, and (d) 1 g/L. The scans were taken 1 week after the sample fabrications, and the relative humidity (RH) was higher than 30% the whole time. The AFM scan areas are 10 μm by 10 μm, and the inset scale bar is for the z-direction. The x-axis and y-axis for the line profiles are the distance along the cut in the horizontal direction (μm) and the height in the vertical direction (nm), respectively.

Since it is not accurate enough to determine the ML thickness of the films by simply estimating the IL molecular structures to be cubes, it is necessary to uncover the detailed interfacial arrangements of IL cations and anions on mica. By comparing the film thicknesses of the three ILs at the equilibrium states, one can find it surprising that their equilibrium ML thicknesses are almost the same. For instance, the thicknesses of the IL nanofilms right before the quantized growths, i.e.,

0.75 g/L [Emim][FAP] (Figure 9c), 0.75 g/L [Bmim][FAP] (Figure 10b), and 0.75 g/L [Hmim][FAP] (Figure 12c), are ~1.8 nm, ~1.7 nm, and ~1.8 nm, respectively. The chemical structures of the three cations with various alkyl chain lengths and the [FAP] anion are presented in Figure 7. As listed by the detailed dimensions, there is an increase in the alkyl chain length by 0.25 nm for the transitions from C_2 to C_4 and from C_4 to C_6. Consequently, the close ML thicknesses of various ILs determined by AFM imply that the alkyl chains are parallel rather than perpendicular to the solid surface. Additionally, the molecular arrangement is not likely to be a layer of cations adjacent to the mica surface to preserve electroneutrality and a layer of anions on top of the cation layer to form one ML altogether, because this assumption is not able to explain why the thinnest nanofilm is ~2 ML thick and why the quantized film growth is always by ~2 ML. Here, based on the directly-observed thickness results from AFM, we propose a double-layering interfacial molecular structure of IL cations and anions when confined to the mica surface, as shown in Figure 13 with [Bmim][FAP] on mica as an example. Within the building block, the first layer adjacent to the mica surface is a layer of cations. The imidazolium rings are oriented perpendicular to mica, which is also suggested by previous density-functional theory (DFT) and molecular dynamics (MD) simulation works,[103-105] and the alkyl chains are oriented parallel to the mica surface. The second layer in the building block adjacent to the first cation layer is another layer of cations. The configuration is similar to the first cation layer, i.e., the imidazolium rings perpendicular and the alkyl chains parallel to the mica surface. The nonpolar alkyl chains in the first and second cation layers closely pack with each other due to their intermolecular dispersive interaction, and the polar imidazolium heads are opposite to each other. Two [FAP] anions sit on top of the two cations. The electrostatic interaction drives the phosphorous atom of the anion to be close to the CH between the methyl and the butyl chains of the imidazolium ring (C(2)H), as

indicated by previous ab initio molecular orbital calculations.[106-108] Besides, as shown by the more transparent structures in Figure 13, the cations in the next building block at the back closely pack with the cations in the front building block due to the π-π stacking interaction between the imidazolium rings.[28, 46, 109] The negative charge density on the fresh mica surface after K^+ are dissolved by absorbed water is approximately one per 0.47 nm^2 on average,[84, 110, 111] and the IL cations need to occupy the empty spots left by the K^+ to preserve electroneutrality. Taking into consideration of the area covered by the two cations in one building block and the range of the π-π stacking interaction between two blocks, the surface area of mica covered by one building block is approximately the same as the area of two negative charges. The sizes of two cations (~0.5 nm each) and one anion (~0.7 nm) in the z-direction account for the overall thickness of a building block. As a result, the thickness of the double-layering molecular structure of the IL nanofilms is ~1.7 nm, which is also close to the thickness of 2ML in the cubic model approximation of bulk molecules.

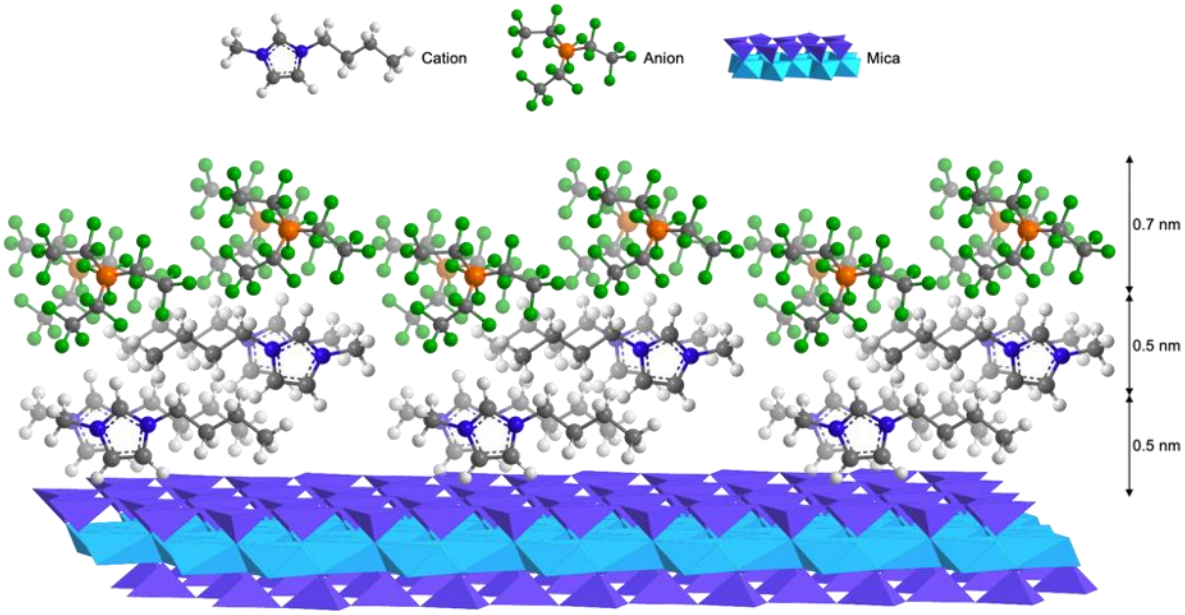

Figure 13. Double-layering interfacial structure of IL molecules on the mica surface.

3.3.3 Different Spreading Kinetics of ILs on Mica

It has been demonstrated that the alkyl chain length in the IL cations has no impact on the thermodynamic equilibrium states of the nanofilm morphology because of the double-layering interfacial structure of IL cations and anions on mica. Meanwhile, it has also been found that the spreading of the [Hmim][FAP] films is the slowest among the series of IL films. It is worth further investigating the effect of the alkyl chain length in the IL cations on the spreading kinetics of mica-confined ILs.

[Emim][FAP], [Bmim][FAP], and [Hmim][FAP] nanofilms were fabricated from the same solution concentration of 0.75 g/L and compared with respect to the lead time after the thin film fabrication. The films were fabricated, characterized, and stored under the RH lower than 20% the whole time. While absorbed water forms large island-like films to full monolayers at RH > 30%,

only small and isolated two-dimensional clusters can be formed on the mica surface at RH < 20%, and the mobility of K^+ is low.[76, 84, 86, 112] It was also previously reported that the initial molecular structure of [Bmim][FAP] gradually changes from droplets to extended layers with increasing RH.[44] In light of this, it is expected that the IL film morphology at the initial stages could change from extended layering at RH > 30% to nanodroplets at RH < 20%. Accordingly, RH < 20% was chosen here.

The AFM images and the corresponding line profiles in Figure 14 display the time-dependent nanofilm morphology of [Emim][FAP] fabricated from the concentration of 0.75 g/L under RH < 20%. The nanofilm behaves as sponge-like layering at the initial state (within half an hour after thin film fabrication), same as the morphology under RH > 30%. While the mobility of K^+ is low, the spreading process for the [Emim][FAP] nanofilm could happen instantly after dipcoating, so only layering structure was observed. No change of the molecular structure was observed, and the RMS surface roughness values remain almost the same at various lead time (Table 4). The molecular structure remained as sponge-like layering, and the nanofilm thickness was constant at ~2 ML for up to one week.

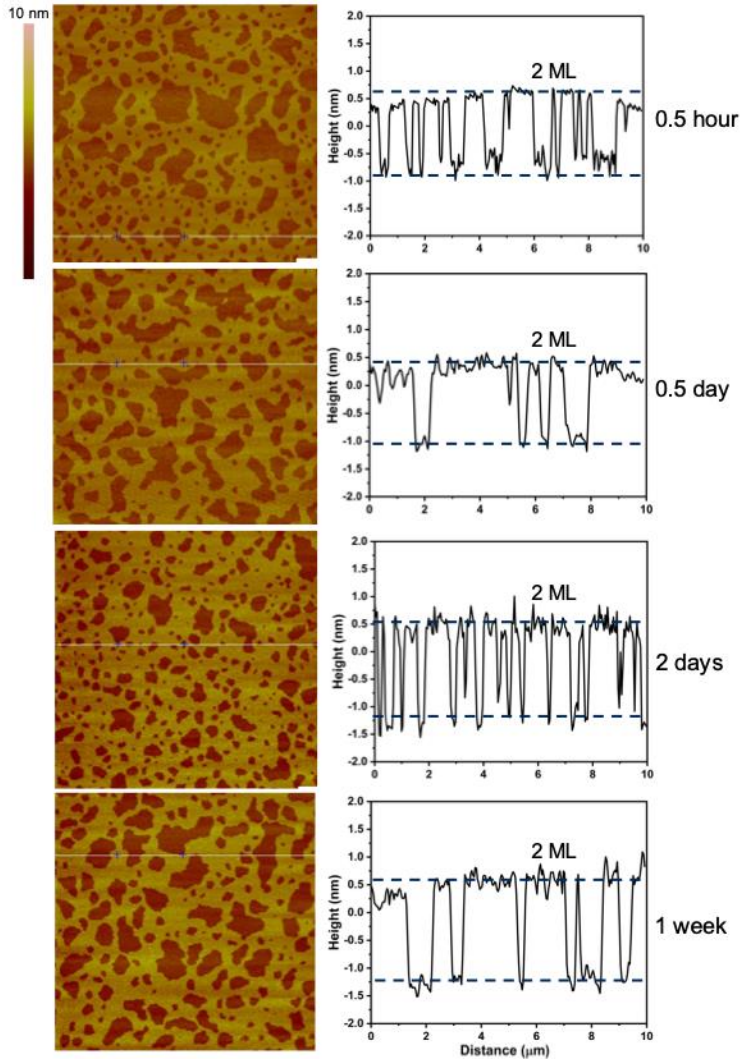

Figure 14. AFM images and their corresponding line profiles of time-dependent nanofilms of [Emim][FAP] fabricated from the concentration of 0.75 g/L. The RH was lower than 20% the whole time. The AFM scan areas are 10 μm by 10 μm, and the inset scale bar is for the z-direction. The x-axis and y-axis for the line profiles are the distance along the cut in the horizontal direction (μm) and the height in the vertical direction (nm), respectively.

Table 4. RMS surface roughness results of the three IL nanofilms fabricated from the concentration of 0.75 g/L at various lead time

	0.5 hr	0.5 day	2 days	1 week	3 weeks
[Emim][FAP]	0.496 nm	0.588 nm	0.794 nm	0.826 nm	
[Bmim][FAP]	2.44 nm	2.16 nm	1.54 nm	0.897 nm	
[Hmim][FAP]	7.01 nm	9.03 nm	4.13 nm	1.49 nm	0.608 nm

As expected, a combination of nanodroplets and layering nanofilms with heights of up to ~10 nm was observed at the initial state for the [Bmim][FAP] nanofilm fabricated from the concentration of 0.75 g/L (Figure 15a). The nanodroplet molecular structure at the initial state under RH < 20% is very different from the sponge-like layering molecular structure under RH > 30% due to the low mobility of K^+, although fast spreading may have already occurred before 0.5 hour. The nanodroplets then start to spread gradually over time, as indicated by the AFM topography and the RMS surface roughness values. At this stage of isotropic spreading, the height of the nanodroplets decreases over time, and the coverage of the nanofilm on mica increases over time. It's worth noting that when the film thickness is above 4 ML, i.e., after 0.5 hour and 0.5 day, the height of the films at various locations are not uniform anymore, possibly because the layering structure away from the solid/liquid interface is dampened. The film morphology changes from nanodroplets with irregular shapes to islands with a constant thickness of ~4 ML after 2 days. Eventually, after one week, the islands spread anisotropically to connect into layering nanofilm with a constant thickness of ~2 ML. The significantly lower mobility and slower spreading of

mica-confined [Bmim][FAP] nanodroplets compared to the spreading in macroscale is also analogous to the previous finding.[91]

For the [Hmim][FAP] nanofilm fabricated from the concentration of 0.75 g/L, only nanodroplets with heights up to ~50 nm were observed at the initial state under RH < 20%, as shown in Figure 15b. The nanodroplets then start to spread isotropically over time to cover more mica areas. However, the spreading of [Hmim][FAP] nanodroplets is much slower than the spreading of [Bmim][FAP] nanodroplets, as indicated by the comparison of AFM topography in Figure 15 and the RMS surface roughness values in Table 4 at various lead time. Besides, the solid/liquid contact lines of [Hmim][FAP] nanodroplets are closer to circles than the contact lines of [Bmim][FAP], since the cohesion interaction within the [Hmim][FAP] molecules with C_6 alkyl chain tails dominate over the templating effect at the solid/liquid interface at these stages. After one week, the film morphology slowly changes from nanodroplets to large islands with a constant thickness of ~4 ML. Interestingly, it was noticed that a layer with a thickness of ~2 ML develops under another layer with a thickness of ~2 ML at the edge of an island, as shown in Figure 16. This phenomenon indicates that the morphology of the [Hmim][FAP] nanofilm after one week may not be at its equilibrium state yet, and the nanofilm still has the tendency to spread slowly. Eventually, after three weeks, the islands spread anisotropically to connect into layering nanofilm with a constant thickness of ~2 ML (Figure 15b).

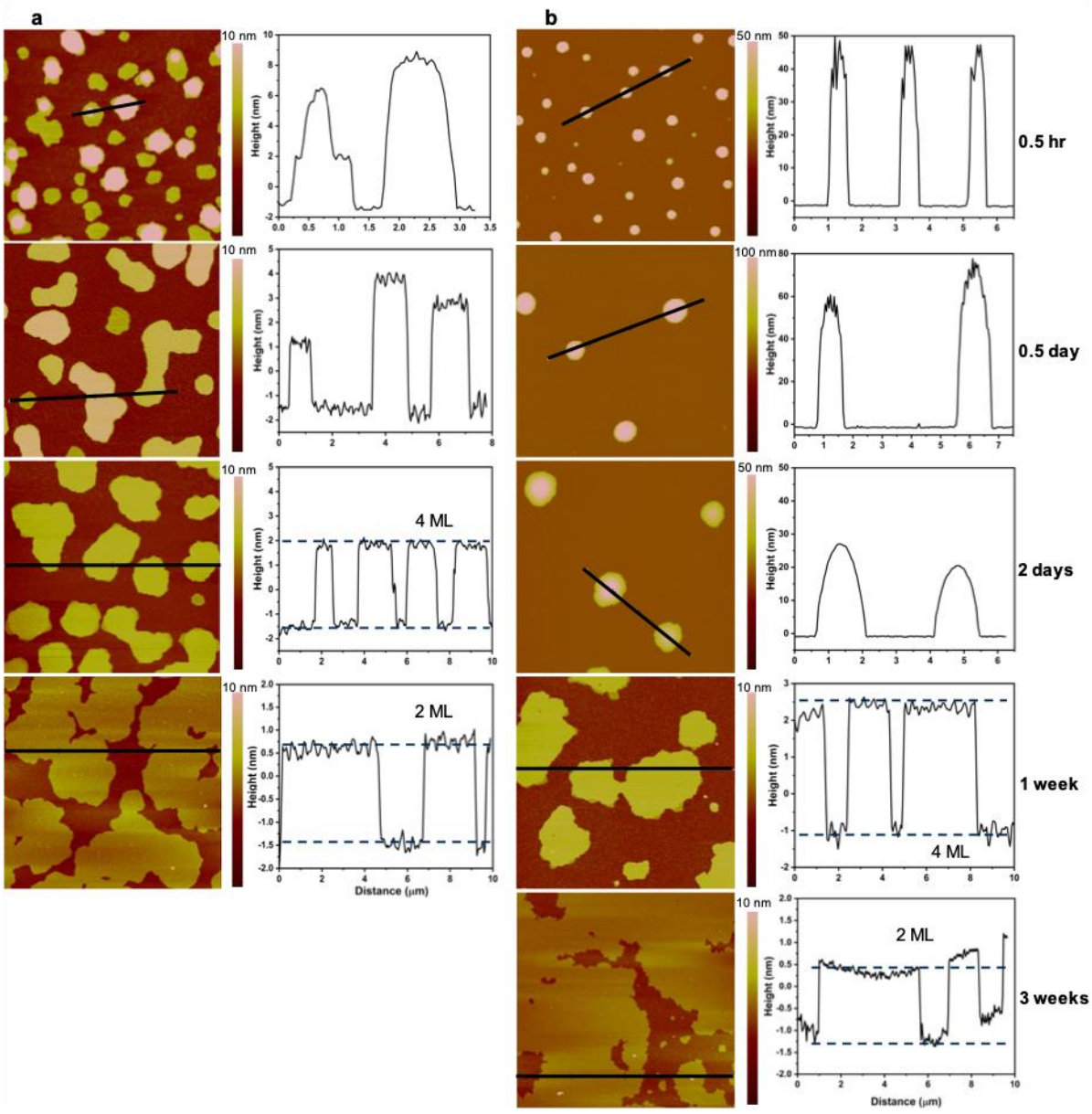

Figure 15. AFM images and their corresponding line profiles of time-dependent nanofilms of (a) [Bmim][FAP] and (b) [Hmim][FAP] fabricated from the concentration of 0.75 g/L. All AFM scan areas are 10 μm by 10 μm, and the inset scale bars are for the z-direction. The x-axis and y-axis for the line profiles are the distance along the cut in the horizontal direction (μm) and the height in the vertical direction (nm), respectively.

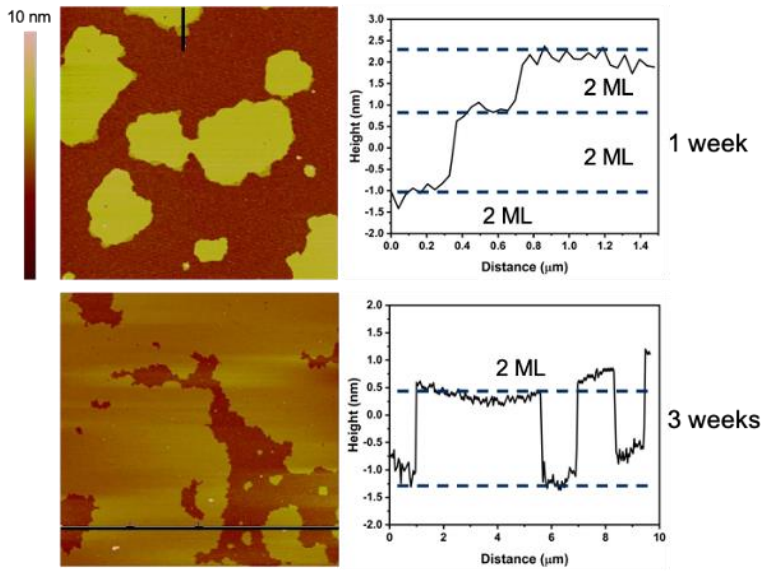

Figure 16. AFM images and their corresponding line profiles of mica-confined [Hmim][FAP] fabricated from the concentration of 0.75 g/L. The scans were taken 1 week and 3 weeks after the sample fabrications, and the RH was lower than 20% the whole time. The AFM scan areas are 10 μm by 10 μm, and the inset scale bar is for the z-direction.

The time-dependent AFM results under RH < 20% demonstrate a clear dependence of the spreading kinetics of mica-confined ILs on the cation alkyl chain length. The spreading of the nanofilm of [Emim][FAP], which has the shortest alkyl chain, is the fastest among the three IL nanofilms. The dispersive interaction of the C_2 alkyl chains is too week to preserve a strong cohesion within the IL molecules, so the solid/liquid interfacial interaction dominates from the beginning. The spreading of the [Bmim][FAP] nanofilm is slower than the [Emim][FAP] nanofilm. A distinct change of surface morphology with lead time, i.e., from the combination of nanodroplets and layering islands after half an hour to smooth layering films after one week, has been noticed. The mild dispersive interaction of the C_4 alkyl chains is able to compete with the templating effect on the mica surface, so the mobility of the nanodroplets is low. The spreading of

the [Hmim][FAP] nanofilm is the slowest among the three IL nanofilms. It takes up to three weeks for the nanofilm to reach its equilibrium state of the smooth layer of 2 ML thick. As [Hmim][FAP] has the longest C_6 alkyl chain in the cation, the intermolecular cohesion is strong enough to preserve the nanodroplet structure with the shape of a spherical cap for the longest time among the three ILs.

3.4 Conclusions

In conclusion, the interfacial molecular structures of mica-confined ILs with various alkyl chain lengths in the cations, i.e., [Emim][FAP], [Bmim][FAP], and [Hmim][FAP], have been systematically investigated by AFM. Quantized growths of the nanofilms of [Emim][FAP] and [Bmim][FAP] at RH > 30% have been directly observed. Initially, the IL films only cover more solid surface areas at the constant film thickness of 2 ML. Then a quantized increase in the film thickness by 2 ML was observed. The nanofilm thickness remains constant afterward as the nanofilm grows. The AFM thickness results directly indicate that the cation alkyl chain length has no impact on the thermodynamic equilibrium states of the nanofilm topographies. As a result, we have proposed a double-layering interfacial molecular arrangement of IL cations and anions on the mica surface. Within the building block, the first two layers adjacent to the mica surface are cation layers with the imidazolium rings perpendicular to mica and the closely-packed alkyl tails parallel to mica, and two anions sit on top of the two cations. Meanwhile, the time-dependent AFM results at RH < 20% reveal the effect of the cation alkyl chain length on the spreading kinetics of mica-confined IL nanofilms. The spreading is slower for ILs with longer alkyl chains due to the stronger

intermolecular dispersive interactions. Our results provide direct proofs and detailed insights into the molecular structures of ILs confined on solid surfaces.

4.0 Nanometer-Thick Fluorinated Ionic Liquid Films as Lubricants in Data-Storage Devices

The material in this chapter is based upon the published work *ACS Appl. Nano Mater.* 2019, 2, 8, 5260–5265.[13]

4.1 Introduction

The physical contact between adjacent solid surfaces has been a huge concern for many nanoscale devices with contacting components during operation, as it could cause the failure of the device. The application of nanometer-thick lubricants is of vital importance to the efficiency and reliability of these devices.[36, 37] For instance, the head-media spacing (HMS) between the flying magnetic head and the spinning magnetic media (~10 m/s^2) is only ~10 nm in a HDD, the state-of-the-art data storage device.[11, 113] Smaller grain sizes induce higher areal density, which also results in weaker magnetic flux. As the reading and writing processes are highly sensitive to HMS, reduced HMS is required to optimize the signal as the areal density increases.[114, 115] Based on the historic trend by Advanced Storage Technology Consortium (ASTC), the HMS is as low as 7 nm in order to reach the areal density milestone of 1 Tbit/in^2 (Tbpsi).[116, 117] The HMS target is even approaching 5-6 nm to reach the areal density target of 2 Tbpsi and 4-5 nm to reach the areal density target of 4 Tbpsi.[116] In order to reduce direct head-media contact and protect the magnetic media from wear, nanometer-thick lubricants need to be applied on the surface of the media.[118, 119] Another example is the NEMS/MEMS. In such systems, it has been reported that adhesion is one

of the major sources of breakdown in a digital micromirror device, and that wear detrimentally affects the data storage system of NEMS-based AFM.[39, 120] Ultrathin lubricants are coated on the surfaces of the NEMS/MEMS devices for better tribological performance. There are several requirements for nanometer-thick lubricants. The lubricant should be load-carrying and have good mobility for self-healing capability. Additionally, having enough perfluorinated components in the molecules is necessary to ensure low surface tension of the molecules, which results in both low friction and low contamination. Moreover, the lubricant should have good thermal stability since tribology contact always increases the temperature at the interface. Last but not least, the thickness of the lubricant should be as low as possible since the areal density of HDD increases with the decrease of the HMS. The minimum thickness of the nanometer-thick lubricants is determined by the ML of the molecules.[121] The nanometer-thick lubricants currently used in HDD industry are PFPEs because of their low surface tension and excellent tribological properties.[11, 88, 122] However, with the continuous decease in HMS due to the need of higher areal density, the characteristic ML thickness of these lubricant films are not low enough. The large radius of gyration of the polymer chain of PFPEs is a primary limiting factor here.[119, 123, 124]

ILs are promising candidates for the next-generation lubricants due to their extraordinary properties. Bhushan et al. reported that the robust thermal conductivity of ILs is good for heat dissipation at the contacting inteface.[125] Valkenburg et al. found that the ions in ILs help reduce the electrical resistance,[126] which is beneficial for NEMS/MEMS.[39] Many commercially available ILs contain fluorinated segments in their anions. Such fluorinated ILs have low surface tension, which induces promising tribological performance and corrosion protection.[15, 35] Most ILs are also more cost-effective than PFPEs. Moreover, as a group of "designer materials",[3] the molecular structures of ILs can be readily tailored by manipulating the ion pairs based on the desired

molecular sizes and physiochemical properties. Importantly, many ILs showed better thermal stability over PFPEs, which is highly desirable for lubrication in HAMR.[11] The high thermal stability of the ILs can be attributed to their unique chemical structures. The strong electrostatic interaction between the cations and anions results in the low volatility and high thermal degradation temperature. The aromatic imidazolium rings from the cations also increase the packing efficiency and enhance electrostatic interactions.[11] The layering structure of ILs at the IL/solid interfaces is also ideal for lubrication, and the mechanisms have been extensively studied. Gong et al. concluded that ultrathin ILs form solid-like molecular layers on charged solids, e.g. silica and mica, which has been attributed to the electrostatic attraction between the negative-charged solids and the IL cations.[127 44, 128] More relevant to HDD, parallel packing of imidazolium cations on the surface of amorphous carbon, the substrate of media lubricants in HDDs, was also reported based on "cross-section" AFM study and has been attributed to the π - π^+ stacking.[46, 129] The most important characteristic of ILs for HDD media lubrication might be that the molecular size of ILs is much smaller than that of PFPEs,[101, 127] which makes it possible to achieve lower ML and thus higher areal density. Nonetheless, to date, no research has been carried out to verify this critical hypothesis, which could lead to the next-generation media lubricants.

In this paper, we evaluated the ML thickness of [Bmim][FAP], a commonly utilized IL with imidazolium cations and fluorinated anions, with Z-tetraol, the state-of-the-art PFPE, as control. The AFM surface roughness analysis and the friction results revealed that the ML thickness of [Bmim][FAP] is only about half of that of Z-tetraol, which is attributed to the smaller size of the IL molecule than the PFPE molecule. Our results also indicated that [Bmim][FAP] has higher thermal stability than Z-tetraol. The findings here suggested that fluorinated ILs are promising candidates as next-generation media lubricants for HDDs.

4.2 Experimental Section

4.2.1 Materials

The IL studied is 1-butyl-3-methylimidazolium tris-(pentafluoroethyl)trifluorophosphate ([Bmim][FAP], high purity >99%). It was obtained from EMD Millipore Corporation and used as received. [Bmim][FAP] contains imidazolium cations and fluorinated anions. It is worth noting that [Bmim][FAP] is very hydrophobic, with the bulk water content of only 276 ppm. Even after exposure under 99% RH for 12 hours, the water content is still as low as 326 ppm.[44] The diameter of the IL ion pair (d_m) is 0.84 nm.[101] The vapor pressure of [Bmim][FAP] is extremely low and too challenging to be measured.[130] The state-of-the-art PFPE studied is Z-tetraol ($M_n \approx 2000$ g/mol), purchased from Solvay Solexis Inc. and utilized as received. Z-tetraol has four hydroxyl end groups, and is one of the most widely used PFPEs.[11] The characteristic size of the PFPE molecule, the radius of gyration (R_g), is 1.5 nm.[131] The vapor pressure of the PFPE is as low as 4×10^{-8} torr at 20°C.[132] The chemical structures and dimensions of both [Bmim][FAP] and Z-tetraol are presented in Figure 17. The solvent used for both the IL and the PFPE is 2,3-dihydrodecafluoropentane (commercially known as Vertrel XF). This was obtained from Miller-Stephenson Chemical Company and used as received. The substrate used is an amorphous carbon with sp^2 and sp^3 hybridization, i.e., carbon overcoat (COC), on which the nanometer-thick lubricant is applied in the HDDs. A 3 nm thick carbon film is deposited by a PECVD process on a NiP/aluminum substrate or a metalized (CrTa-based) glass substrate. The surface region of the carbon film, about a few Å in depth, is enriched with nitrogen to promote the bonding of lubricants. Glass COC was used for all characterizations except measurement of film thickness, where aluminum COC was used instead.

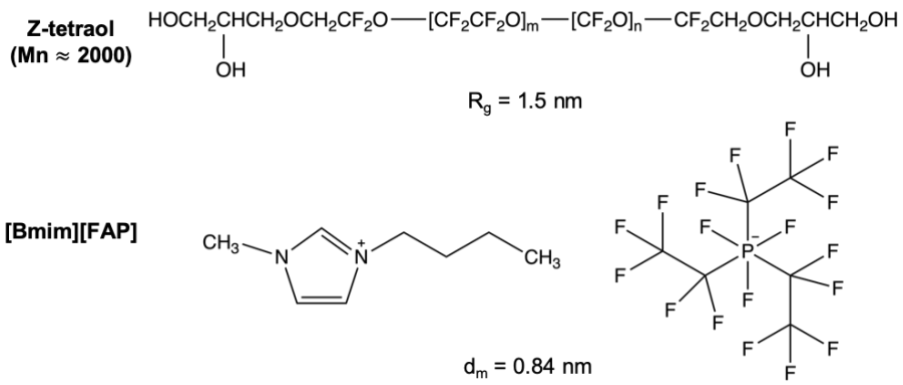

Figure 17. Chemical structures of [Bmim][FAP] and Z-tetraol.

4.2.2 Fabrication of Nanometer-Thick Films

Solutions were made by dissolving [Bmim][FAP] or Z-tetraol in Vertrel XF in varying concentrations. Both solutes easily dissolve in the solvent. These solutions were used to apply a thin film to the substrates used by utilizing a dipcoating procedure, already used in the HDD industry.[88, 89] In this procedure, the substrate was dipped into the solution at a rate of 60 mm/min, and removed at the same rate. The solvent then evaporated, leaving behind a thin film of IL or PFPE. The thickness of this film was controlled by changing the concentration of the solution based on our previous report.[11]

Solutions were made by dissolving [Bmim][FAP] or Z-tetraol in Vertrel XF in varying concentrations. Both solutes easily dissolve in the solvent. These solutions were used to apply a thin film to the substrates used by utilizing a dipcoating procedure, already used in the HDD industry.[88, 89] In this procedure, the substrate was dipped into the solution at a rate of 60 mm/min, and removed at the same rate. The solvent then evaporated, leaving behind a thin film of IL or

PFPE. The thickness of this film was controlled by changing the concentration of the solution based on our previous report.[11]

Nanofilm thickness was measured with an Alpha-SE (J. A. Woollam Co.) spectroscopic ellipsometer. The incident angle was 70° and the wavelength range was 380-900 nm. Data analysis was conducted with vendor-supplied software, CompleteEASE. The uncoated aluminum COC samples were tested initially to determine the thickness of the COC layer before the coating was added. The coated samples were then tested to determine the thickness of the nanofilms. At least three trials were completed for each sample. Optical constants used to calculate the thickness were determined with the Cauchy dispersion equation:

$$n(\lambda) = A + \frac{B}{\lambda^2} \tag{4-1}$$

where n is the refractive index, λ is the wavelength in microns, and A and B are constants that vary with the coating composition. A is 1.45 for ILs and 1.30 for PFPEs, and B is 0.0025 for both ILs and PFPEs. As shown in Figure 18, the thickness of the fabricated nanofilms, measured with an ellipsometer, increased proportionally with the concentration of the bulk solutions within the investigated range of the nanofilm thickness, which is consistent with previous reports[88, 133].

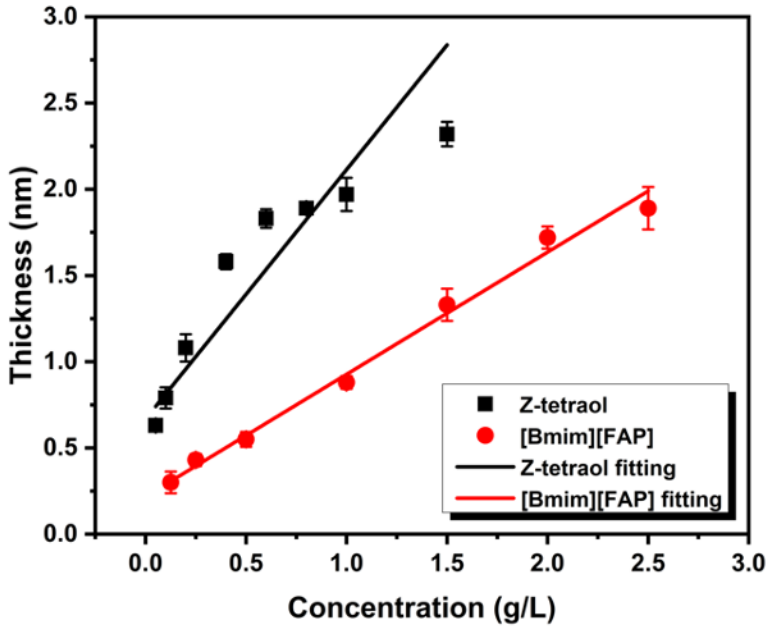

Figure 18. Nanofilm thickness of [Bmim][FAP] and Z-tetraol on COC at various concentrations.

4.2.3 Other Characterizations

AFM imaging was conducted to investigate the surface topography and roughness of the nanofilms on COC. The scans were performed at tapping mode with a Veeco Dimension V Scanning Probe Microscope (image acquisition, 256 by 256 pixels; vertical resolution, 0.1 nm). The AFM probe utilized has an aluminum tip on a n-type silicon cantilever (MikroMasch NSC14/AL BS; resonance frequency, 160 kHz; force constant, 5.0 N/m; tip radius, 8 nm). The scan size was 10 μm by 10 μm for all scans, which determined the lateral resolution of 39 nm at 256 pixels.

Friction tests were performed with a CSM Instruments Nanotribometer (NTR^2) on top of a Kinetic Systems antivibration platform. Friction force and normal force were measured with a dual

beam cantilever and high-resolution capacitive sensors. The counterface used was a 2 mm diameter stainless steel sphere, which was cleaned with isopropanol between trials. For each trial, the normal load was 10 mN, the maximum linear speed was 0.20 cm/s, the half amplitude was 1.00 mm, and 50 cycles were performed. The tests were conducted at 20-22 °C and 6-50% relative humidity. At least three measurements were recorded for each sample, and the average coefficient of friction (COF) and the standard deviation are reported. The COF traces are recorded in Figure 19, where one trial for each nanometer-thick film is randomly selected to be displayed.

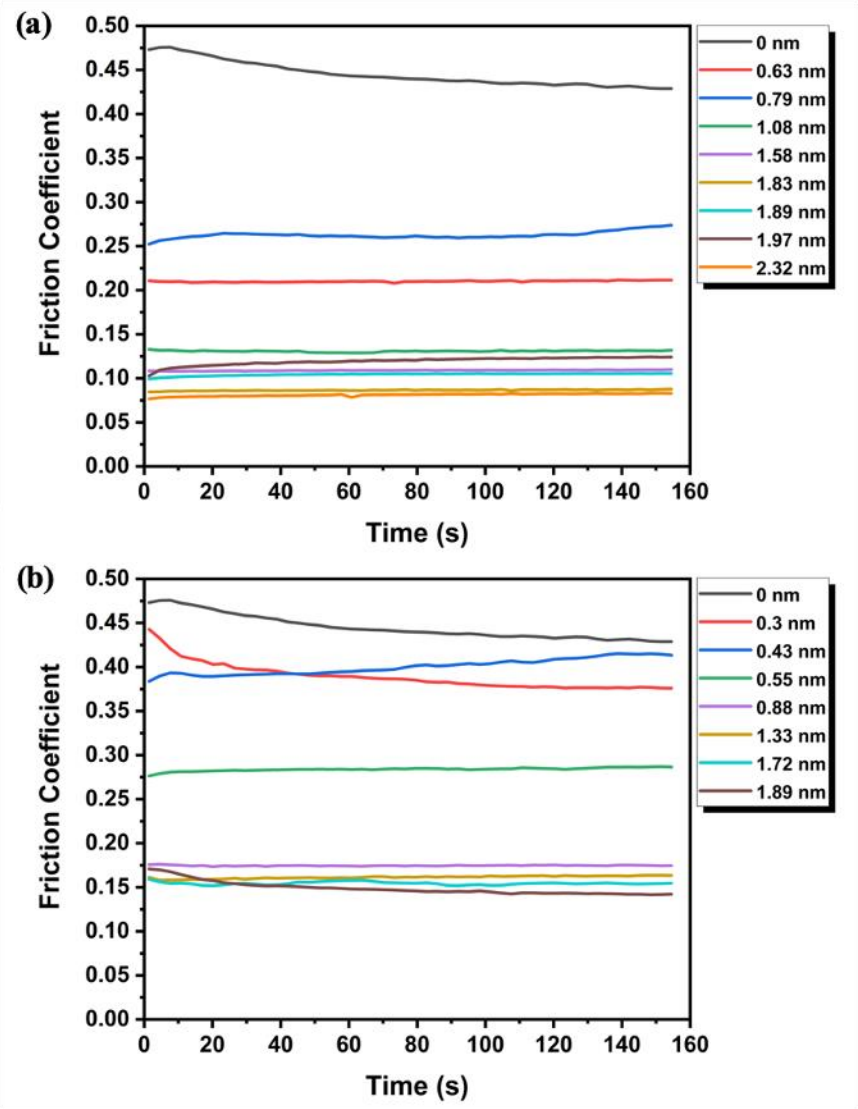

Figure 19. Friction traces of (a) Z-tetraol and (b) [Bmim][FAP] with varying thicknesses on COC. One trial is randomly selected to be displayed for each nanometer-thick film.

Thermogravimetric analysis (TGA) was performed to determine the thermal stability of the bulk [Bmim][FAP] and Z-tetraol. These tests were conducted with a SEIKO-220 TG system, using sample weight around 25 mg in aluminum pans. The samples were heated from room temperature to 600 °C at a heating rate of 10 °C/min in 94% N_2/6% O_2. The weight percentage of the remaining sample is plotted against the heating temperature. As shown in Figure 20, [Bmim][FAP] has

significantly higher thermal stability than Z-tetraol. The weight loss of [Bmim][FAP] started at a temperature higher than 300 °C, which was almost 200 °C higher than that of Z-tetraol. [Bmim][FAP] reached 50% of its initial weight at ~425 °C, which was also higher compared to Z-tetraol.

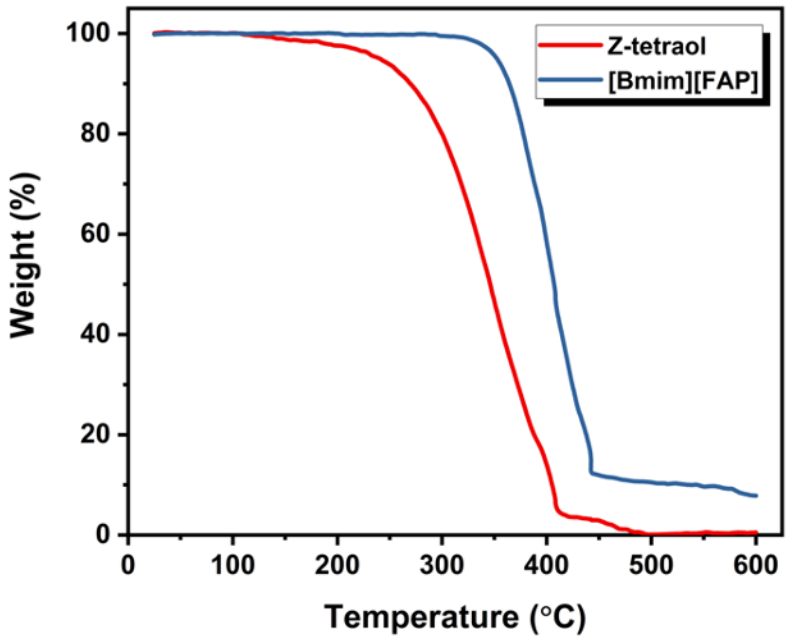

Figure 20. TGA results of the bulk IL and PFPE.

To understand the bonding interactions between the lubricant, i.e., [Bmim][FAP] or Z-tetraol, and COC, the coated media was washed with Vertrel XF based on a previously established procedure in our lab.[89] During this procedure, the coated media was dipped into and withdrawn from Vertrel XF at a rate of 60 mm/min. The thickness of the remaining lubricant left on COC was then determined by ellipsometry.

4.3 Results and Discussion

4.3.1 Monolayer Thickness Determined by Surface Roughness

In the current study, we found that there is a close relationship between the surface roughness and the lubricant thickness with respect to the ML thickness. Based on this, we have determined the ML thickness of both [Bmim][FAP] and Z-tetraol on COC and found that the ML thickness of the IL is only ~ 50% of that of the PFPE.

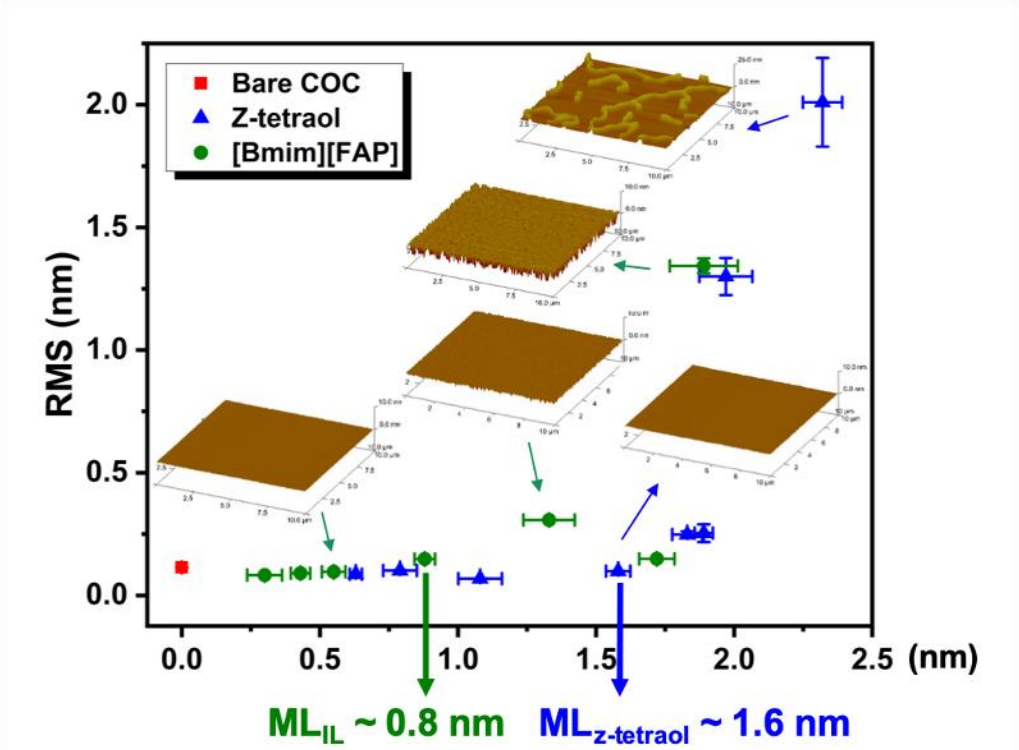

Figure 21. RMS of the nanometer-thick films with varying thicknesses on COC.

ML thickness of both [Bmim][FAP] and Z-tetraol have been determined by means of AFM surface roughness analysis. Figure 21 shows the surface roughness results and the corresponding

AFM images of [Bmim][FAP] and Z-tetraol with different thicknesses on COC. A scan size of 10 μm by 10 μm was standard for all the scans. The AFM images of all the investigated surfaces are also available in Figure 22. Bare COC was used as the control. Root mean squared roughness, RMS, was used as the surface roughness parameter. Nanofilm thickness was controlled by varying the concentration of solutions and measured with an ellipsometer. For Z-tetraol, the surface roughness of the nanofilms was comparable to the 0.114 nm roughness of bare COC until the film thickness approached 1.6 nm. As further confirmed by the AFM images, no dewetting was detected when the thickness was below 1.6 nm. It is worth noting, however, that the lateral resolution in the AFM images is 39 nm, as compared to the vertical resolution of 0.1 nm. The smooth surface below the ML thickness under AFM does not necessarily indicate uniform film coverage because the lateral features smaller than the pixel size cannot be detected. The macroscale lateral scan area was also much bigger than the Ångstrom-scale vertical features. At this Z-tetraol submonolayer regime, a decrease in the surface free energy with increasing film thickness was discovered previously, which results from the favorable bonding of the hydroxyl end groups with the polar sites on COC.[38] When the nanofilm thickness exceeded the ML, the surface roughness increased dramatically. Previous study showed that the surface free energy starts to increase at this stage as a result of the noninteracting hydroxyl end groups of Z-tetraol, where the interaction within Z-tetraol dominated over the solid-liquid interaction (i.e., dewetting occurs).[38] As shown in Figure 21, dewetting was clearly observed by AFM for the film with thickness above 1.6 nm for Z-tetraol. Therefore, 1.6 nm is determined to be the ML thickness of Z-tetraol. Moreover, R_g of Z-tetraol was reported to be 1.5 nm[131], which is comparable with the ML thickness.

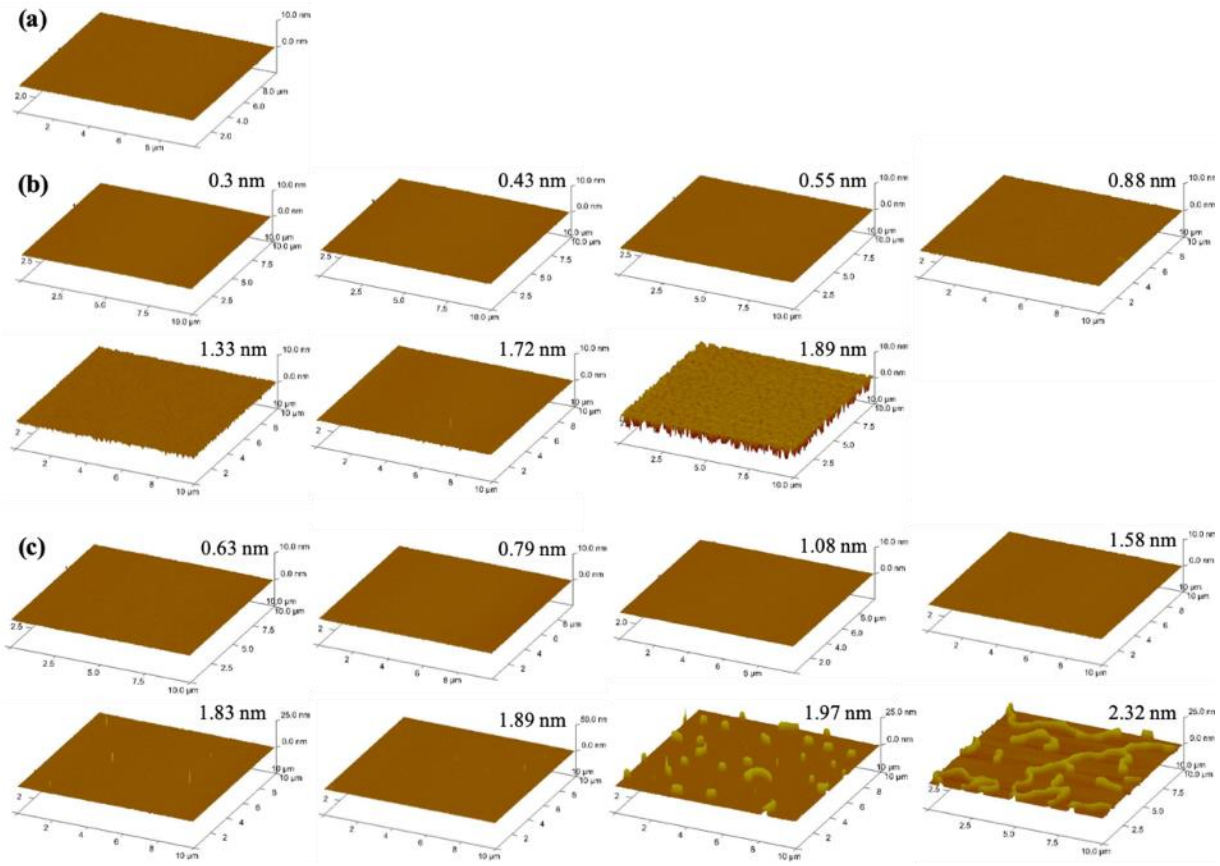

Figure 22. AFM images of (a) bare COC, (b) [Bmim][FAP], and (c) Z-tetraol with different thicknesses on COC.

For [Bmim][FAP], the AFM roughness results revealed that the surface remained very smooth for film thinner than 0.8 nm. Therefore, 0.8 nm is determined to be the ML thickness of [Bmim][FAP]. The layering structure of ILs with imidazolium cations at the IL/COC interfaces was reported in the previous studies.[46, 134] IL cations orient horizontally on COC due to the π - π^+ interaction between the π electrons from the sp^2 carbon on the surface of COC and the delocalized π^+ electrons from the imidazolium rings of ILs. The π - π^+ stacking thus triggers the layering of cations and anions in the vertical direction. The thickness of the first layer of the ion pairs is referred to the ML thickness of the IL. The surface became rougher with the thickness of film

above ~0.8 nm initially, while it became smoother again when the film thickness approached ~1.7 nm. This was where the second ML covered the underlying ML completely. As the film thickness exceed 2 ML, the surface roughness became much higher, which can be attributed to the dominating cohesion of the IL ions over IL/COC interaction with the increase of the IL thickness.[127] As indicated in equation (4-2), the ML of [Bmim][FAP] can also be estimated from the bulk molar volume V_m of the IL ion pair.[92, 127] If the physical shape of each IL ion pair is assumed to be cubic, V_m can be determined from the molar weight M (584.23 g/mol), the bulk density ρ (1.63 g/cm^3 at 293 K), and the Avogadro constant N_A. Accordingly, the ML of [Bmim][FAP] is calculated to be 0.841 nm, which is very consistent with the result from the surface roughness study.

$$ML = V_m^{\frac{1}{3}} = \left(\frac{M/N_A}{\rho}\right)^{\frac{1}{3}} \quad (4\text{-}2)$$

Usually, AFM only provides the topographic information on how rough the nanofilm surfaces are based on the images and the corresponding RMS roughness values. However, when the nanofilm is thicker than the ML, there is a sharp increase in RMS and clear dewetting can be observed from the AFM images. Therefore, the ML thickness can be determined by the onset of the sharp increase in RMS by AFM. Our results showed that the ML thickness of [Bmim][FAP] is only about half of that of Z-tetraol, which can be attributed to the fact that [Bmim][FAP] has a smaller molecular size than polymeric Z-tetraol. The thinner ML of the IL lubricant provides the opportunity to further scale down HMS and hence ramp up the areal density. At the areal density range of >1 Tbpsi and the HMS range of <7 nm, ~1 nm decrease in HMS results in doubling of the areal density.[116]

4.3.2 Monolayer Thickness Determined by Friction

The friction measurement of the IL and PFPE, varying in film thicknesses on COC, was conducted. The standard testing duration, normal load, and the linear speed was 50 cycles, 10 mN, and 0.20 cm/s, respectively. As shown in Figure 23, the COF of the Z-tetraol nanofilms was higher than 0.2 when the films were thinner than 1.6 nm. For films thicker than 1.6 nm, the COF started to stabilize at ~ 0.1, which indicates that the 1.6 nm nanofilms efficiently covered the entire COC surface. Therefore, the ML thickness of Z-tetraol was determined to be 1.6 nm, which is consistent with what was determined by surface roughness (See Figure 21). For [Bmim][FAP], the COF of thinner films was similar to that of bare COC without any lubricants, while it dropped down to ~ 0.15 and leveled off when the films were thicker than 0.8 nm, which corresponds to the ML thickness of [Bmim][FAP] and echoes the surface roughness results. Accordingly, the friction results here provide strong support to the surface roughness results that the ML thickness of [Bmim][FAP] is only about half of that of Z-tetraol. The COF of the ML of Z-tetraol and [Bmim][FAP] on COC under longer testing duration, higher normal load, and faster linear speed were recorded in Figure 24. Little changes in the COF were observed compared to the COF recorded with the standard parameters, and the surfaces remained smooth after long-duration tests under optical microscope images of the MLs taken before and after the long-duration tests, indicating excellent durability and wear-resistance of the nanometer-thick lubricants.

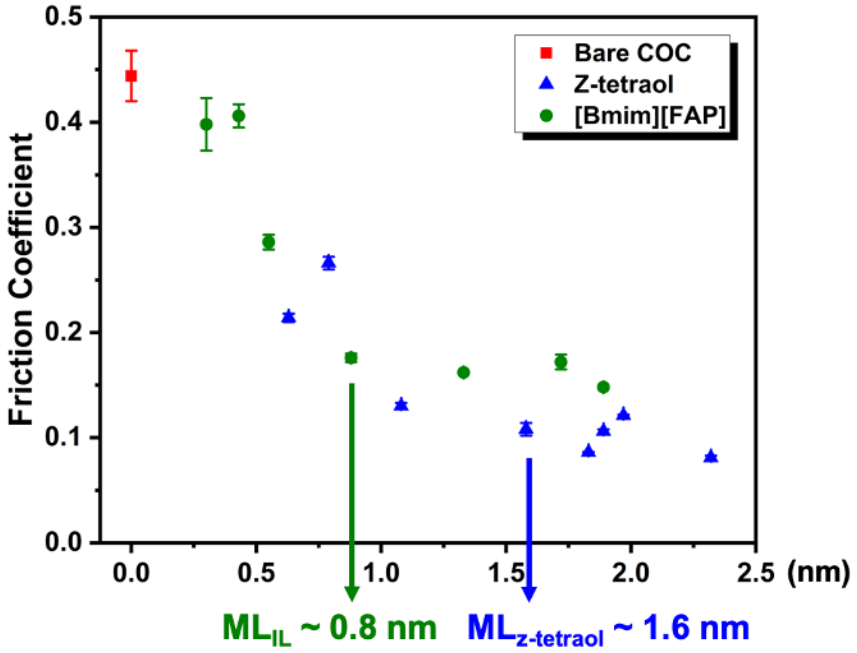

Figure 23. COF of the nanometer-thick films with varying thicknesses on COC.

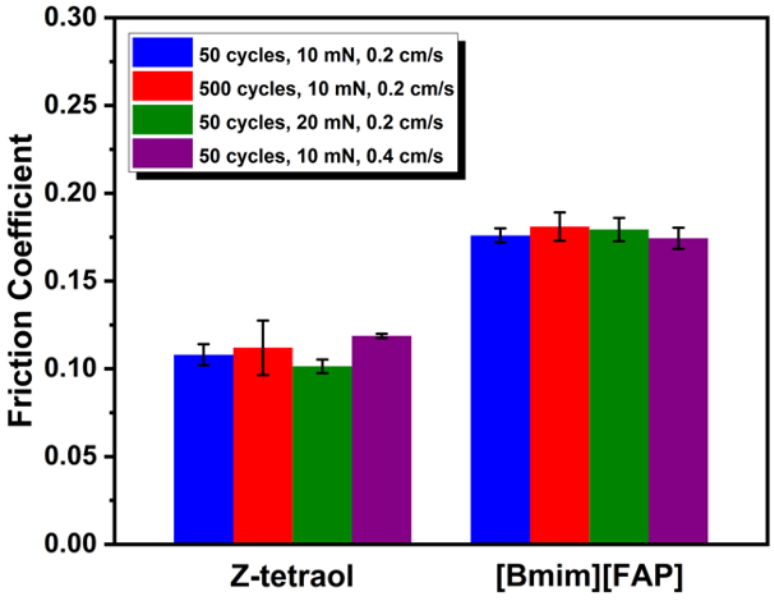

Figure 24. COF of the ML of Z-tetraol and [Bmim][FAP] on COC at different duration, normal load, and maximum linear speed. Standard testing parameters are 50 cycles, 10 mN, and 0.2 cm/s.

The friction test results show that [Bmim][FAP] is a promising candidate as a nanometer-thick media lubricant for HDDs due to its potential to reduce the lubricant thickness as well as its robust tribological property. Nevertheless, its COF was still slightly higher than that of the PFPE at the stable regime. On the one hand, the higher COF of [Bmim][FAP] is associated with its higher surface tension. The surface tension of Z-tetraol is 22.4 mN/m,[135] while the surface tension of [Bmim][FAP] is 32.4 mN/m from pendant drop analysis. The higher surface tension of the IL can be attributed to fewer CF_x groups in its chemical structure.[15] On the other hand, the bonding of the IL to the substrate was much weaker than that of the PFPE. Figure 25 shows the difference between the thickness of the nanometer-thick films before and after Vertrel washing. Vertrel washing was operated following similar procedures to dipcoating except using coated samples and pure Vertrel instead of bare COC and solutions. The IL nanofilms barely survived washing in all concentrations, and the COF increased significantly based on Figure 26. The intermolecular interaction at the IL/COC interface was too weak to survive Vertrel washing because the IL molecules do not have functional end groups. The high mobile fraction of the IL nanofilm caused more direct contact of the counterface to the hard COC surface during tribology tests, which led to higher COF.[136] In contrast, only a slight decrease in thickness and a slight increase in COF were observed after washing for the Z-tetraol nanofilms, as the hydrogen bonding between Z-tetraol and COC was stronger.[89] The ideal bonded and mobile ratio led to lower COF. For future improvement, the next-generation IL lubricants need to have more fluorinated components and hydroxyl groups in the alkyl chains of the cations to reduce the surface tension and enhance the bonding to solid substrates.

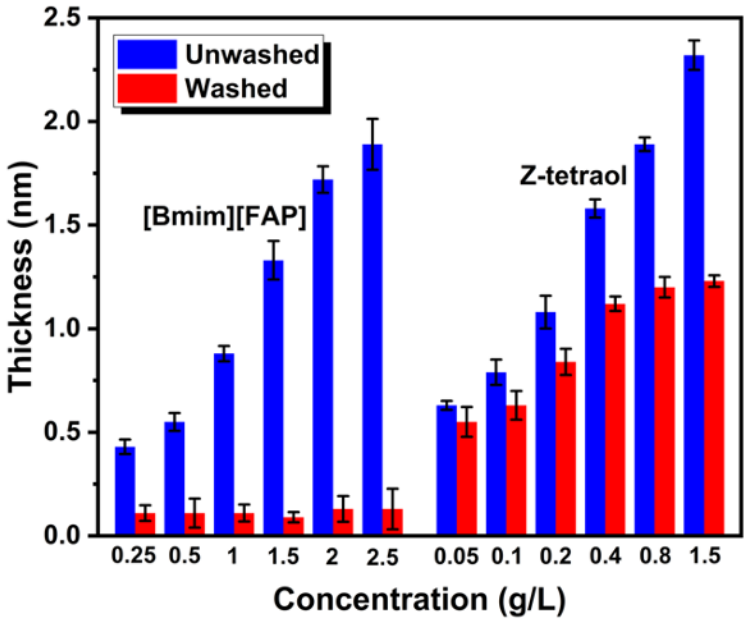

Figure 25. Bonded ratio of the nanometer-thick films on COC.

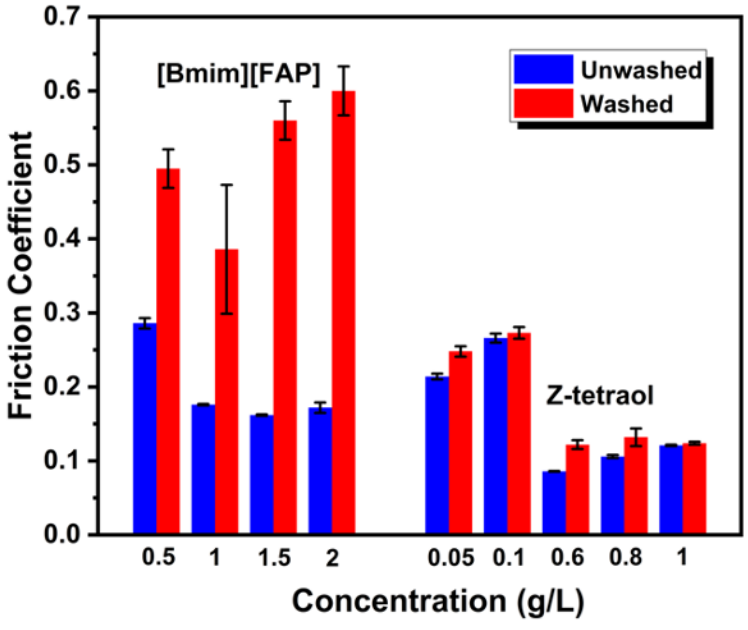

Figure 26. COF of the nanometer-thick films before and after Vertrel washing.

4.4 Conclusions

In conclusion, we have highlighted the potential of nanometer-thick fluorinated ILs as novel media lubricants in this paper. The TGA results indicated that [Bmim][FAP] has higher thermal stability than Z-tetraol, which is mainly attributed to the electrostatic interaction of the ion pairs in the IL. This characteristic is critical to the application of the IL as a HAMR lubricant. More importantly, the ML thickness of [Bmim][FAP] on COC is only ~50% of that of Z-tetraol based on the surface roughness results by AFM, which provides the opportunity to scale down the thickness of the nanometer-thick films and thus increase the areal density. We concluded that the intrinsically small molecular size of the IL induces a lower ML thickness. The lower ML thickness of [Bmim][FAP] over Z-tetraol was further supported by the friction results of the nanometer-thick films confined on COC. The COF of the nanometer-thick [Bmim][FAP], however, is slightly higher than that of the PFPE, which indicates the direction for synthesizing the next-generation ILs with more fluorinated components and hydroxyl groups to reduce the surface tension and enhance the bonding to solid substrates.

5.0 Highly Fluorinated Ionic Liquid Films as Nanometer-Thick Media Lubricants for Hard Disk Drives

The material in this chapter is based upon the published work *ACS Appl. Nano Mater*. 2020, 3, 9, 8803–8809.[14]

5.1 Introduction

The operation of hard disc drives (HDDs) requires the use of nanometer-thick lubricants on magnetic media to enhance the lifetime by reducing the friction and wear at the head-media inierface.[33, 34] The lubricants should have high thermal stability and low volatility to ensure the durability, low film thickness to ensure a high areal density for recording media, and good tribological properties such as low surface tension and the capability of load-carrying and self-healing.[37] Unfortunately, the state-of-the-art boundary lubricant, perfluoropolyether (PFPE), has inadequate thermal stability, and its minimum film thickness is limited by the relatively large polymeric molecular structure.[11, 13, 38] Ionic liquids (ILs) are promising to be the next-generation boundary lubricants for HDDs because of their on-demand structure design of cations and anions, and optimum physicochemical properties, i.e., small molecular sizes, high thermal stability, and negligible volatility.[3, 12, 35] Besides, ILs with aromatic cations can form parallel packing structure of cations and anions on charged solid surfaces, e.g., silicon wafer, mica, and gold, and on amorphous carbon surfaces with sp^2 hybridization, e.g., carbon overcoat (COC), graphene, and graphite, which is beneficial for lubrication.[3, 27, 44, 46, 78, 127, 134]

There have been a handful of previous reports on the application of commercially available ILs as boundary lubricants for microdevices and nanodevices to date. Palacio et al. studied [Bmim][PF_6] and [Bmim][$OctSO_4$] as ultrathin lubricants for potential applications in NEMS/MEMS, HDDs, and digital micromirror devices (DMD) because of the excellent electrical and thermal conductivity of the ILs.[35, 39-41] Zhu et al. studied nanometer-thick ILs with 3-butyl-1-methylimidazolium ([Bmim]) cations and concluded that high hydrophobicity of ILs leads to lower friction.[137] Hatsuda et al. investigated the lubrication of magnetic media using thin DBU- and TBD-based protic ILs.[42, 43] Gong et al. demonstrated the potential of nanometer-thick ILs with fluorinated tris(pentafluoroethyl)trifluorophosphate ([FAP]) anions for lubrication in heat-assisted magnetic recording (HAMR).[11] Lertola et al. reported that ILs with lower surface tension have better tribological properties when confined to charged solid surfaces.[15] Recently we have found that [Bmim][FAP] is promising to be the next-generation media lubricant due to its more robust thermal stability and significantly lower ML thickness than PFPE lubricants.[13] Nevertheless, the primary concern for the application of commercially available ILs as media lubricants is their higher surface tension than PFPEs, e.g., >30 mN/m v.s. 24 mN/m. The undesired higher surface tension typically results in stronger adhesion and more contamination during operation. This drawback significantly limits the tribological performance of ILs as nanometer-thick media lubricants. Addition of fluorinated components in ILs could reduce the IL surface tensions. Some progress has been made in recent years on the development of fluorinated ILs, e. g., the computational studies on the triphilic mixtures of fluorinated aprotic and protic ILs.[138-140]

In the current paper, we have successfully synthesized a novel highly fluorinated IL (FIL). The surface tension of FIL is comparable to PFPE and significantly lower than the commercially available IL lubricants, which is a key step forward in applying ILs as media lubricants. The

thermogravimetric analysis (TGA) showed that FIL has higher thermal stability than PFPE Ztetraol. The atomic force microscopy (AFM) indicated that the ML thickness of FIL is only ~50% of that of Ztetraol, which can be attributed to the intrinsically small molecular size of FIL. Compared to the commercially available ILs, the friction of the nanometer-thick FIL lubricant on COC was also lower. Our results suggest that the synthesized FIL is promising as the next-generation lubricant in HDDs.

5.2 Experimental Section

5.2.1 Chemicals and Materials

The reactants for synthesizing FIL include 1-iodo-1H,1H,2H,2H-perfluorohexane (99%) from TCI America, 1-methylimidazole (99%) from Sigma-Aldrich, and lithium bis(trifluoromethane)sulfonimidate (99%) from Fisher Scientific. All the other chemicals, i.e., toluene, diethyl ether, ethyl acetate, and silver nitrate, were purchased from Sigma-Aldrich. The above-mentioned chemicals were used as received. Ztetraol (Figure 17) is the PFPE primarily studied, as it is one of the most commonly used PFPEs.[11] It was purchased from Solvay Solexic Inc. and used as received. The polymer has a radius of gyration (R_g) of 1.5 nm,[131] its characteristic size, and has a fluorinated backbone and four hydroxyl end groups. The vapor pressure of Ztetraol is as low as 5.33×10^{-6} Pa at 20 °C.[132] Both FIL and Ztetraol can be readily dissolved in the solvent 2,3-dihydrodecafluoropentane (Vertrel XF), which was obtained from Miller-Stephenson Chemical Company and used as received. The solid substrate utilized was COC, the state-of-the-art substrate for the media lubricant in the HDD industry.[141, 142] The surface of COC is composed

of 3 nm thick amorphous carbon with sp^2 and sp^3 hybridization. The carbon film was deposited on a CrTa-metalized glass substrate (glass COC) or a NiP/aluminum substrate (aluminum COC) through a PECVD process that is widely used in the HDD industry. The top few angstroms of the carbon film was enriched with nitrogen to promote lubricant bonding. Aluminum COC was used to measure film thicknesses via ellipsometry, and glass COC was used for the rest of the characterizations.

5.2.2 Synthesis of FIL

Scheme 1 illustrates the two-step synthetic path of FIL, i.e., 1-1H,1H,2H,2H-perfluorohexyl-3-methylimidazolium bis(trifluoromethylsulfonyl)imide, which contains an imidazolium cation with a highly fluorinated alkyl chain and a fluorinated anion. The first step of the synthesis undergoes the S_N2 reaction, where the highly fluorinated alkyl chain is added in the imidazolium cation. Initially, 35 mL toluene was used to dissolve 21.8 mmol 1-iodo-1H,1H,2H,2H-perfluorohexane. 24.0 mmol 1-methylimidazole was added in the solution, and the reaction is stirred and refluxed at 110 ℃ under N_2 purging for 15 hr. After cooling to the room temperature, toluene was decanted, and the remaining wax was stirred in 200 mL diethyl ether. Subsequently, the mixture was washed with 150 mL diethyl ether for three times and dried under vacuum overnight. The second step of the synthesis undergoes the metathesis reaction, where the fluorinated anion bis(trifluoromethane)sulfonimidate ($[NTf_2]^-$) replaces the iodide anion. The product from the S_N2 reaction was dissolved in 80 mL DI water at 65 ℃. 21.8 mmol lithium bis(trifluoromethane)sulfonimidate was then added, and the reaction was stirred at 65 ℃ for 3 hours. After the metathesis reaction, the product was dissolved in 200 mL ethyl acetate and washed with 100 mL DI water for four times until pH 6-7. (The test on I^- with $AgNO_3$ in the separated

water phase was negative.) Finally, the final product was extracted from the solvent by rotary evaporation and dried under vacuum at 75 ℃ overnight. The obtained FIL, 1-1H,1H,2H,2H-perfluorohexyl-3-methylimidazolium bis(trifluoromethylsulfonyl)imide, was a viscous liquid in light yellow color.

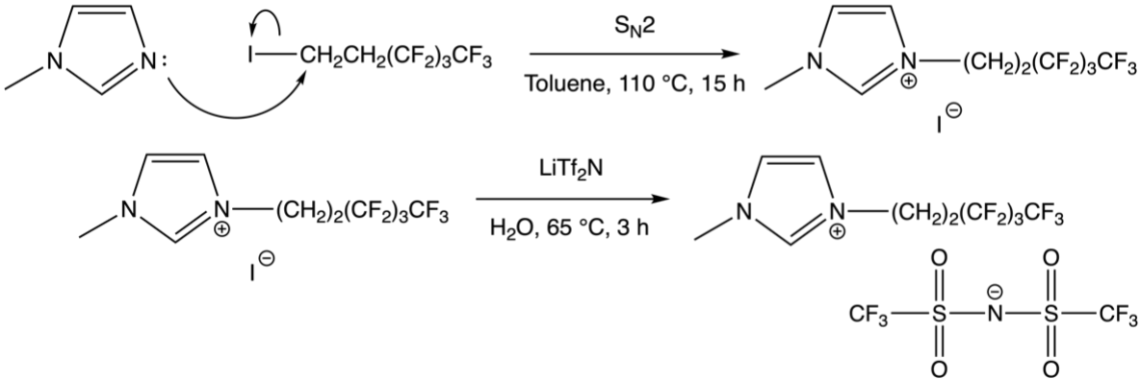

Scheme 1. Synthesis of FIL.

5.2.3 Nanofilm Fabrication and Thickness Measurement

The lubricants were applied on the COC substrates in nanometer-thick films by dipcoating, which is commonly used in the HDD industry.[88, 89] Dilute solutions of different concentrations of the lubricants in Vertrel XF were prepared. To apply the thin film, a substrate was lowered into and subsequently removed from a solution vertically at a speed of 60 mm/min with a KSV Instrument dipcoater. The thickness of this lubricant layer directly trends with the concentration of the solution as we previously reported.[11] To measure the thicknesses of the nanofilms, ellipsometry was conducted using a J. A. Woollam alpha-SE Spectroscopic Ellipsometer with a wavelength range of 380-900 nm, an incident angle of 70°, and a beam diameter of ~2 mm. The

Cauchy dispersion model was used to determine the thickness of the lubricant layer.[11] The nanofilm thicknesses measured by ellipsometry are the average thicknesses within the areas covered by the beams.

5.2.4 Characterization of FIL

The chemical structure and the purity of the synthesized FIL were determined by ^{1}H NMR spectroscopy using a Bruker Avance III 500 MHz Spectrometer with a BBF/1H broadband observe probe. The 2.50 ppm chemical shift of the trace impurity of the NMR solvent, i.e., DMSO-d_6, was referenced.[143] In addition, the chemical compositions of FIL were characterized by Energy-Dispersive X-ray Spectroscopy (EDS) with a 15 kV accelerating voltage.

To test the thermal stability of FIL, TGA was performed with a SEIKO-220 TG/DTA system. The purity of the synthesized FIL was further examined by TGA. For each test, a sample of lubricant weighing approximately 25 mg was placed in an aluminum pan and heated from RT to 610 °C at a heating rate of 10 °C/min under air purging.

The surface tension was measured by the pendant drop method using a VCA Optima Contact Angle system. In the measurement, the liquids were dispensed through the needles to form pendant drops, and the droplet images were captured by a charge-coupled device (CCD) camera. The vendor-supplied software can calculate the surface tension values through the drop shapes and the density values based on the Young-Laplace equation.

5.2.5 Assessment of Lubrication Performance

The surface topography and roughness of the nanometer-thick lubricants on COC were inspected with AFM using a Veeco Dimension V Scanning Probe microscope. Scans were conducted at tapping mode with an image acquisition of 256 by 256 pixels and a vertical resolution of 0.1 nm. The AFM probe was MikroMasch NSC14/AL BS (resonance frequency, 160 kHZ; force constant, 5.0 N/m; tip radius, 8 nm) with an aluminum tip on an n-type silicon cantilever. The lateral resolution of the scans was 39 nm as the scan area was 10 μm by 10 μm. AFM scan is not able to capture any lateral textures lower than the pixel size. The scan rate for all image acquisitions was 0.3 Hz.

The water contact angle (WCA) and hexadecane contact angle (HCA) of nanometer-thick FIL on COC were measured based on the sessile drop method also using the VCA Optima Contact Angle system. 1.5 μL drops of testing liquids were dispensed on the surfaces through a syringe automatically, and the drop shapes were captured by a CCD camera and analyzed. The CA on each sample was averaged by measuring on at least three locations.

Nanotribology testing was conducted using a CSM Instruments Nano Tribometer that was placed on a Kinetic Systems Vibration Control Platform. The coefficient of friction (COF) was measured with a dual beam cantilever and high-resolution capacitive sensors. A stainless steel ball with 2 mm in diameter was used as the counterface. The normal load, the maximum linear speed, and the amplitude were set as 10 mN, 0.20 cm/s, and 2.00 mm, respectively, and 50 cycles were performed for each trial. Each sample was tested for at least three trails. The counterface was cleaned with isopropanol between trials. The tests were performed at 5-50% RH and 20-22°C.

The bonded ratio was measured to determine how strong the lubricants bond to the substrate surface, as reported previously.[13, 89] This was done by measuring the thickness of the lubricant layer after dipcoating by ellipsometry, washing the surface of the samples by dipping them into and subsequently removed from pure Vertel XF at 60 mm/min, and measuring the thickness of the remaining lubricant layer by ellipsometry.

5.3 Results and Discussion

5.3.1 Characterization of FIL

^{1}H NMR analysis was conducted on the synthesized 1-1H,1H,2H,2H-perfluorohexyl-3-methylimidazolium bis(trifluoromethylsulfonyl)imide, as shown in Figure 27. The peak shift, the peak integral, and the multiplet splitting for all the assigned peaks demonstrate the successful synthesis of FIL. It is worth noting that the peak at 2.5 ppm is from the trace impurities of the solvent DMSO-d_6, and the peak at 3.3 ppm is from absorbed water in the solvent.[143] The chemical composition results characterized by EDS elemental analysis, which are listed in Table 1, further support the conlusion of successful synthesis of FIL. Additionally, as shown by the TGA results in Figure 28, only one step of weight loss can be detected for the synthesized FIL, demonstrating the high purity of the product. The TGA results also indicate that FIL has significantly better performance than PFPE Ztetraol in terms of thermal stability because of the strong electrostatic interactions within FIL. The onset of the weight loss was higher than 350 °C for FIL, while the weight loss started at ~150 °C for Ztetraol. The 50% weight-loss of FIL occured at ~450 °C, which

was also more than 100 °C higher than Ztetraol. The excellent thermal stability of FIL is ideal for its application in lubrication due to the rising temperature during tribology contact.

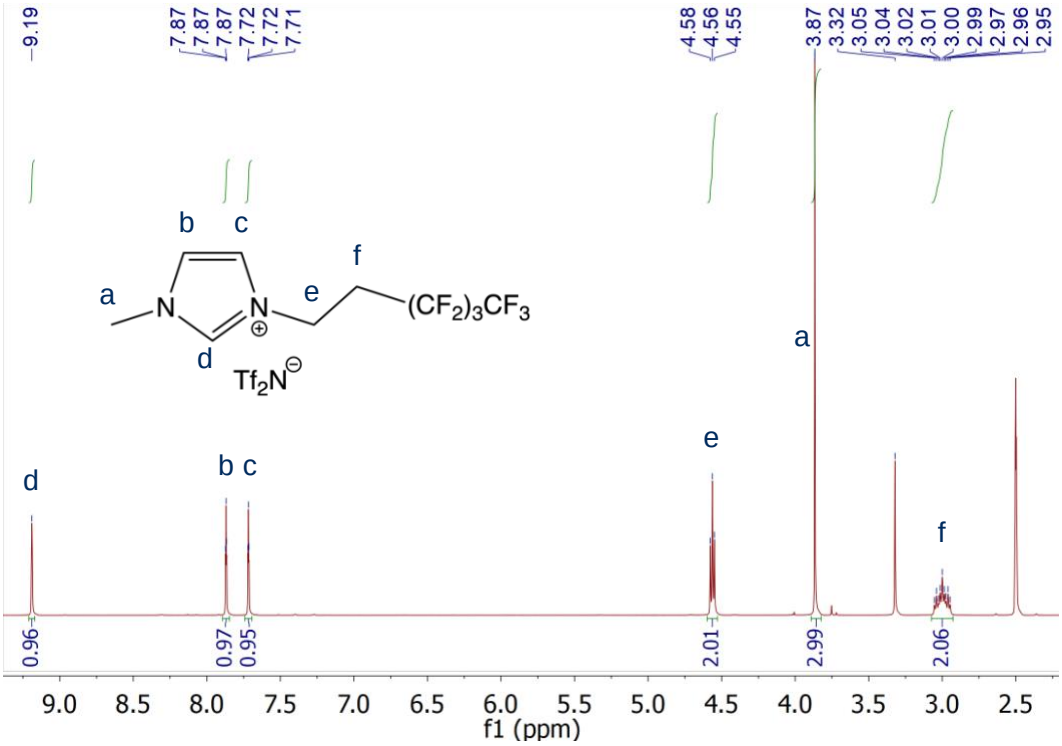

Figure 27. ^{1}H NMR spectrum of 1-1H,1H,2H,2H-perfluorohexyl-3-methylimidazolium bis(trifluoromethylsulfonyl)imide. The peak assignments are labeled.

Table 5. Chemical compositions of FIL

	C	F	O	S	N
Theoretical	23.7%	46.8%	10.5%	10.5%	6.9%
Experimental	25.7%	46.5%	10.7%	9.3%	6.2%

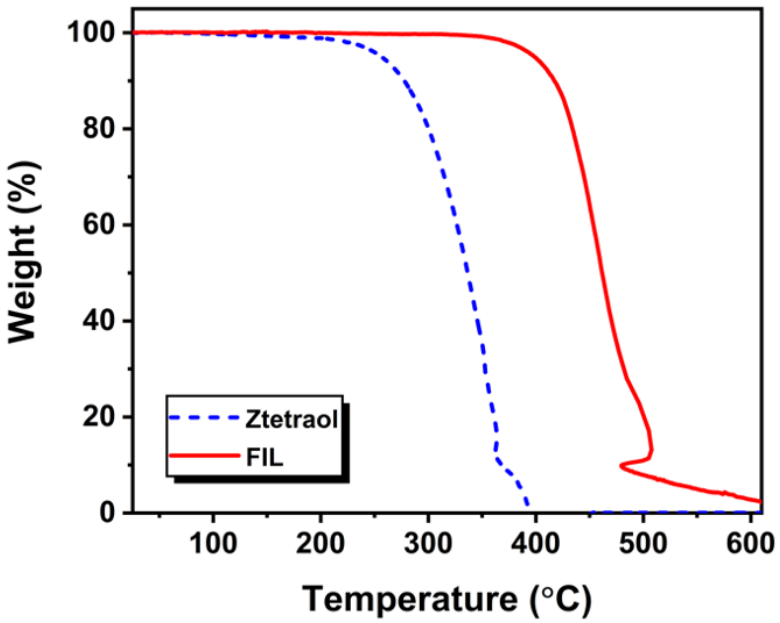

Figure 28. TGA results of bulk Ztetraol and FIL.

5.3.2 Reduced Surface Tension of FIL

For the molecular design of the next-generation FIL lubricant, the substitution of multiple CF_x groups in the IL cation is expected to induce a low surface tension close to PFPEs. The surface tension of the synthesized FIL was measured by the pendant drop method and compared with the commercially available [Hmim][NTf_2], which has the same [NTf_2] anion and the same length of alkyl chain in the imidazolium cation with FIL, and two PFPEs, i.e., Zdol and Ztetraol (Figure 17). As shown in Table 6, the surface tension of FIL is 24.5 mN/m, which is significantly lower that of [Hmim][NTf_2] (i.e., 31.2 mN/m.) Indeed, it is comparable to the surface tension of PFPE Zdol (24 mN/m), yet slightly higher than that of Ztetraol (22.4 mN/m).

Table 6. Surface tension ($\boldsymbol{\gamma}$) of FIL, [Hmim][NTf_2], Zdol, and Ztetraol at RT

	FIL	[Hmim][NTf_2]	Zdol[144]	Ztetraol[135]
γ (mN/m)	24.5 ± 0.04	31.2 ± 0.38	24.0	22.4

Figure 4 presents the WCA and HCA results on the FIL-coated COC with varying FIL thicknesses. The WCA remains constant as the film thickness increases, which can be explained by a previous hypothesis that the tiny water molecules always travel through the relatively big intermolecular pores in the FIL nanofilms instantly and rest on the composite of FIL nanofilms and COC surface.[145] During HCA measurements, the hexadecane molecules, which are insoluble to FIL, can initially go through the intermolecular pores when the nanofilm is at the thickness of 0.72 nm. The intermolecular pores become smaller as the nanofilms grow thicker. When the nanofilm is thicker than 1.10 nm, the hexadecane molecules, which are much bigger than the water molecules, cannot go through the pores anymore.[145] Consequently, hexadecane rests on the surface of the FIL nanofilms instead, and the HCA increases with the FIL thickness. The interfacial tension between the thicker lubricant film and hexadecane is calculated as ~10.4 mN/m based on the force balance at the three-phase interface $\gamma_L = \gamma_{LH} + \gamma_H \cos\theta_H$, where γ_L is the surface tension of the FIL lubricant (24.5 mN/m), γ_H is the surface tension of hexadecane, and θ_H is the HCA.[146] Detailed growth model of the FIL nanofilms on COC is discussed later. The hypothesis here certainly requires further investigations. However, the CA results reveal that the FIL-coated COC exhibits simultaneous hydrophilicity/oleophobicity.

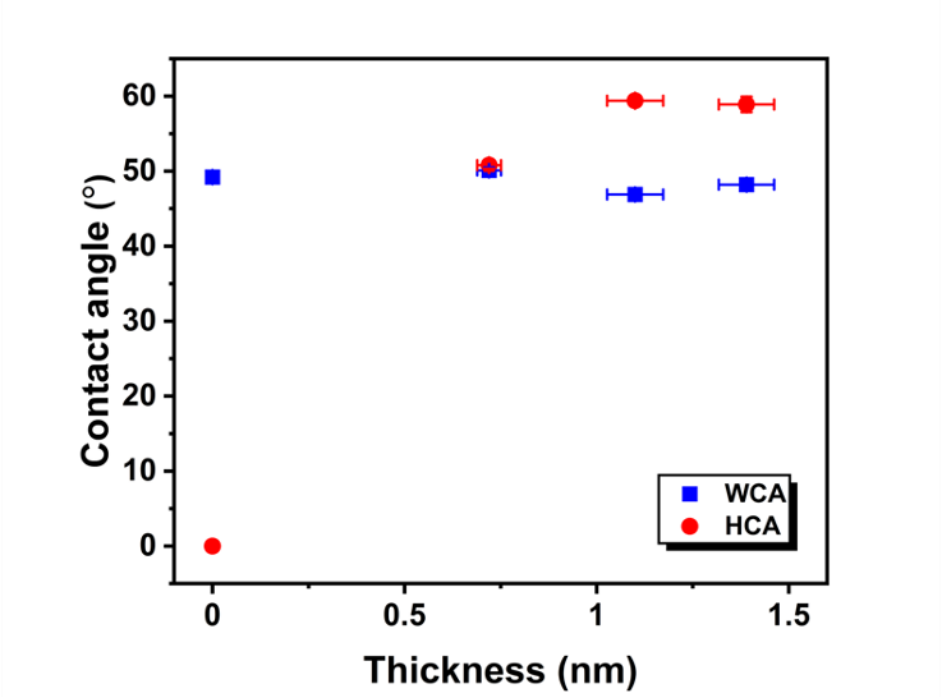

Figure 29. CA results on the nanometer-thick FIL films.

Compared to the commercially available ILs, the significantly lower surface tension of FIL is ideal for reducing the adhesion between the sliding component and the substrate and consequently inducing more robust tribological performance. Moreover, it is difficult for airborne contaminants to attach to the FIL-covered surface, which improves their efficiency and reliability for long-term operations.[147]

5.3.3 Nanometer-Thick FIL as Media Lubricant

In a hard disk drive (HDD), the spacing between the flying head and the media surface is less than 10 nm to ensure a high areal density.[11, 116] As a result, the media lubricants need to be as thin as possible.[13] The monolayer (ML) thickness of the lubricant molecule governs the lowest possible thickness of the fully covered nanofilm.[119, 121] The method of determining the ML

thickness based on the variation of the root-mean-square (RMS) surface roughness with the nanofilm thickness has been established in our previous report.[13] In short, the ML thickness can be estimated by the change in RMS values obtained from AFM scans. The nanofilm is smooth with low roughness when thinner than ML, while a significant increase in RMS and a change from wetting to dewetting occur when the film thickness exceeds the ML thickness. Accordingly, the ML thickness of the synthesized FIL on COC was analyzed by AFM first. The surface roughness of the bare COC and the state-of-the-art media lubricant, i.e., PFPE Ztetraol, were used as control. Figure 30 shows the surface roughness results in RMS at various thicknesses for the nanofilms on COC. The insets also show the AFM scan images of the nanometer-thick FIL at various thicknesses. 2D AFM images and their corresponding line profiles for all FIL nanofilms are also reported in Figure 31. The ML thickness for Ztetraol has been previously determined as ~1.6 nm,[13] which is also close to its 1.5 nm R_g.[131] For the Ztetraol films thinner than ML, the surfaces remained smooth as the hydroxyl end groups preferred to bond with COC, while a sharp increase in surface roughness was observed as the interaction among the noninteracting hydroxyl group dominated over the solid-liquid interaction.[38]

Based on the AFM surface roughness results, the ML thickness of the synthesized FIL lubricant is ~0.9 nm, which is only about half of the ML thickness of the Ztetraol lubricant. As shown in Figure 30, the FIL nanofilms are very smooth at the thinner regime (≤ 0.9 nm), and the RMS remains at low values (0.108 ± 0.0015 nm at the thickness of 0.72 nm and 0.099 ± 0.0007 nm at the thickness of 0.9 nm) comparable to the RMS of bare COC (0.114 ± 0.0010 nm). At this stage, the FIL nanofilm covers more COC surface areas as the film thickness from ellipsometry increases, until the film thickness reaches the ML thickness. A possible mechanism is that the π-π stacking interaction between the delocalized π^+ electrons from the FIL aromatic cations and the π

electrons from the sp^2 amorphous carbon on COC enables the FIL cations to form a layer of film on the COC surface, which induces the subsequent layering of the anions on the cation layer vertically.[46, 134] As the film does not uniformly cover the solid surface, hexadecane is in contact with the composite of the FIL nanofilm and the COC surface, so HCA is low at the thickness of 0.72 nm (Figure 29). It is noteworthy that AFM is not able to reveal the surface morphology smaller than the pixel size (39 nm) in the lateral directions, so a smooth surface is captured for the film thinner than ML. The film coverage on COC can be estimated by Cassie's law for heterogeneous surfaces, $\cos\theta_H = \sigma_1 \cos\theta_{H1} + \sigma_2 \cos\theta_{H2}$,[148] where θ_H is the overall HCA (50.8°), σ_1 is the bare COC area with the HCA of θ_{H1} (0°), σ_2 is the FIL nanofilm area with the HCA of θ_{H2} (~59°). The coverage of the 0.72 nm thick FIL nanofilm on COC is calculated as approximately 76% of the total surface area. However, when the nanofilm thickness exceeds ~0.9 nm, sharp increases in the surface roughness occurs, that is, RMS of 0.162 ± 0.0100 nm at the thickness of 1.1 nm. For the thicker FIL nanofilms, the cohesion within the FIL ions surpasses the π-π interaction between the FIL and the solid.[16] The FIL nanofilm starts to grow on top of the ML film, and dewetting occurs. As the FIL nanofilms completely cover the solid surface, hexadecane rests entirely on the surface of the nanofilms, so HCA remains high. As a result, we conclude that the ML thickness of the FIL lubricant is ~0.9 nm, which is the thickness of the first cation/anion layer. Moreover, assuming the FIL molecules are cubic,[92, 127] the dimension *a* of each FIL molecule can be calculated by $a = \sqrt[3]{\frac{M/N_A}{\rho}}$, where *M* is the molar mass (609.27 g/mol), ρ is the density (1.66 g/ml at RT), and N_A is the Avogadro constant. Accordingly, the dimension of the FIL molecule is estimated as 0.85 nm, which is comparable to the ~0.9 nm ML thickness determined from the AFM surface roughness results. Additionally, based on the van der Waals radii, the dimensions of the FIL cation and anion are estimated as 1.12 × 0.21 × 0.41 nm^3 and 0.72× 0.36 × 0.24 nm^3,

respectively (Figure 32). Compared to Ztetraol, the thinner ML thickness of FIL provides the lower minimum thickness of the nanometer-thick lubricants, which is expected to result in a higher areal density.

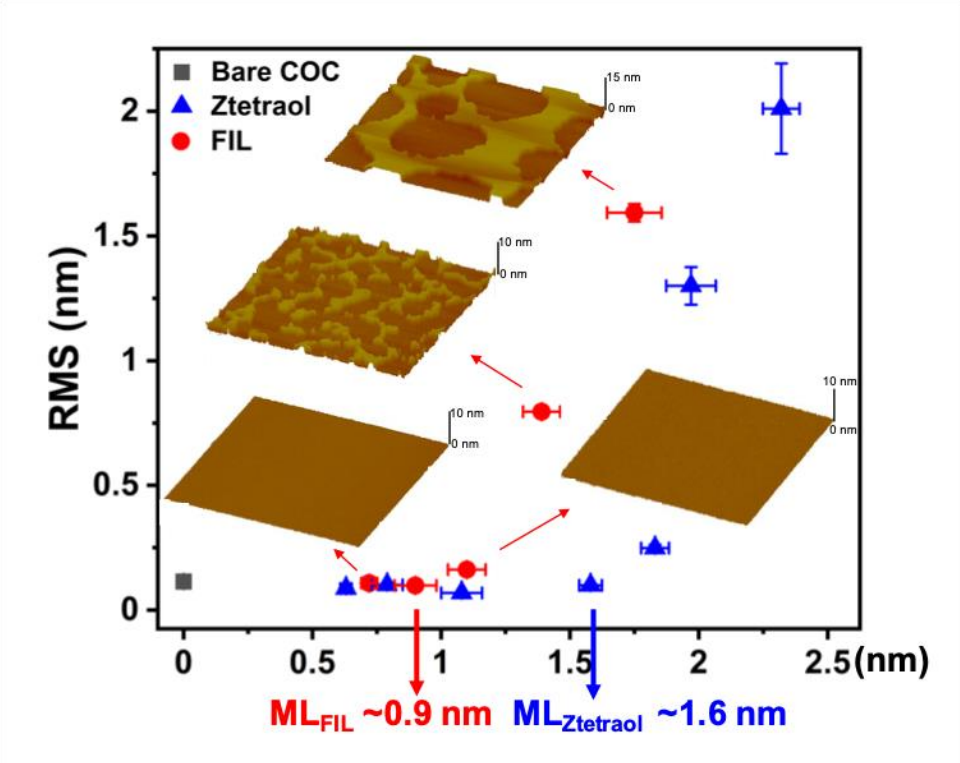

Figure 30. Surface roughness results of the nanometer-thick lubricants on COC. The insets are AFM images of the FIL nanofilms at various thicknesses (10 μm by 10 μm scan size).

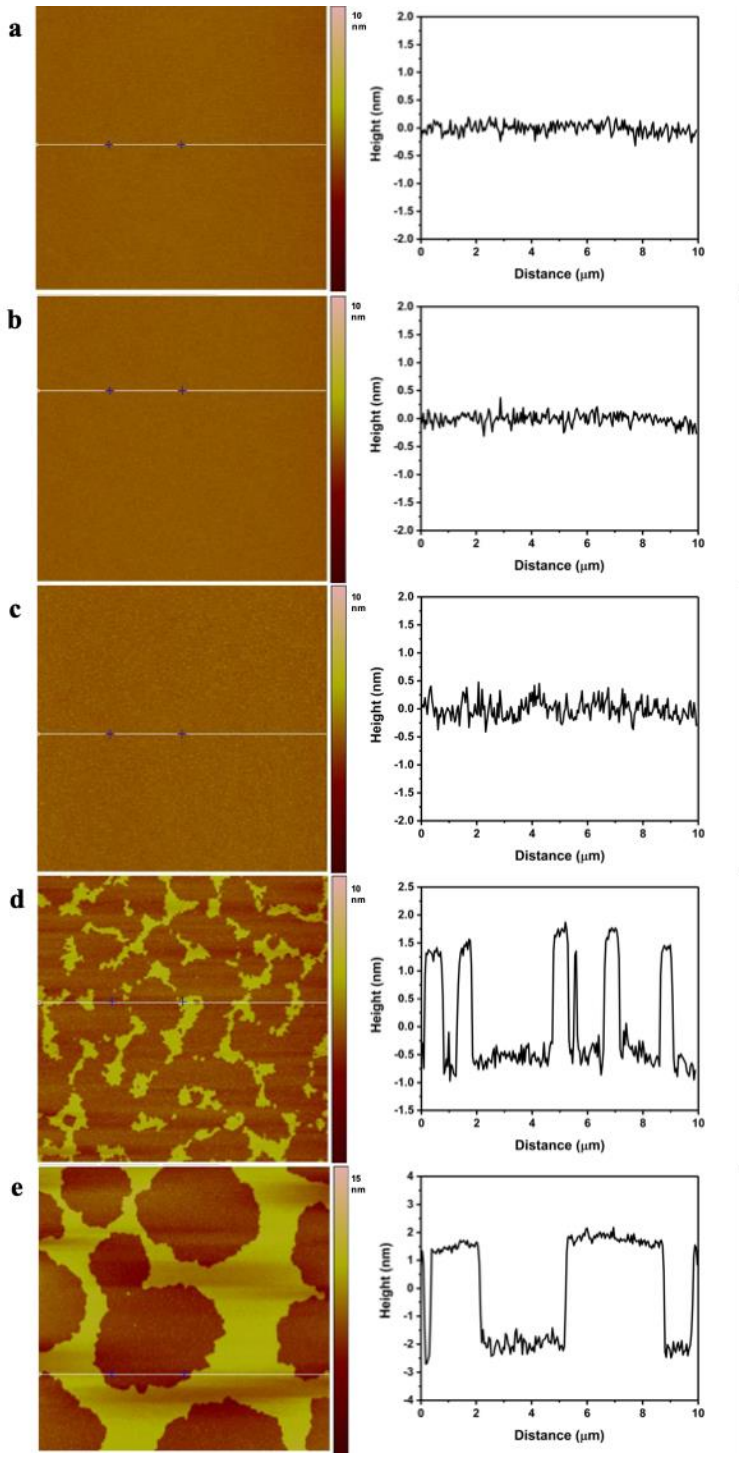

Figure 31. 2D AFM images and the line profiles of nanometer-thick FIL on COC at (a) 0.72 nm, (b) 0.9 nm, (c) 1.1 nm, (d) 1.39 nm, (e) 1.75 nm. The scan sizes are 10 μm by 10 μm.

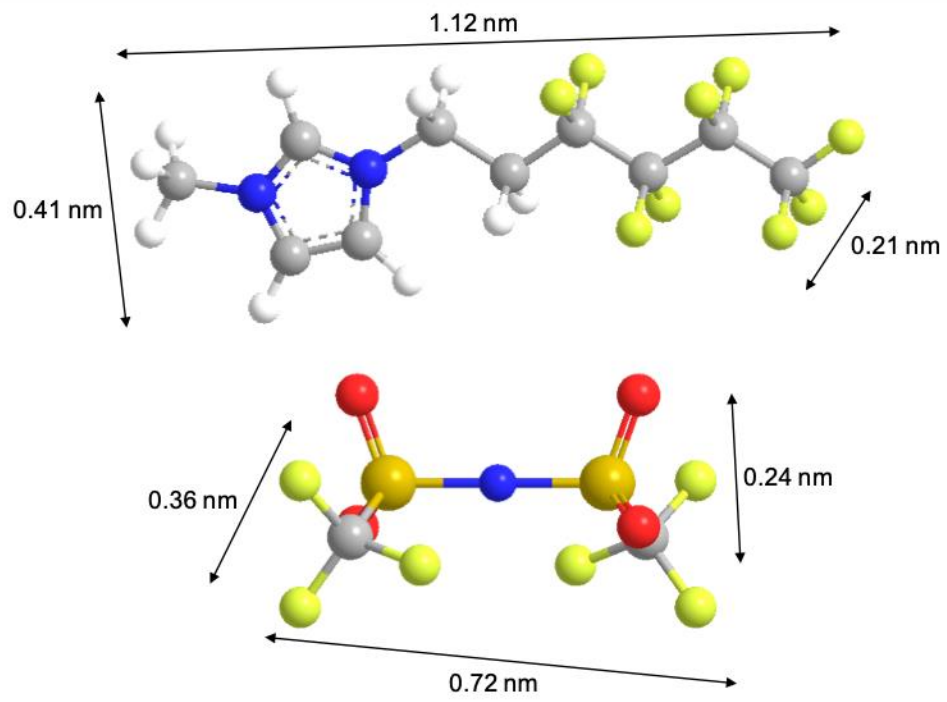

Figure 32. Estimated dimensions of the FIL cation and anion from van der Waals radii.

Nanotribology testing has been performed for the nanometer-thick lubricants at various thicknesses on COC, and the coefficient of friction (COF) results are shown in Figure 33. The COF results of the bare COC (i.e., 0.444 ± 0.024), Ztetraol, and [Bmim][NTf_2] were used as control. For the FIL nanofilms, the COF decreased from 0.276 ± 0.009 at the thickness of 0.72 nm to minimum values of 0.153 ± 0.001 and 0.150 ± 0.006 at the thickness of 1.39 nm and 1.75 nm, respectively. The high COF for the FIL nanofilm below ML could result from the insufficient coverage of the FIL lubricant on COC. In contrast, the COF of [Bmim][NTf_2] decreased from 0.320 ± 0.003 at the thickness of 0.65 nm to a minimum value of 0.167 ± 0.008 at the thickness of 2.10 nm, which is approximately 11% higher than the level-off COF of FIL. Unlike hydrodynamic lubrication, the lubrication using the molecular-level FIL films in microdevices is defined as boundary lubrication, where the chemical structure of the nanometer-thick lubricants is the most

critical factor to the adhesion and the friction.[33, 149, 150] The adhesion in nanotribology is governed by the van der Waals force, and the Hamaker constant (A_H) characterizes the intermolecular force.[33] Due to the presence of the highly fluorinated alkyl chain with low polarizability, the FIL boundary lubricant with low surface tension has a low A_H, and consequently results in a low adhesion and friction compared to the commercially available IL boundary lubricants.

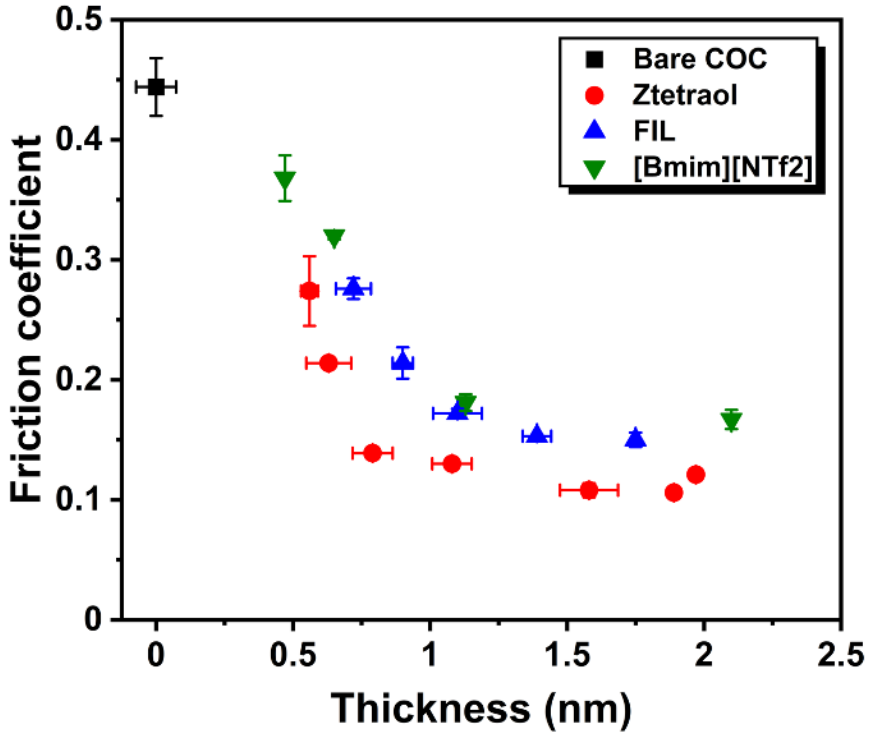

Figure 33. Friction results of the nanometer-thick lubricants on COC.

Despite the reduced COF compared to the commercially available IL, the FIL nanofilms still have slightly higher level-off friction than the Ztetraol nanofilms, as shown in Figure 33. To achieve low friction in boundary lubrication, it helps when a layer of lubricant molecules can bond to the COC surface to certain extent.[33, 149] The FIL nanofilms at various thicknesses on COC were

washed with Vertrel XF to study the bonding between the lubricants and COC. The thicknesses of the FIL nanofilms before and after washing are reported in Figure 34. For all FIL nanofilms with different initial thicknesses, most of the lubricants transferred from COC into the solvent, indicating a dominating fraction of mobile lubricants over bonded lubricants. During tribology testing, the majority of the FIL boundary lubricants were displaced from the surface asperities of COC, which led to an increase in the undesired solid/solid contact.[13] As FIL has no functional end-groups in its molecular structure, the nanofilms stay on the COC surface only by relatively weak van der Waals interactions. For Ztetraol, however, the molecules are bonded to the polar sites in COC by stronger hydrogen bonding.[13, 89] While the mobile molecules are displaced as the testing head moves, the bonded layer of molecules still covers the COC surface. Additionally, while a highly fluorinated alkyl chain has been added in the cation, the surface tension of FIL is still slightly higher than Ztetraol (see Table 6). To achieve more robust tribological performance, the molecular design of the next-generation FIL lubricant should contain functional hydroxyl end-groups in the FIL to promote the bonding to the solid surface and more fluorinated moiety to further lower the surface tension.

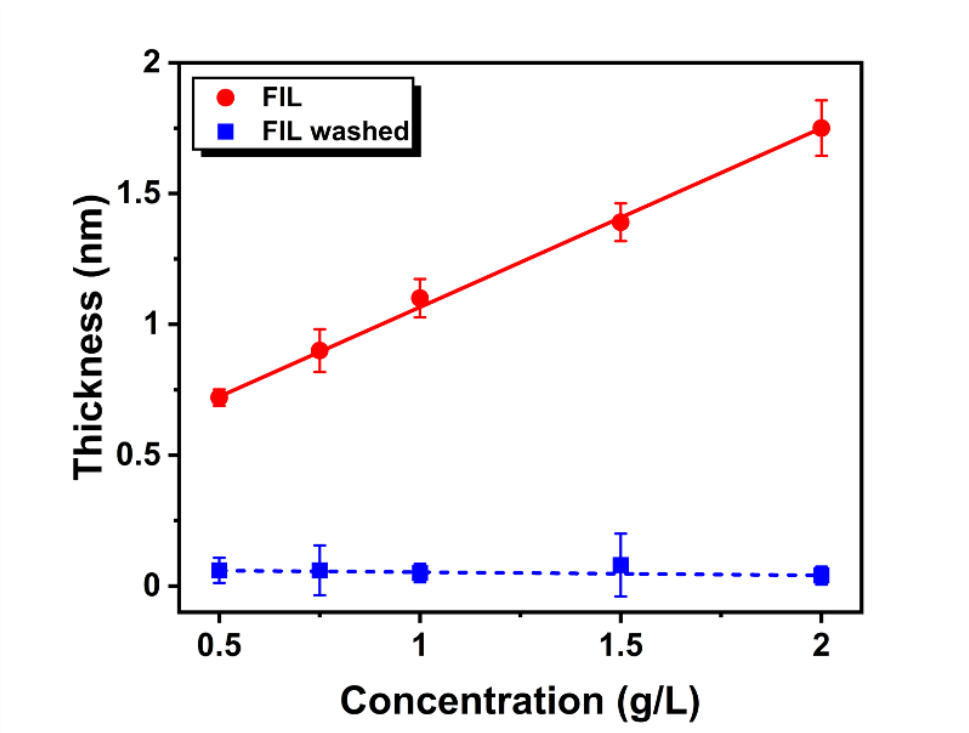

Figure 34. Thicknesses of the nanometer-thick FIL lubricants on COC before and after Vertrel XF washing.

5.4 Conclusions

In this paper, we report our successful synthesis of a novel FIL lubricant with a highly fluorinated alkyl chain in the cation. The molecular structure and the purity of the synthesized FIL were confirmed with ^{1}H NMR and TGA. The TGA results also suggested that FIL has higher thermal stability than PFPEs. Compared to the commercially available IL lubricant, a significant decrease in the surface tension of FIL was achieved due to the highly fluorinated structure of the FIL molecule. AFM surface roughness results revealed that the ML of FIL is much thinner than

Ztetraol, which is expected to induce a lower minimum thickness of the nanometer-thick lubricants and hence a potentially higher areal density in HDDs. Moreover, the friction results demonstrate the COF of the nanometer-thick FIL lubricant on COC is lower than the commercially available IL because of the intrinsically lower surface tension of FIL. Our results indicate that FIL is promising as the next-generation boundary lubricant in HDDs. As the friction of the current FIL lubricant is comparable to yet still slightly higher than the PFPE Ztetraol lubricant, the future design of FIL lubricant needs to have enhanced bonding to the solid substrate and an even lower surface tension.

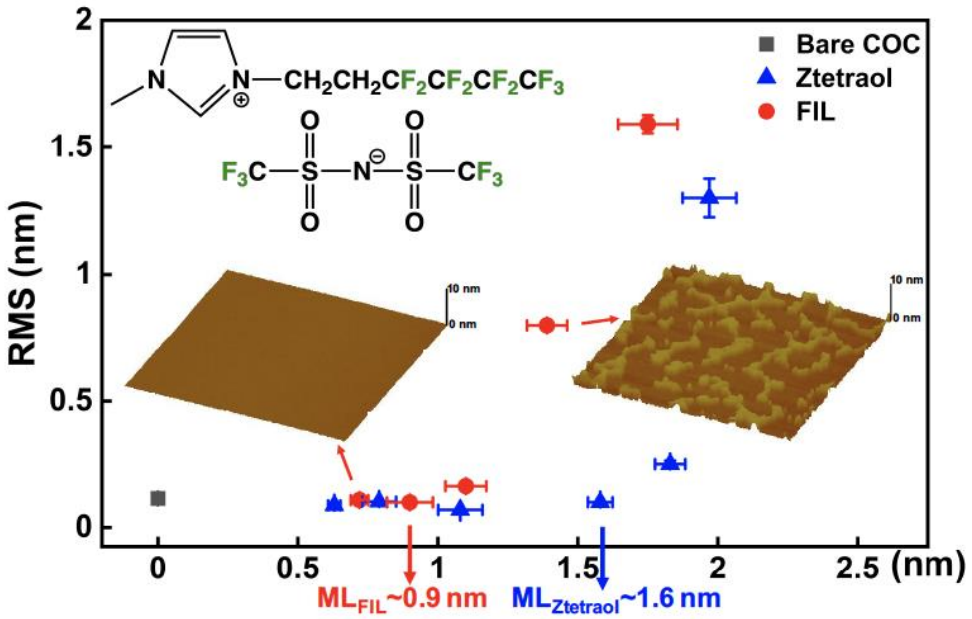

Figure 35. TOC figure.

6.0 Novel Highly Fluorinated Ionic Liquid with Functional Endgroups as Nanometer-Thick Media Lubricants for Hard Disk Drives

The material in this chapter is based upon a manuscript for submission to *Advanced Materials* or *Nature Materials*.

6.1 Introduction

Physical contact between adjacent solid surfaces has been a huge concern when operating nanoscale devices with contacting components during operation, e. g., hard disc drives (HDD) and nano- and micro-electromechanical systems (NEMS/MEMS).[33-35] The use of nanometer-thick boundary lubricants on solid surfaces to reduce friction and wear is critical to the efficiency and reliability of these devices during operations. Ideally, the lubricants should have excellent tribological properties, i.e., low surface tension, and load-carrying and self-healing capabilities.[37] The lubricants should also have high thermal stability due to the heating from tribology contacts and the increasing need for heated-assisted magnetic recording (HAMR).[11] Besides, a lower thickness of the lubricant film is desired to achieve higher areal density for HDD. The minimum thicknesses of the lubricant films are determined by the monolayer (ML) thicknesses of the lubricant molecules. Unfortunately, the state-of-the-art lubricant, perfluoropolyether (PFPE), only has limited thermal stability, and its ML is relatively thick due to the sizable polymeric structure.[11, 13, 38] Ionic liquids (ILs) are promising candidates for the next-generation media lubricants for HDD due to their promising physical properties and relatively low cost. ILs consist of organic cations

and anions, and they are viscous liquids at RT due to their wide liquidous range. Many ILs have higher thermal stability and lower volatility than PFPEs.[1-3, 12] ILs with low surface tensions have good tribological performances on solid surfaces.[15] ILs also have been found to form layering structures that are ideal for lubrication when confined to solid surfaces, e.g., silica, mica, Au(111), and amorphous carbon surfaces, e.g., carbon overcoat (COC), graphite.[3, 27, 44, 46, 78, 127, 134] Besides, the much smaller molecular sizes of ILs than PFPEs also provide the opportunity to reduce the lubricant thicknesses.

In our earlier work, the commercially-available [Bmim][FAP] has been demonstrated to have much lower ML thickness, when confined to COC, than the state-of-the-art PFPE lubricant from the AFM surface roughness results.[13] The thin ML makes the IL promising to be the next-generation media lubricant, but its higher surface tension than PFPEs limits its lubrication performance due to the strong adhesion and contamination during operation. To address the concern, a novel highly fluorinated IL (FIL) that contains a highly fluorinated alkyl chain in the cation was synthesized.[14] The surface tension of FIL is significantly lower than commercially-available ILs and is comparable to PFPEs. FIL also has excellent thermal stability and low ML thickness on COC. The successful development of the FIL lubricant is a major leap forward in applying ILs as the next-generation media lubricants in HDDs. However, FIL has been found to have an almost zero bonded ratio on COC because it has no functional endgroups in the molecule. The weak bonding of FIL to the COC surface could cause unwanted direct counterface contact. To further improve the tribological performances of IL lubricants, it is essential to develop fluorinated ILs with functional endgroups.

Here, we report our successful synthesis of two novel fluorinated ILs with functional endgroups. The first IL, FIL-OH, contains a hydroxyl endgroup and a highly fluorinated alkyl

chain in the cation. FIL-OH has enhanced bonding to the COC surface, but the coverage of the fluorinated segments is limited. The second IL, HFIL-OH, contains the same hydroxyl endgroup and fluorinated alkyl chain in the cation as FIL-OH and a more fluorinated anion. The surface tension of the HFIL-OH lubricant is even lower than the state-of-the-art PFPE lubricants. The surface energy of the HFIL-OH coated surface is significantly reduced due to the addition of the highly fluorinated anion, and the bonding between HFIL-OH and COC is enhanced due to the addition of the hydroxyl group in the cation.

6.2 Experimental Section

6.2.1 Chemicals and Materials

The reactants for synthesizing FIL-OH and HFIL-OH were 1-iodo-1H,1H,2H,2H-perfluorohexane (99%, TCI America), 1-(2-hydroxyethyl)imidazole (97%, Sigma-Aldrich), lithium bis(trifluoromethane)sulfonimidate (99%, Fisher Scientific), and lithium Bis(nonafluorobutanesulfonyl)imide (95%, TCI America). All the solvents were purchased from Fisher Scientific and Sigma-Aldrich and used as received. Ztetraol was the PFPE primarily used as the reference lubricant, which is one of the most commonly used PFPEs,[11] and was acquired from Seagate Technology LLC and used as received. Ztetraol has a fluorinated backbone and four hydroxyl end groups, and its characteristic size, radius of gyration (R_g), is radius of gyration (R_g) radius of gyration (R_g), is 1.5 nm.[131] Its vapor pressure is 5.33×10^{-6} Pa at 20 °C.[132] FIL-OH, HFIL-OH, and Ztetraol can be easily dissolved in the solvent, 2,3-dihydrodecafluoropentane (Vertrel XF, Miller-Stephenson Chemical Company). The solid substrate tested was COC, which

is commonly used in the HDD industry.[141, 142] The surface of COC is composed of 3 nm thick amorphous carbon with sp^2 and sp^3 hybridization. The carbon film was deposited on a CrTa-metalized glass substrate (glass COC) or a NiP/aluminum substrate (aluminum COC) through a PECVD process that is widely used in the HDD industry. The top few angstroms of the carbon film was enriched with nitrogen to promote lubricant bonding. Aluminum COC was used to ellipsometry tests, and glass COC was used for lubrication characterizations.

6.2.2 Characterization of IL Products

The chemical structures of the synthesized ILs were characterized by ^{1}H NMR spectroscopy using a Bruker Avance III 500 MHz Spectrometer with a BBF/1H broadband observe probe. The 2.50 ppm chemical shift of the trace impurity of the DMSO-d_6 solvent was used as reference.[143]

TGA was performed by a SEIKO-220 TG/DTA system to determine test the thermal stability and further examine the purity of the synthesized ILs. A sample at ~20-25 mg was placed in an aluminum pan and heated under air purging from RT to 600 °C at a heating rate of 10 °C/min.

Pendant drop method was used to measure the surface tensions of the IL products with a VCA Optima contact angle machine at RT. The liquids were dispensed through the needles to form pendant drops, and the images of the droplet right before falling off were captured by a charge-coupled device (CCD) camera. The vendor-supplied software calculated the surface tension values from the drop shapes and the bulk densities based on the Young-Laplace equation.

6.2.3 Dipcaoting and Ellipsometry

The lubricant nanofilms were applied on the COC surfaces by dipcoating based on our previously established method.[13, 14, 88, 89] The IL products can be readily dissolved in Vertrel XF to prepare IL solutions at a range of concentrations. The COC substrate was vertically submerged into and subsequently pulled out from the solutions at a speed of 1 mm/second using a KSV Instrument dipcoater. The thickness of this lubricant films is directly controlled by changing the solution concentration.[11, 13, 14]

Thicknesses of the fabricated nanofilms were measured using a J. A. Woollam alpha-SE Spectroscopic Ellipsometer at an incident angle of 70° and a beam diameter of ~2 mm. B-spline model was used to determine the optical constants of the COC surface before dipcoating. After dipcoating, Cauchy dispersion model was used to measure the thickness of the IL nanofilms.[11] The measured thicknesses are the average thicknesses within the beam spot.

6.2.4 Assessment of Nanometer-Thick Lubricants

The surface topography of the nanometer-thick lubricants on COC was evaluated by AFM using a Veeco Dimension V Scanning Probe microscope. The AFM probe was MikroMasch NSC14/AL BS with a resonance frequency of 160 kHZ, a force constant of 5.0 N/m, and a 8 nm aluminum tip. The scans were conducted at tapping mode with an image acquisition of 256 by 256 pixels. The lateral resolution of the scans was 39 nm as the scan area was 10 μm by 10 μm, and the vertical resolution was 0.1 nm.

The water contact angle (WCA) and hexadecane contact angle (HCA) of nanometer-thick lubricants on COC were measured using a VCA Optima Contact Angle system. 1.5 μL drops of

testing liquids were automatically dispensed on the surfaces, and the drop shapes were captured by a CCD camera and analyzed by the vendor-supplied software. The CA on each sample was averaged by measuring at more than three locations.

The coefficient of friction (COF) was measured using a CSM Instruments Nanotribometer with a dual beam cantilever and high-resolution capacitive sensors. A stainless steel ball with 2 mm in diameter was used as the counterface and was cleaned with isopropanol between trials. The normal load, maximum linear speed, amplitude, and cycle were set as 10 mN, 0.20 cm/s, 2.00 mm, and 50 cycles, respectively. Each surface was tested for at least three trails.

The bonded ratio was measured to understand the bonding interactions between the IL lubricants and the COC surface.[13, 89] The coated media was washed by dipping into and subsequently removed from pure Vertel XF at 1 mm/second. The thickness of the remaining lubricant layer was measured by ellipsometry.

6.3 Results and Discussion

6.3.1 Synthesis and Characterizations of ILs

Scheme 2(a) illustrates the two-step synthetic path of FIL-OH, i.e., 1-1H,1H,2H,2H-perfluorohexyl-3-2-hydroxylethylimidazolium bis(trifluoromethylsulfonyl)imide, which contains a highly fluorinated alkyl chain and a hydroxyl endgroup in the imidazolium cation and a fluorinated [NTf_2] anion. The first step of the synthesis undergoes the S_N2 reaction, where the highly fluorinated alkyl chain is added in the imidazolium cation that contains a hydroxyl endgroup. Initially, 21.8 mmol 1-Iodo-1H,1H,2H,2H-perfluorohexane was dissolved in 35 mL

toluene at 110 ℃ under stirring. 24.0 mmol 1-(2-hydroxyethyl)imidazole was added to the solution, and the reaction was refluxed at 110 ℃ under N_2 purging for 16 hr. Then toluene was decanted after the system cooled to RT. The remaining wax was stirred in 200 mL diethyl ether, and the mixture was stirred and washed with 150 mL diethyl ether three times and dried under vacuum overnight. The second step is a metathesis reaction, where the $[NTf_2]^-$ anion replaces the iodide anion. The waxy product from the first step was dissolved in 80 mL DI water at 65 ℃ under stirring. 21.8 mmol lithium bis(trifluoromethane)sulfonimidate was added, and the reaction was stirred at 65 ℃ for 4 hours. Afterward, the product was dissolved in 200 mL ethyl acetate and washed with 100 mL DI water four times until pH 6-7. The final product was acquired after rotary evaporation and dried in a vacuum oven overnight. The synthesized FIL-OH, 1-1H,1H,2H,2H-perfluorohexyl-3-2-hydroxylethylimidazolium bis(trifluoromethylsulfonyl)imide, is a viscous liquid in yellow color.

Scheme 2(b) illustrates the two-step synthetic path of HFIL-OH, i.e., 1-1H,1H,2H,2H-perfluorohexyl-3-2-hydroxylethylimidazolium Bis(nonafluorobutanesulfonyl)imide, which contains a highly fluorinated alkyl chain and a hydroxyl endgroup in the imidazolium cation and an even more fluorinated Bis(nonafluorobutanesulfonyl)imide anion than the [NTf2] anion. The S_N2 reaction in the first step is the same as the synthesis of FIL-OH. The Bis(nonafluorobutanesulfonyl)imide anion replaces the iodide anion by the metathesis reaction in the second step. The waxy product from 21.8 mmol 1-Iodo-1H,1H,2H,2H-perfluorohexane and 24.0 mmol 1-(2-hydroxyethyl)imidazole in the first step was again dissolved in 80 mL DI water at 65 ℃ under stirring. 21.8 mmol lithium bis(trifluoromethane)sulfonimidate was added, and the reaction was stirred at 65 ℃ for 4 hours. The product was then dissolved in 200 mL ethyl acetate and washed with 100 mL DI water four times. The final product was acquired after rotary

evaporation and dried in a vacuum oven overnight. The synthesized HFIL-OH, 1-1H,1H,2H,2H-perfluorohexyl-3-2-hydroxylethylimidazolium bis(trifluoromethylsulfonyl)imide, is a highly viscous liquid in dark yellow color.

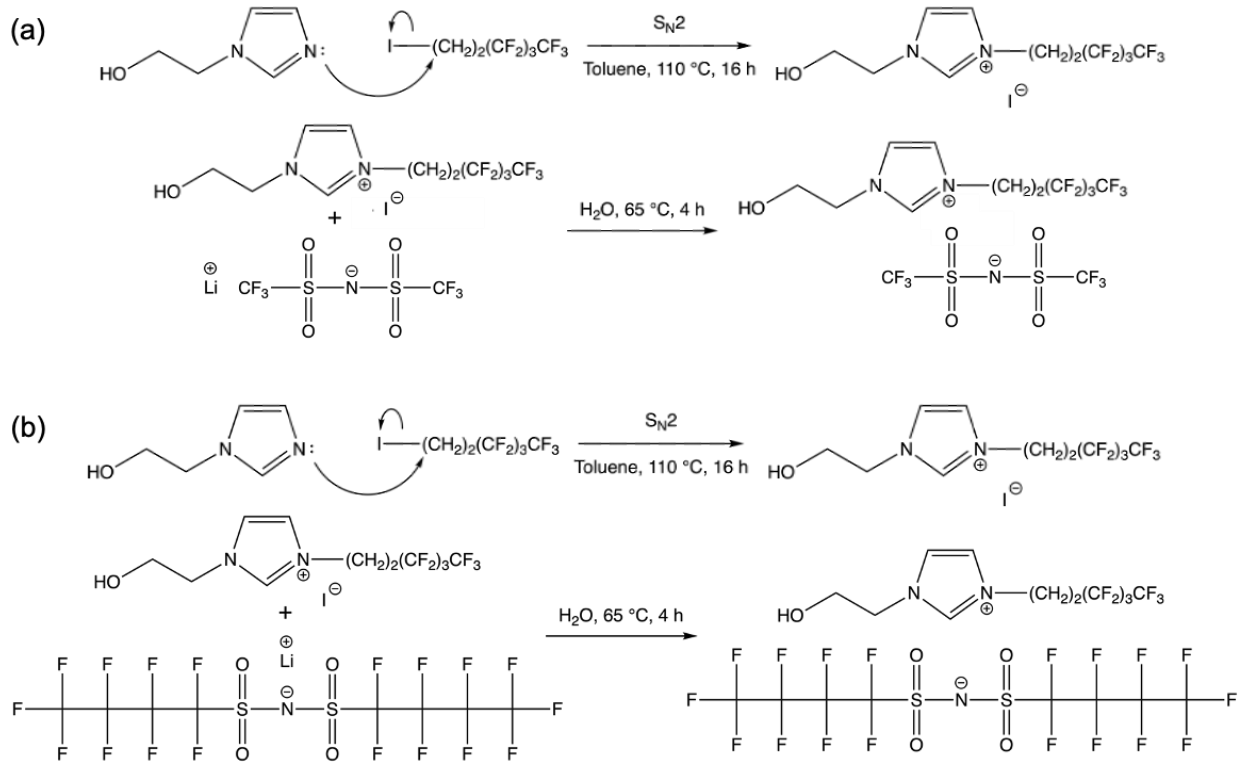

Scheme 2. Synthesis of (a) FIL-OH and (b) HFIL-OH.

^{1}H NMR analysis was conducted on the synthesized FIL-OH and HFIL-OH, as shown in Figure 36. The peak shift, the peak integral, and the multiplet splitting for all the assigned peaks demonstrate the successful synthesis of the two ILs. It is worth noting that the peak at 2.5 ppm is from the trace impurities of the solvent DMSO-d_6, and the peak at 3.3 ppm is from absorbed water in the solvent.[143] Additionally, as shown by the TGA results in Figure 37, only one major step of weight loss can be detected for the synthesized ILs, demonstrating the relatively high purity of the product. The TGA results also indicate that FIL-OH and HFIL-OH have significantly higher

thermal stability than PFPE Ztetraol because of the strong electrostatic interactions within ILs. The major weight loss was at ~350 °C for FIL-OH and HFIL-OH, while the weight loss started at ~150 °C for Ztetraol. It is worth noting that there is ~4% weight loss before 200 °C for HFIL-OH, which can be attributed to the trace amount of impurity. The excellent thermal stability of FIL-OH and HFIL-OH is ideal for their applications in lubrication due to the rising temperature during tribology contact and the high thermal stability requirement for HAMR. In addition to the bulk thermal stability, the thermal stability of the nanofilms of PFPE Zdol and ILs on silicon wafers were also investigated in a previous study.[11] Assuming 1 ns duration per HAMR laser write and lubricant lifetime of <50% nanofilm loss, the lifetime of the nanometer-thick [Bmim][FAP] lubricant is ~4 times longer than the nanometer-thick Zdol lubricant at the operating temperature of 400 °C.

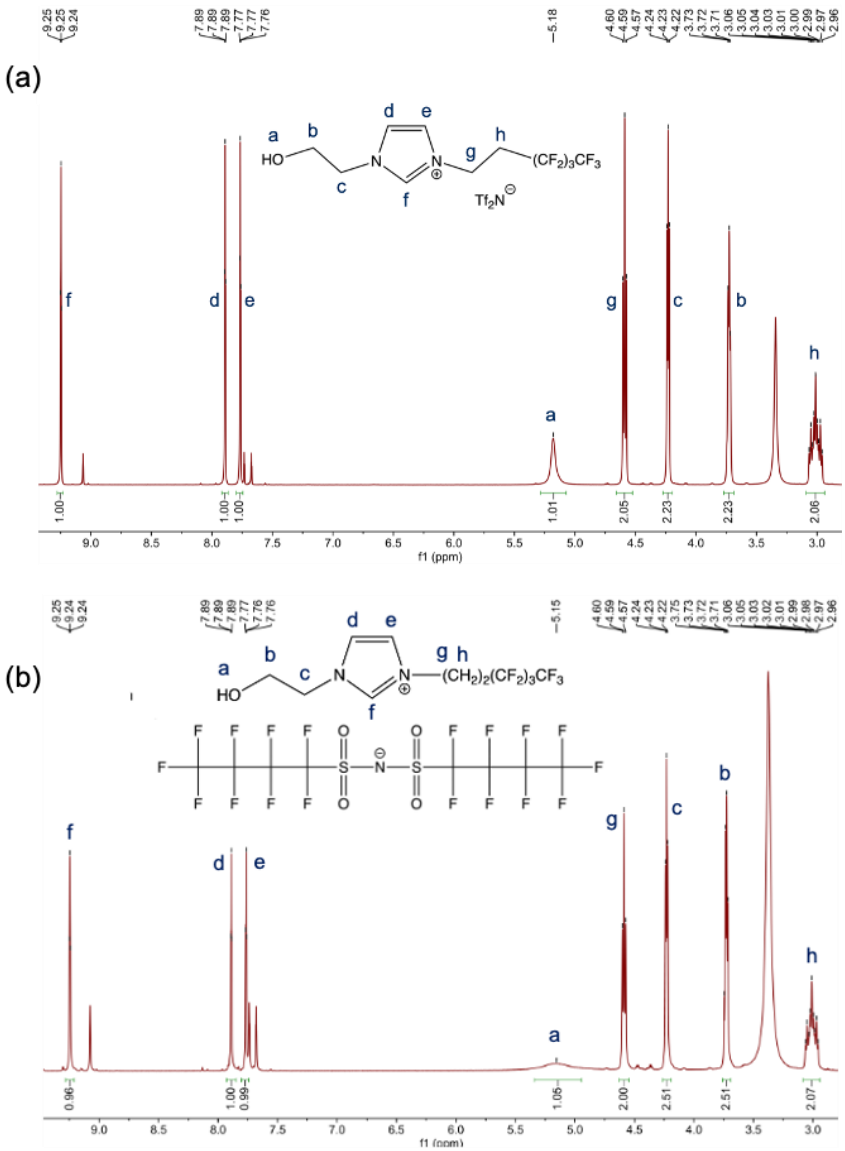

Figure 36. ^{1}H NMR spectrum of (a) FIL-OH and (b) HFIL-OH. The peak assignments are labeled.

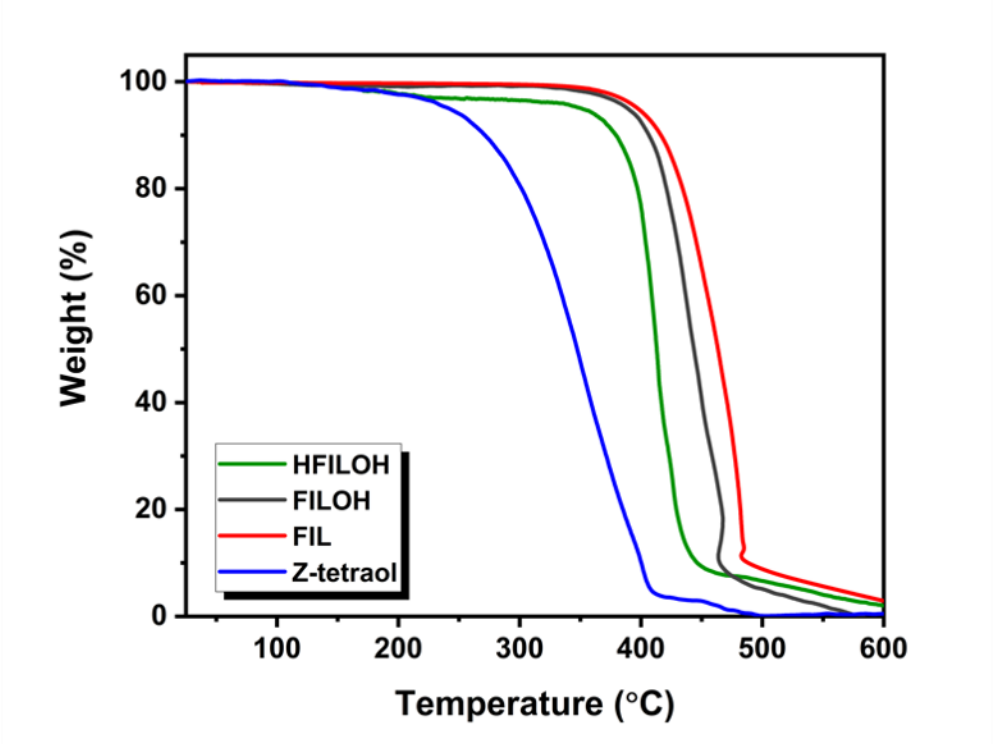

Figure 37. TGA results of bulk FIL-OH and HFIL-OH. Ztetraol and FIL are used as control.

6.3.2 Reduced Surface Tension and Enhanced Bonding

A highly fluorinated C_6 alkyl chain has been added in the cations of FIL-OH and HFIL-OH. The substitution of multiple fluorinated components in the FIL-OH cation is expected to induce a low surface tension, since the strong C–F bonds and the low polarity can lead to weak intermolecular forces and consequently low surface tensions. The surface tension of HFIL-OH is expected to be even lower than FIL-OH due to the substitution of the highly fluorinated anion in HFIL-OH. The surface tensions of the synthesized ILs were measured by the pendant drop method and compared with FIL, [Bmim][FAP], and PFPEs Zdol and Ztetraol. As shown in Table 7, the surface tension FIL-OH is reduced to 24.8 mN/m, which is significantly lower than that of

[Bmim][FAP] (i.e., 32.4 mN/m) and comparable to the surface tensions of FIL (24.5 mN/m) and PFPE Zdol (24 mN/m). The surface tension HFIL-OH is further reduced to 18.2 mN/m, which is much lower than that of Ztetraol (22.4 mN/m).

Table 7. Surface tension ($\boldsymbol{\gamma}$) of FIL-OH and HFIL-OH at RT, with [Bmim][FAP], Zdol and Ztetraol as control

	FIL-OH	HFIL-OH	FIL[14]	[Bmim][FAP]	Zdol[144]	Ztetraol[135]
γ (mN/m)	24.8	18.2	24.5	32.4	24.0	22.4

FIL-OH and HFIL-OH nanofilms with various thicknesses were fabricated from solutions at various concentrations by dipcoating, and the nanofilm thicknesses are shown in Figure 38. Figure 39(a) presents the WCA and HCA results on the FIL-OH coated COC with varying film thicknesses. The HCA results on the FIL-OH nanofilms are higher than HCA on bare COC, but the WCA results on the FIL-OH nanofilms are lower than WCA on bare COC. It was previously proposed that the small water molecules always instantly travel through the relatively big intermolecular pores in the FIL-OH nanofilms and rest on the composite of nanofilms and COC.[14, 145] The WCA results on FIL-OH nanofilms are lower than the WCA results on bare COC and FIL nanofilms possibly because of the effect of the hydroxyl group in the cation. The hexadecane molecules, which are much bigger than the water molecules, sits on the nanofilm surfaces only, since they cannot go through the intermolecular pores in the FIL-OH nanofilms.[145] As a result, the HCA results are higher on the FIL-OH nanofilms than on bare COC. The low WCA results indicate that the coverage of the fluorinated segments on the solid surface is limited for FIL-OH nanofilms.

The WCA and HCA on the HFIL-OH nanofilms, on the other hand, are both higher than the WCA and HCA results on bare COC, FIL nanofilms, and FILOH nanofilms, as shown in Figure 39(b). The high WCA and HCA results on the HFIL-OH nanofilms indicate that the more fluorinated segments from the highly fluorinated anion in the HFIL-OH molecule can significantly reduce the surface energy of the coated surface. The significantly lower surface tension of HFIL-OH is ideal for reducing the adhesion between the sliding component and the substrate and eliminating airborne contaminations, which can consequently induce more robust tribological performance.[147]

To investigate the bonding of the IL lubricants on COC, the FIL-OH and HFIL-OH nanofilms at various thicknesses were washed with pure Vertrel, and the remaining thicknesses are shown in Figure 38. The FIL nanofilms before and after washing are used as control. A layer of lubricant with a thickness of ~0.3-0.4 nm remains on COC for the FIL-OH nanofilms, and a layer of lubricant with a thickness of ~0.4-0.5 nm remains on COC for the HFIL-OH nanofilms. Specifically, the AFM image of the HFIL-OH nanofilm fabricated from the 3 g/L solution after washing is shown in the inset of Figure 38(b). The surface is very smooth with a low root-mean-square (RMS) roughness of 0.115 nm. The HCA on the washed HFIL-OH nanofilm is 49.5° compared to the ~0° HCA on bare COC, further demonstrating there remains a smooth lubricant layer. The ellipsometry tests after washing indicate that some FIL-OH and HFIL-OH molecules bond to the polar sites on the COC surface by strong hydrogen bonding, similar to the bonding of PFPE.[13, 89] In comparison, FIL molecules only bond on COC by weak van der Waals interactions due to no functional endgroups,[13, 14] so almost nothing survives the Vertrel washing. It is remarkable to have such improved bonded ratios for the novel FIL-OH and HFIL-OH boundary lubricants. The mobile lubricants are displaced during device operations, while the bonded lubricants still cover the solid surface asperities and prevent direct solid/solid contacts.[13, 33, 149]

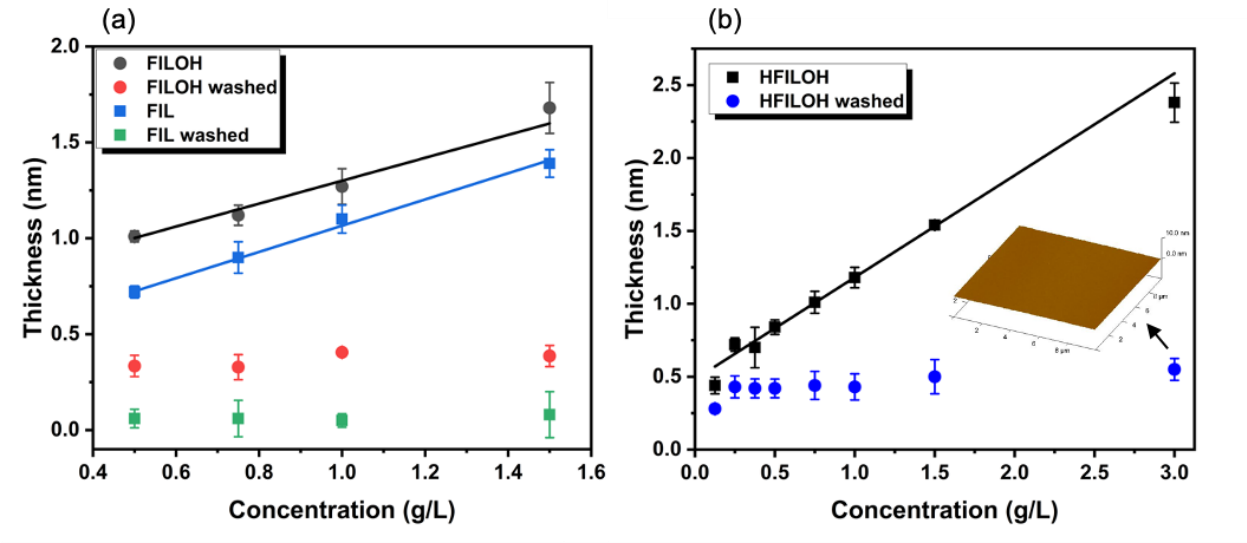

Figure 38. Nanofilm thicknesses of (a) FIL-OH and (b) HFIL-OH before and after Vertrel washing. FIL nanofilms and bare COC are used as reference.

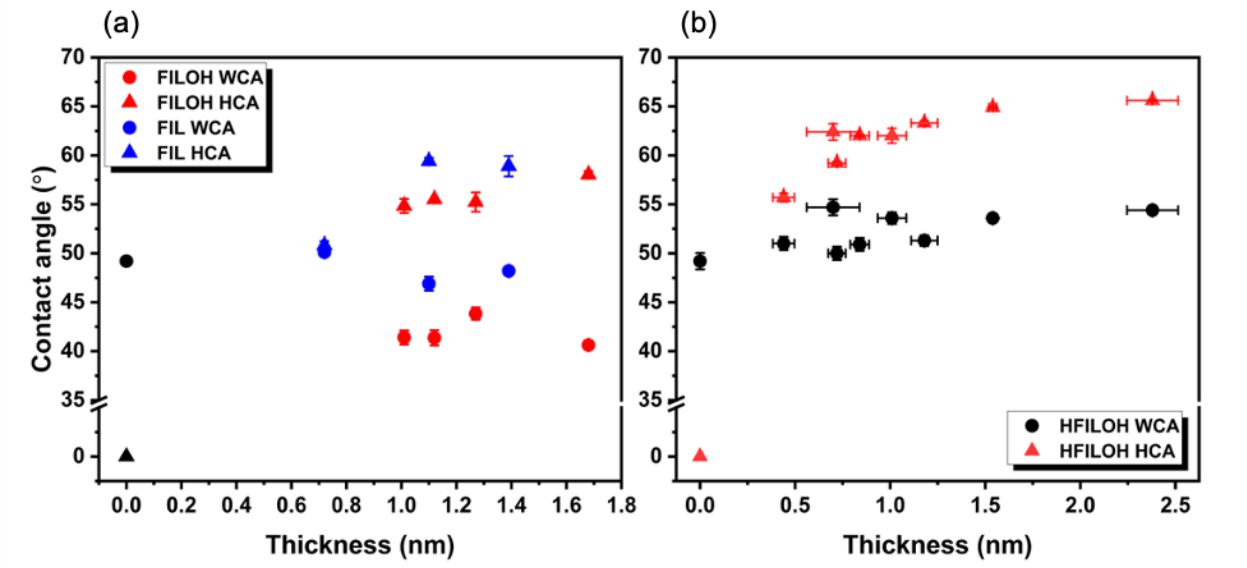

Figure 39. CA results on the FIL-OH and HFIL-OH nanofilms.

6.3.3 Nanometer-Thick ILs as Media Lubricant

In a hard disk drive (HDD), thinner media lubricants are desired as the head-media spacing needs to be smaller to achieve a high areal density.[11, 13, 116] The ML thickness of the lubricant governs the thinnest possible nanofilm that fully covers the solid surface while remains smooth.[119, 121] The ML thickness can be determined from the change in the RMS surface roughness by AFM with the nanofilm thickness.[13, 14] When the film thickness exceeds the ML thickness, a significant increase in surface roughness and a topography change from a smooth nanofilm to dewetting will occur. Figure 40 shows the AFM surface roughness results for the IL nanofilms with various thicknesses on COC. The surface roughness results of PFPE Ztetraol and FIL were used as control. The ML thickness of Ztetraol is ~1.6 nm,[13] which is close to its R_g of 1.5 nm.[131] The ML thickness of FIL has been previously determined as ~0.9 nm,[13] which is close to the size of a FIL molecule (0.85 nm), assuming the FIL molecule is cubic.[14] Based on the AFM surface roughness results, the ML thickness of the synthesized FIL-OH lubricant is ~1.1 nm, close to the ML thickness of FIL and much lower than the ML thickness of PFPE Ztetraol. The FIL-OH nanofilms are very smooth at the thinner regime (≤1.1 nm), and the RMS values are low. At this stage, the nanofilm covers more solid areas as the film grows thicker. The π-π stacking between imidazolium cations and the amorphous COC surface initiates the FIL cations to form a layer of film on the COC surface and the subsequent layering of the anions on the cation layer.[46, 134] It is worth noting that the IL film does not entirely cover the COC surface, as demonstrated by the low WCA on the IL film. AFM cannot reveal the detailed surface morphology smaller than the 39 nm pixel size in the lateral directions. When the nanofilm grows thicker than ML, the intermolecular cohesion of IL molecules has more impact than the π-π interaction at the IL/COC interface,[16] so significant increases in the

surface roughness and the dewetting topography were observed. Besides, assuming the FIL-OH molecule is cubic, the edge length a of each cubic molecule is estimated to be 0.86 nm based on $a = \sqrt[3]{\frac{M/N_A}{\rho}}$, where M is the molar mass (639.38 g/mol), ρ is the bulk density (1.69 g/mL at RT), and N_A is the Avogadro constant. The 0.86 nm size of the molecule is also comparable to the ~1.1 nm ML thickness determined from the AFM surface roughness results.

Similarly, the ML thickness of the synthesized HFIL-OH lubricant on COC is determined to be ~0.75 nm based on the AFM surface roughness results in Figure 40(b). The HFIL-OH nanofilms are very smooth at the thinner regime (≤0.75 nm) due to the π-π stacking at the IL/COC interface, and the nanofilm only covers more solid areas as it grows. When the nanofilm grows thicker than ML, dewetting and increases in RMS were observed due to the dominating cohesion interaction within HFIL-OH. Based on the 939.44 g/mol molar mass and 1.67 g/mL bulk density, the molecule size of HFIL-OH can be estimated to be 0.98 nm, close to the ~0.75 nm ML thickness determined from AFM surface roughness results and much lower than the ML thickness of PFPE Ztetraol. Compared to Ztetraol, the thinner ML thicknesses of the novel FIL-OH and HFIL-OH provide the lower minimum thickness of the nanometer-thick lubricants, which provides the opportunity to achieve a higher areal density in the next-generation HDD.

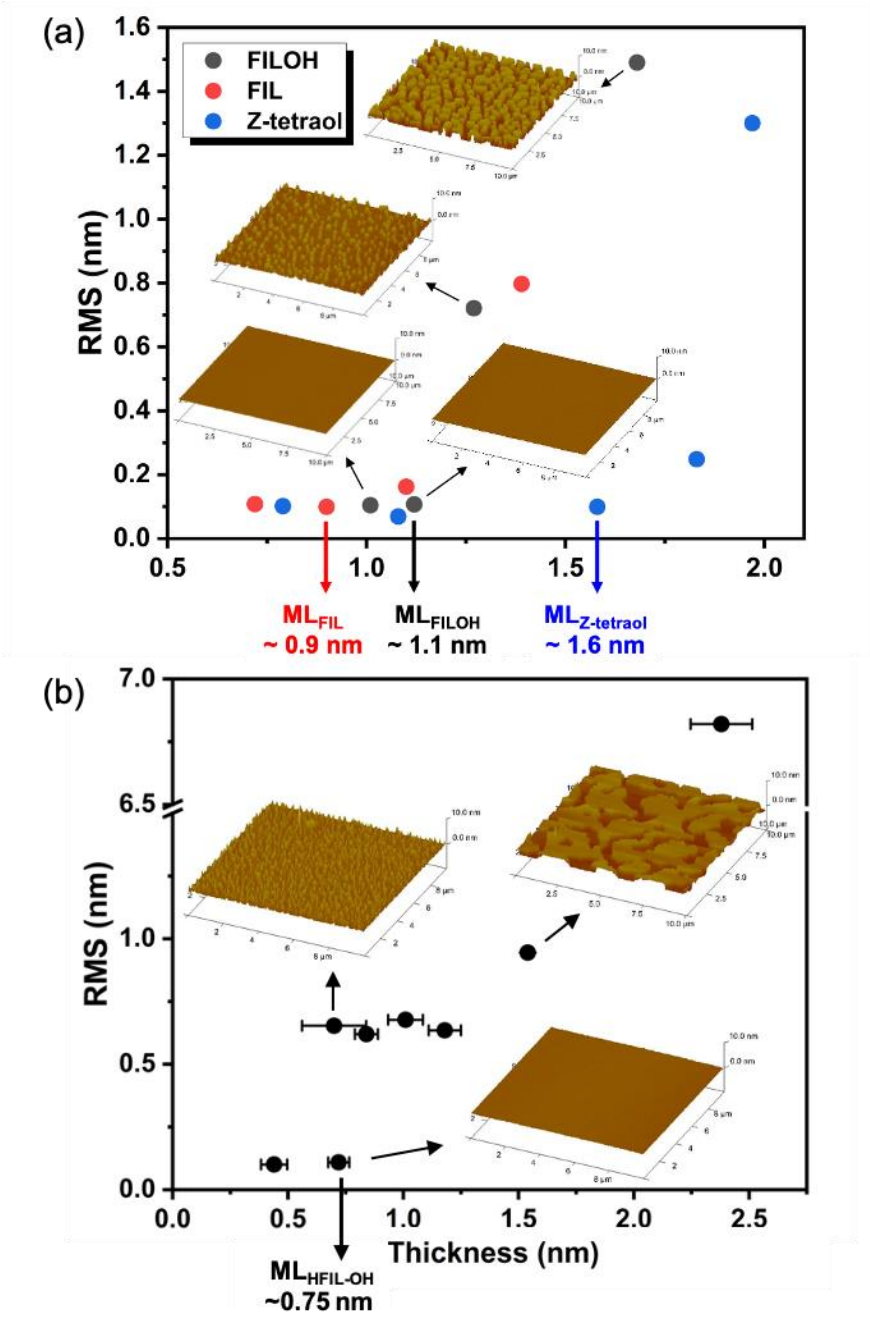

Figure 40. Surface roughness results of the nanometer-thick lubricants of (a) FIL-OH and (b) HFIL-OH on COC. The insets are AFM images of the IL nanofilms at various thicknesses.

Nanotribology testing has been performed for the nanometer-thick lubricants at various thicknesses on COC, and the coefficient of friction (COF) results are shown in Figure 41. The

COF results of the bare COC (i.e., 0.444 ± 0.024), Ztetraol, and FIL were used as control. Despite the reduced surface tension and the enhanced bonding on COC for FIL-OH and HFIL-OH, the friction of the FIL-OH and HFIL-OH lubricants are still not at the same level as the friction of the Ztetraol lubricant. However, low adhesion, which is determined by the low van der Waals force of the lubricant molecules, is also critical for good boundary lubrations.[1, 31] Due to the presence of the highly fluorinated components in the two novel ILs, especially in HFIL-OH, low adhesion for the novel IL boundary lubricants is expected. Adding more functional endgroups in the next-generation HFIL-OH lubricant may further promote bonding of the molecule to solid surfaces, which may induce the molecular orientation to favor tribological performance. Moreover, the $(CF_2)_x$ alkyl chains in the IL cations may be too rigid for lubrication. Instead of substituting the fluorinated C_6 alkyl chain, substituting a softer and more flexible chain similar to the backbone of PFPEs, i.e., $–CF_2CF_2OCF_2CF_3$, could significantly promote the tribological performance.

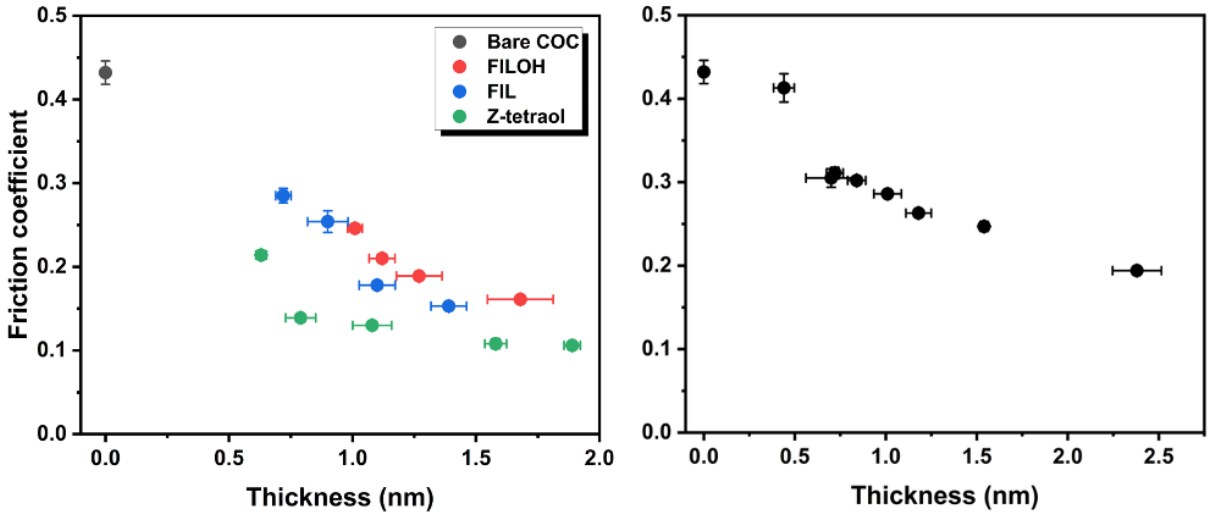

Figure 41. Friction results of the nanometer-thick FIL-OH and HFIL-OH lubricants on COC.

6.4 Conclusions

In summary, we report our successful synthesis of two novel fluorinated ILs with functional endgroups through two-step reactions. The first IL, FIL-OH, contains a hydroxyl endgroup and a highly fluorinated alkyl chain in the cation. FIL-OH has enhanced bonding to the COC surface due to its hydroxyl endgroup, but the coverage of the fluorinated segments on COC is still limited based on CA results. The second IL, HFIL-OH, contains the same cation with the hydroxyl endgroup and the highly fluorinated alkyl chain as FIL-OH, but it contains an even more fluorinated anion instead. The bonding between HFIL-OH and COC is also enhanced due to the addition of the hydroxyl group in the cation. The surface tension of the HFIL-OH lubricant is significantly lower than the state-of-the-art PFPE lubricants. The surface energy of the HFIL-OH coated COC surface is greatly reduced due to the addition of the highly fluorinated anion, indicating a rich coverage of the fluorinated segments. However, the COF results of the two novel IL lubricants are still higher than PFPE Ztetraol, which enlightens the future direction of adding more functional groups and substituting a flexible fluorinated alkyl chain for the molecular design of the next-generation IL lubricant.

7.0 Summary and Future Work

7.1 Summary

7.1.1 Molecular Structure of Solid-Confined ILs

In summary, we first report that tuning humidity is an effective approach manipulating the molecular arrangement and macroscopic wettability of ILs on the mica surface. We have provided direct experimental evidence showing that, under different humidity, the molecular arrangement of ILs on the mica surface could be droplet, "pancake", or extended layering. Meanwhile, the macroscopic wettability increases with the relative humidity. The experimental results suggest that the underlying mechanism is the water-enabled ion exchange between K^+ and the IL cation and the resulting layering of ILs. At low humidity (low water adsorption), the K^+ dissolution is very limited and thus the ion exchange is hindered. As a result, the IL takes a droplet structure at nanoscale and the macroscopic wettability is lower. At high humidity (high water adsorption), the K^+ is dissolved and mobilized, which enables the ion exchange between K^+ and IL cations and initiates the layering of ILs. Therefore, the IL takes an extended layering structure at nanoscale and the macroscopic wettability is higher. The finding here potentially provides a new dimension tailoring the performance of ILs at the IL/solid interface.

In the next work, the interfacial molecular structures of mica-confined ILs with various alkyl chain lengths in the cations, i.e., [Emim][FAP], [Bmim][FAP], and [Hmim][FAP], have been systematically investigated by AFM. Quantized growths of the nanofilms of [Emim][FAP] and [Bmim][FAP] at RH > 30% have been directly observed. Initially, the IL films only cover more

solid surface areas at the constant film thickness of 2 ML. Then a quantized increase in the film thickness by 2 ML was observed. The nanofilm thickness remains constant afterward as the nanofilm grows. The AFM thickness results directly indicate that the cation alkyl chain length has no impact on the thermodynamic equilibrium states of the nanofilm topographies. As a result, we have proposed a double-layering interfacial molecular arrangement of IL cations and anions on the mica surface. Within the building block, the first two layers adjacent to the mica surface are cation layers with the imidazolium rings perpendicular to mica and the closely-packed alkyl tails parallel to mica, and two anions sit on top of the two cations. Meanwhile, the time-dependent AFM results at RH < 20% reveal the effect of the cation alkyl chain length on the spreading kinetics of mica-confined IL nanofilms. The spreading is slower for ILs with longer alkyl chains due to the stronger intermolecular dispersive interactions. Our results provide direct proofs and detailed insights into the molecular structures of ILs confined on solid surfaces.

7.1.2 Nanometer-Thick ILs as Novel Media Lubricants

In summary, we have highlighted the potential of nanometer-thick fluorinated ILs as novel media lubricants. The TGA results indicated that [Bmim][FAP] has higher thermal stability than Z-tetraol, which is mainly attributed to the electrostatic interaction of the ion pairs in the IL. This characteristic is critical to the application of the IL as a HAMR lubricant. More importantly, the ML thickness of [Bmim][FAP] on COC is only ~50% of that of Z-tetraol based on the surface roughness results by AFM, which provides the opportunity to scale down the thickness of the nanometer-thick films and thus increase the areal density. We concluded that the intrinsically small molecular size of the IL induces a lower ML thickness. The lower ML thickness of [Bmim][FAP] over Z-tetraol was further supported by the friction results of the nanometer-thick films confined

on COC. The COF of the nanometer-thick [Bmim][FAP], however, is slightly higher than that of the PFPE, which indicates the direction for synthesizing the next-generation ILs with more fluorinated components and hydroxyl groups to reduce the surface tension and enhance the bonding to solid substrates.

In the next work, we report our successful synthesis of a novel FIL lubricant with a highly fluorinated cation alkyl chain. The molecular structure and the purity of the synthesized FIL were confirmed by ^{1}H NMR and TGA. The TGA results also suggested that FIL has higher thermal stability than PFPEs. Compared to the commercially available IL lubricant, a significant decrease in the surface tension of FIL was achieved due to its highly fluorinated molecule structure. AFM surface roughness results revealed that the ML of FIL is much thinner than Ztetraol, which is expected to induce a lower minimum thickness of the nanometer-thick lubricants and hence a potentially higher areal density in HDDs. Moreover, the friction results demonstrate the COF of the nanometer-thick FIL lubricant on COC is lower than the commercially available IL because of the intrinsically lower surface tension of FIL. Our results indicate that FIL is promising as the next-generation boundary lubricant in HDDs. As the friction of the current FIL lubricant is comparable to yet still slightly higher than the PFPE Ztetraol lubricant, the future design of FIL lubricant needs to have enhanced bonding to the solid substrate and an even lower surface tension.

Then we report our successful synthesis of two novel fluorinated ILs with functional endgroups through two-step reactions. The first IL, FIL-OH, contains a hydroxyl endgroup and a highly fluorinated alkyl chain in the cation. FIL-OH has enhanced bonding to the COC surface due to its hydroxyl endgroup, but the coverage of the fluorinated segments on COC is still limited based on CA results. The second IL, HFIL-OH, contains the same cation with the hydroxyl endgroup and the highly fluorinated alkyl chain as FIL-OH, but it contains an even more

fluorinated anion instead. The bonding between HFIL-OH and COC is also enhanced due to the addition of the hydroxyl group in the cation. The surface tension of the HFIL-OH lubricant is significantly lower than the state-of-the-art PFPE lubricants. The surface energy of the HFIL-OH coated COC surface is greatly reduced due to the addition of the highly fluorinated anion, indicating a rich coverage of the fluorinated segments. However, the COF results of the two novel IL lubricants are still higher than PFPE Ztetraol, which enlightens the future direction of adding more functional groups and substituting a flexible fluorinated alkyl chain for the molecular design of the next-generation IL lubricant.

7.2 Future Work

7.2.1 Molecular Structure of Solid-Confined ILs

To further support the proposed double-layering interfacial molecular arrangement of IL cations and anions on mica based on the equilibrium nanofilm topographies under AFM, molecular dynamics simulations on the molecular structure of ILs near the mica surface will be conducted in future work. Angle-resolved XPS (ARXPS) will also be conducted to support our proposed interfacial molecular model from the nitrogen/fluorine intensity ratio at various emission angles and thicknesses.

In addition to ILs on mica, the interfacial molecular structures of ILs on more model solids, including silica with negatively charged surface and amorphous carbon such as COC, will also be systematically investigated. The ILs studied will not be limited to imidazolium ILs with the [FAP] anion. ILs containing other anions, i.e., bis(nonafluorobutanesulfonyl)imide, [NTf_2], [BF_4], and

[PF_6], will also be utilized. The different anions could change the surface tension, hydrophobicity, viscosity, and size of the ILs, which may impact the molecular structure on solid surfaces. The results are expected to provide more comprehensive information on the interfacial molecular arrangement of solid-confined ILs.

7.2.2 Nanometer-Thick ILs as Novel Media Lubricants

Our industry partner is currently performing component-level testing on FIL and HFIL-OH. The component-level testing results, together with all the current results on the novel IL lubricants, i.e., FIL, FIL-OH, and HFIL-OH, could be another step forward for the application of ILs as the next-generation media lubricants for the hard disk drive industry.

Meanwhile, the spreading tests and the mobility tests will also be performed. Nanometer-thick IL lubricants will be applied on half of the COC disk by dipcoating. The IL/COC/air contact line will be monitored by ellipsometry and tapping-mode AFM at various lead time to determine the mobility of the nanometer-thick IL lubricants.

The molecular structure of ILs should also be tailored by synthesis to further optimize the lubrication performances. Adding more functional endgroups in the next-generation HFIL-OH lubricant can promote bonding of the molecule to solid surfaces, which may induce the molecular orientation to favor tribological performance. Moreover, the $(CF_2)_x$ alkyl chains in the IL cations may be too rigid for lubrication. Instead of substituting the fluorinated C_6 alkyl chain, substituting a softer and more flexible chain similar to the backbone of PFPEs, i.e., $(CF_2CF_2O)_m(CF_2O)_n$, could significantly promote the tribological performance. Additionally, we plan to add antioxidant groups, i.e., aromatic amine groups and hindered phenolic groups, in the IL molecules to achieve the antioxidation capability for the IL lubricants.

Appendix A 3D-Printed Repeating Re-Entrant Topography to Achieve On-Demand Wettability and Separation

The material in this chapter is based upon the published work *ACS Appl. Mater. Interfaces* 2020, 12, 31, 35725–35730.

Appendix A.1 Introduction

Superwetting surfaces in nature, e.g., lotus leaf[151], fish skin[152], and water strider leg[153], have been extensively studied in the past three decades. The biomimetic superhydrophobic and superoleophobic surfaces require the microscale and nanoscale hierarchical surface textures, combined with coatings with low surface energy[154, 155]. Based on the Cassie-Baxter model[148, 156], the superhydrophobic states result from the air trapped at the liquid/solid interface due to the surface roughness, and the fact that liquids rest on top of the air/solid composite. The apparent contact angle (CA) can be determined by $cos\,\theta_{Apparent} = f\,cos\,\theta_{LS} + f - 1$, where θ_{LS} and f are the equilibrium CA on the flat solid surface and the solid fraction on the air/solid surface, respectively. The surfaces with the hierarchical features were usually fabricated using conventional manufacturing technologies, e.g., top-down approaches (lithography, chemical etching, anodization) and bottom-up approaches (coating, electrospinning, electrodeposition)[155]. However, the manufacturing process typically involves multiple complicated steps, and the fabrication of intricate structures is always very challenging. 3D printing is a promising alternative to conventional manufacturing methods. It can efficiently create a complicated assembly with high

resolution in a single-step process at a reasonable cost[157, 158]. Nevertheless, there has been only a handful of reports on the 3D-printed superwetting surfaces with well-controlled textures to date. Using immersed surface accumulation 3D printing, Yang et al.[159] produced a superhydrophobic eggbeater-shape surface with the addition of carbon nanotubes to enhance the roughness. Liu et al.[160] reported the successful fabrication of a superrepellent surface with complicated triply re-entrant features by 3D-printing. Li et al.[161] applied multiscale stereolithography to develop a superhydrophobic textured surface with artificial lotus leaf pillars.

However, these superhydrophobic and/or superoleophobic of surfaces are still limited in their long-term robustness and application in the separation of liquid mixtures. Here we report fabricating a novel repeating re-entrant topography via two-photon polymerization (2PP) 3D-printing. First, we have achieved the robust on-demand wettability of various liquids on the single re-entrant surface by precisely manipulating the re-entrant angle ($\theta_{Re-entrant}$). Second, we have demonstrated that 3D-printed repeating re-entrant surface, which has not been made via conventional techniques, further enhances the desired on-demand surface wettability. Last but not least, we have shown that the 3D-printed membranes with the repeating re-entrant pores can achieve efficient on-demand separations of liquid mixtures with high flux, which is promising in wastewater treatment.

Appendix A.2 Experimental Section

Appendix A.2.1 Fabrication of the Re-Entrant Structures

The computer-aided design (CAD) models were generated with a 3D modeling software and saved in STL (stereolithography) format. Subsequently, the STL files were converted into GWL (general writing lithography) files through a vendor-supplied software DeScribe. During the file conversion, all the printing parameters were determined, i.e., the slicing distance (0.2 μm), the hatching distance (0.2 μm), the laser power (40 mW), and the writing speed (10000 μm/s). The GWL files were then loaded to the operation software Nanowrite for 3D printing. 2PP 3D printing of the re-entrant surfaces and the re-entrant membranes was performed with a NanoScribe Photonic Professional GT 3D direct laser writer that was equipped with a femtosecond pulsed laser generator (780 nm wavelength) and 63x objective lens for high-resolution printing. The whole system was placed on an anti-vibration table to reduce the acoustic noise. The re-entrant structures were printed with Galvo mode for the lateral scanning and piezo mode for the vertical scanning. Fused silica substrates were used as printing platforms. The photoresist utilized was IP-Dip, which is mainly composed of 2-(hydroxymethyl)-2-[[(1-oxoallyl)oxy]methyl]-1,3-propanediyl (60%-80%). After printing was completed, the samples were developed in SU-8 for 10 minutes, rinsed in isopropanol for 1 minute, and then dried under ambient air. All the samples were further cured in an ultraviolet chamber at 40 °C for 10 minutes.

Appendix A.2.2 Modification of Surface Chemistry

The surface chemistry of the re-entrant surfaces was modified for water repellency testings by applying a nanometer-thick film of perfluoropolyether (PFPE). 1 g/L solution of PFPE z-tetraol in Vertrel XF (2,3-dihydrodecafluoropentane) was prepared. The substrates were dipped into and withdrawn from the solution vertically at a constant speed of 1 mm/s using a KSV Instrument dipcoater. The PFPE-coated surfaces were then heated at 60 °C for 2 hours to render the hydroxyl groups to bond to the solid and the fluorinated backbones to orient toward air.[144, 162]

Appendix A.2.3 Fabrication of the Holder for the Separation Membrane

The liquid holder for the re-entrant separation membrane was designed with 3D modeling software and fabricated with a desktop 3D printer Formlabs Form 2. After the printing was completed, the holder was washed in isopropanol for 10 minutes and cured in an ultraviolet chamber at 40 °C for 30 minutes. The liquid holder and the re-entrant separation membrane were then sealed with fluoroelastomer.

Appendix A.2.4 Chemicals and Materials

DI water (18.2 MΩ·cm) was produced by a MilliporeSigma Milli-Q water purification system. The photoresist, the fused silica substrates, and SU-8 were vendor-supplied. All other testing liquids and solvents were purchased from Sigma-Aldrich and used as received. PFPE z-

tetraol and the solvent Vertrel XF were obtained from Solvay Solexis Inc. and Miller-Stephenson Chemical Company, respectively, and utilized as received.

Appendix A.2.5 Imaging

SEM imaging was conducted using a Zeiss SIGMA VP Scanning Electron Microscope with a Schottky thermal field emitter as the electron source. The accelerating voltage utilized was 10 kV, and the imaging was performed under high vacuum. As the 3D-printed surfaces are essentially made of nonconductive polymers, 12 nm Au/Pd sputter coating was applied in advance to avoid charging and reduce thermal damage. Optical microscopy imaging was conducted using a Carl Zeiss Axio Lab A1 microscope equipped with a Zeiss AxioCam ERc5s camera.

Appendix A.2.6 Contact Angle Measurement

The microscopic CA testing was performed with a VCA Optima XE system. 2 μL liquid drops were dispensed on the testing surfaces unless otherwise stated, and the droplet images and videos were taken by a charged coupled device (CCD) camera and analyzed with the vendor-supplied software.

Appendix A.3 Results and Discussion

Appendix A.3.1 Design and Fabrication of the Surface Texture

Assuming no external pressure is applied, the physics of a liquid on a solid surface with straight-wall opening can be described by the Young-Laplace equation $\Delta p = \frac{2\gamma \cos \theta_{LS}}{r}$, where Δp is the Laplace pressure, γ is the liquid surface tension, r is the diameter, and θ_{LS} is the liquid CA on the flat surface. A liquid always enters the opening as long as it wets the flat surface ($\theta_{LS} < 90°$), since both gravity and capillary force drive it into the opening[163]. However, it is possible that a liquid with $\theta_{LS} < 90°$ cannot enter the opening with a "re-entant" feature[164, 165], as shown in Figure S1a. On the one hand, as long as the re-entrant angle $\theta_{Re-entrant}$ is smaller than θ_{LS}, the capillary force counteracts the gravity, which prevents the liquid from entering the opening if the capillary force is larger than the gravity. As a result, the surface repels the liquid since air is trapped in the pore, and the interface is in Cassie state. On the other hand, both capillary force and gravity drive the liquid to enter the opening when $\theta_{Re-entrant} > \theta_{LS}$. Air is squeezed out of the pore as the liquid wets the surface, and Wenzel state is induced[166, 167]. Consequently, on-demand wettability of liquids with various θ_{LS} can be easily achieved on the re-entrant surfaces by designing $\theta_{Re-entrant}$ accordingly. For a given liquid, $\theta_{Re-entrant}$ can be tuned to be either smaller than θ_{LS} to achieve dewetting, or larger than θ_{LS} to achieve wetting, regardless of its wettability on the flat surface.

The microscale re-entrant surface (Figure S1b) can be readily fabricated by 3D-printing. The performed 3D-printing here is based on direct laser writing enabled by layer-by-layer 2PP. In 2PP, one molecule undergoes simultaneous two photon absorption (TPA) to reach its excited

state[168]. The absorption probability of TPA is proportional to the square of the laser intensity. As the polymerization happens only when the laser intensity exceeds a polymerization threshold, 2PP can be triggered only at the laser focal spot where the maximum absorption occurs[169, 170]. Consequently, the printing resolution can be as high as sub-micrometer.

In our first design, only one re-entrant layer is created and it is referred as the "single" re-entrant surface. Inverted truncated cones sit on top of 10 μm tall cylinders, and a 3 μm thick base was created under the cylinders to support the re-entrant structures. Based on previous reports[165, 171], the diameter of the circular disk (W) and the center-to-center distance of adjacent circular disks (D) are selected to be 10 μm and 30 μm, respectively. $\theta_{Re-entrant}$ is designed as 30°. This design is expected to make the liquids with $\theta_{LS} <$30° wet the surface. Meanwhile, the liquids with $\theta_{LS} >$30° is expected to exhibit high contact angle on the surface. The tilted views under SEM (Figure S1c, d) show the details of the 3D-printed single re-entrant surface. Compared with the design targets, W, D and $\theta_{Re-entrant}$ for the 3D-printed surface are within the error of 11%, 5.7% and 3.3%, respectively.

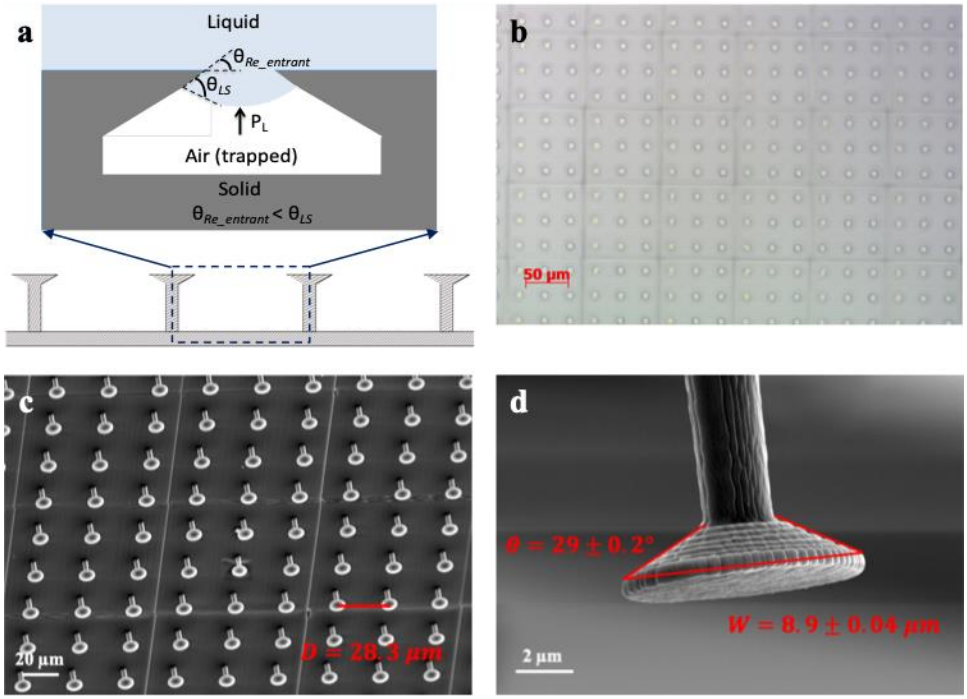

Appendix Figure 1. Design and fabrication of the re-entrant surface. (a) Physics of a liquid being repelled at the re-entrant structure. (b) Optical microscope image of the top view of the single re-entrant surface. (c) Tilted SEM image of the single re-entrant surface. (d) Tilted SEM image highlighting the details of the re-entrant structure.

Appendix A.3.2 On-Demand Wettability on the Single Re-Entrant Surface

The 3D-printed microscale single re-entrant surface has been demonstrated as a smart surface that can achieve on-demand wettability. Liquids with various surface tensions, including isopropanol, hexadecane, chlorobenzene, bromobenzene, dimethylformamide, benzyl alcohol, ethylene glycol, diiodomethane, and water, have been tested. To determine the CA on the flat surface (θ_{LS}), a flat surface is also fabricated by 3D-printing, and it has the same chemical composition as the re-entrant surface. The measured θ_{LS} for the testing liquids ranges from 0° to

71.0°. The wettability of these testing liquids on the single re-entrant surface is then investigated. Figure S2 shows the CA on the single re-entrant surface ($\theta_{Apparent}$) for liquids with different θ_{LS}. The dotted line in Figure S2 indicates the 30º $\theta_{Re-entrant}$ from the design. Complete wetting, i.e., CA approaching 0º, on the re-entrant surface is observed for liquids with $\theta_{LS} < 30°$, which can be attributed to the fact that the capillary force drives the liquids through the opening. However, the CA increases dramatically when θ_{LS} gets above $\theta_{Re-entrant}$. This is expected since the capillary force points upward and prevents the liquids from entering the opening, the liquid drops with $\theta_{LS} > 30°$ are strongly repelled by the re-entrant surface, exhibiting very high CA. Specifically, the 167.6° CA on the single re-entrant surface for water ($\theta_{LS} = 71.0°$) demonstrates that the surface is superhydrophobic. These results strongly support the design concept that the wettability of liquids with various surface tensions can be manipulated on the smart surface by simply modifying $\theta_{Re-entrant}$. For example, if it is desirable that a re-entrant surface is fully wetted by ethylene glycol ($\theta_{LS} = 52.6º$) yet repels DI water ($\theta_{LS} = 71.0º$), it can be achieved by having $\theta_{Re-entrant}$ between 52.6º and 71.0º. Superoleophobic re-entrant surfaces could also be fabricated by 2PP 3D printing as long as $\theta_{Re-entrant}$ is below θ_{LS} of the oils.

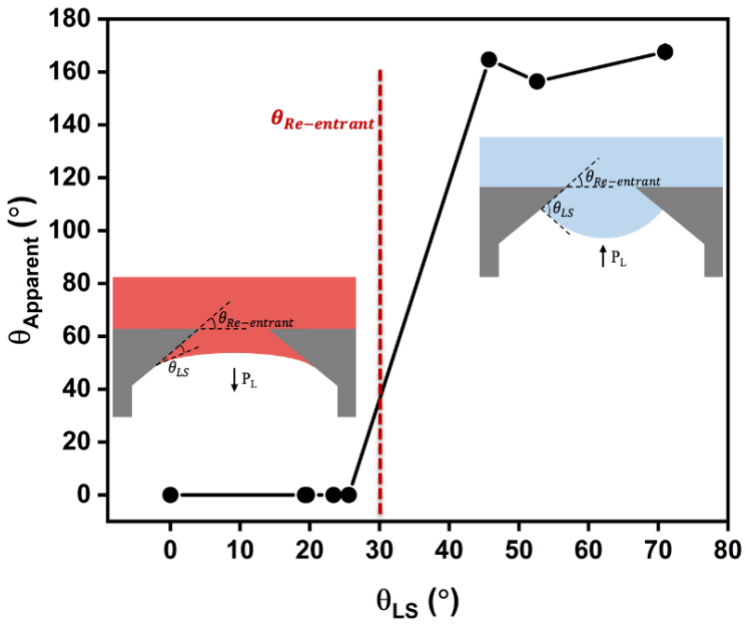

Appendix Figure 2. On-demand wettability on the single re-entrant surface. The dotted line indicates the 30º re-entrant angle ($\theta_{Re-entrant}$) in the current design. A sharp increase of the CA on the single re-entrant surface ($\theta_{Apparent}$) occurs when the CA on the flat surface (θ_{LS}) is higher than $\theta_{Re-entrant}$. The insets illustrate the physics of liquids wetting the re-entrant surface when $\theta_{LS} < \theta_{Re-entrant}$, and being repelled by the re-entrant surface when $\theta_{LS} > \theta_{Re-entrant}$.

Appendix A.3.3 Enhanced Water Repellency on the Repeating Re-Entrant Surface

To make the surface with $\theta_{Re-entrant} = 30°$ even more hydrophobic, the surface chemistry is modified by applying a nanometer-thick PFPE z-tetraol by dipcoating[13, 89]. The PFPE-coated sample is fully covered with water to test how robust the surface superhydrophobicity is. After one minute, the surface is taken out and tilted to let water flow away, and the WCA is immediately measured. It is worth noting that a single re-entrant wall around the re-entrant

structures is also created to exclude the possibility that water enters from the bottom. As water enters the single re-entrant structure and gets trapped during rinsing, a change from Cassie state to Wenzel state can be observed for the water drop on the surface[172]. Defects in the re-entrant structure from the manufacturing process could also drive water into the pores and initiate the Cassie-to-Wenzel transition. To further enhance the desired on-demand surface wettability, a repeating re-entrant topography with two re-entrant layers (Figure 3a) is designed.

In the repeating re-entrant design, each layer is composed of 5 μm-tall cylinders with inverted truncated cones on top. All the other design parameters, i.e., W (10 μm), D (30 μm), $\theta_{Re-entrant}$ (30°), and the thickness of the supporting base (3 μm), are the same as the single re-entrant design. A repeating re-entrant sidewall that surrounds the structures is also created to prevent water from entering from the bottom (see Figure S4b in the Supporting Information). Compared to the single re-entrant structure, the repeating re-entrant structure is even more difficult to fabricate by the conventional methods, while 3D-printing is a time- and cost-efficient approach to fabricating such complicated microscale structure. As shown by the SEM image in Figure S3b, the repeating re-entrant structure has been readily fabricated by 3D-printing. Figure S3c and Figure S4 also show the optical microscopy images of the top view of the repeating re-entrant surface, and the first and the second re-entrant layers. The nanometer-thick PFPE coating is again applied on the repeating re-entrant surface to enhance the superhydrophobic performance.

Compared to single re-entrant surface, more robust and reliable superhydrophobicity has been achieved on the repeating re-entrant surface. The repeating re-entrant surface even repels a 5 μL water drop falling on it (Figure S3d). The surface is also repellent to a 20 μL water drop, which provides much higher pressure (~30.4 Pa) at the water/solid interface, right after being fully covered with water and then tilted to allow water to flow away (Figure S3e). Additionally, the

repeating re-entrant surface has been fully submerged in water at 0.25 cm, 1 cm, and 2 cm depth for 1 minute, and at 0.5 cm for 30 min, which introduce external pressure of 24.5 Pa to 196 Pa on the water/solid interface, and the WCA measurements with 5 μL drops were then conducted immediately after the membranes were tilted (Figure S3f). The surface remains superrepellent to the 5 μL water drops, indicating no water enters the repeating re-entrant structure and thus results in the Cassie-to-Wenzel transition. These experimental results demonstrate that the repeating re-entrant topography significantly enhances the desired hydrophobicity. Supposing the probability of a defect-free pillar for a single re-entrant structure is p (i.e., 0.950), the probability of a functional pillar after creating a second layer increases to $2p - p^2$ (i.e., 0.998). The inspiring findings are important to many potential applications, e.g., on-demand separation of liquid mixtures, antibiofouling surfaces, self-cleaning surfaces, etc.

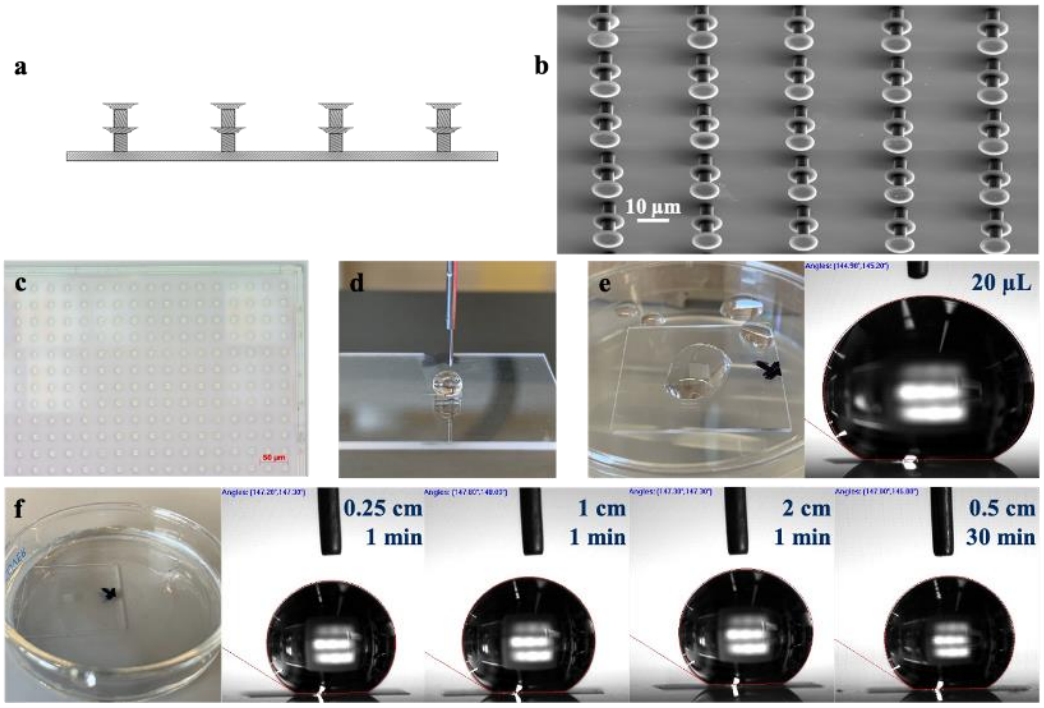

Appendix Figure 3. Repeating re-entrant topography inducing more robust surface wettability. (a) Cross-section view of the microscale repeating re-entrant structure. (b) Tilted SEM image of the repeating re-entrant surface. (c) Optical microscope image of the top view of the repeating re-entrant surface. (d) The repeating re-entrant surface repelling a 5 µL water drop. (e) A repeating re-entrant surface fully covered with water immediately followed by WCA measurement with a 20 µL drop on the post-rinsing surface. (f) A repeating re-entrant surface submerged in water at 0.25 cm, 1 cm, and 2 cm deep for 1 minute, and at 0.5 cm deep for 30 min, immediately followed by WCA measurements with 5 µL drops.

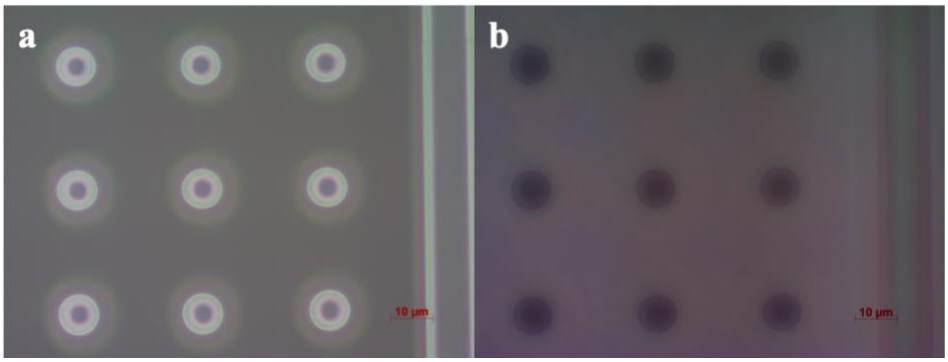

Appendix Figure 4. Optical microscope images of the repeating re-entrant surface. (a) Top layer. (b) Bottom layer.

Appendix A.3.4 On-Demand Separation by the Repeating Re-Entrant Membrane

The state-of-the-art membrane separation techniques include the size-dependent filtration and osmosis[173], and superwetting coatings[174, 175]. 3D printing is an emerging technique of fabricating separation membranes in recent years because of the ability to accurately produce complicated structures in a one-step process. However, many previous works are limited to printing relatively large-scale meshes with coatings to achieve the desired roughness and wettability[176-178]. Here, we fabricate a novel microscale repeating re-entrant separation membrane via 2PP 3D printing. Given two liquids, the re-entrant topography can be tuned to achieve wetting of one and dewetting of the other. Accordingly, on-demand separation of immiscible liquids L1/L2 can be achieved using a 3D-printed membrane with microscopic re-entrant topography. Figure S5a shows the separation membrane that allows L1 to flow through the re-entrant pores whereas renders L2 to stay on the surface when $\theta_{LS1} < \theta_{Re-entrant} < \theta_{LS2}$. The designed membrane here (Figure S5b) has 8 repeating re-entrant layers to ensure the robustness of the on-demand

separation. Each layer has square pores with re-entrant topography, and $\theta_{Re-entrant}$ is designed as 45° (Figure S5c). At the re-entrant section of each square pore, the length at the top and bottom are 50 μm and 100 μm, respectively, as shown by the optical microscope images of the 3D-printed re-entrant membrane in Figure S5d. The re-entrant membrane is then fitted into a 3D-printed liquid container and sealed with fluoroelastomer (see Figure S6a). As shown in Figure S5e, efficient separations of several liquid mixtures have been demonstrated using the 45º repeating re-entrant membrane, including bromobenzene and water (θ_{LS}: 19.3º/71.0º), chlorobenzene and water (θ_{LS}: 19.6º/71.0º), and bromobenzene and ethylene glycol (θ_{LS}: 19.3º/52.6º). All three separations show high flux[179-181], i.e., 0.0382 $m^3 \cdot m^{-2} \cdot min^{-1}$ for bromobenzene/ water, 0.0465 $m^3 \cdot m^{-2} \cdot min^{-1}$ for chlorobenzene/ water, and 0.0502 $m^3 \cdot m^{-2} \cdot min^{-1}$ bromobenzene/ ethylene glycol. The re-entrant membrane can also separate partially miscible liquid mixtures, i.e., benzyl alcohol and water (θ_{LS}: 25.6º/71.0º), as displayed in Figure S6b. Compared to other 3D-printed separation membranes, the novel repeating re-entrant membrane can achieve more efficient and robust on-demand separation due to the precisely controlled pore geometry and multiple layers of re-entrant structure. It is noteworthy that no external energy is required for all the separations here in that the driving force is gravity. The on-demand separation enabled by the 3D-printed repeating re-entrant membranes is critical for the wastewater treatment in the chemical industry[182].

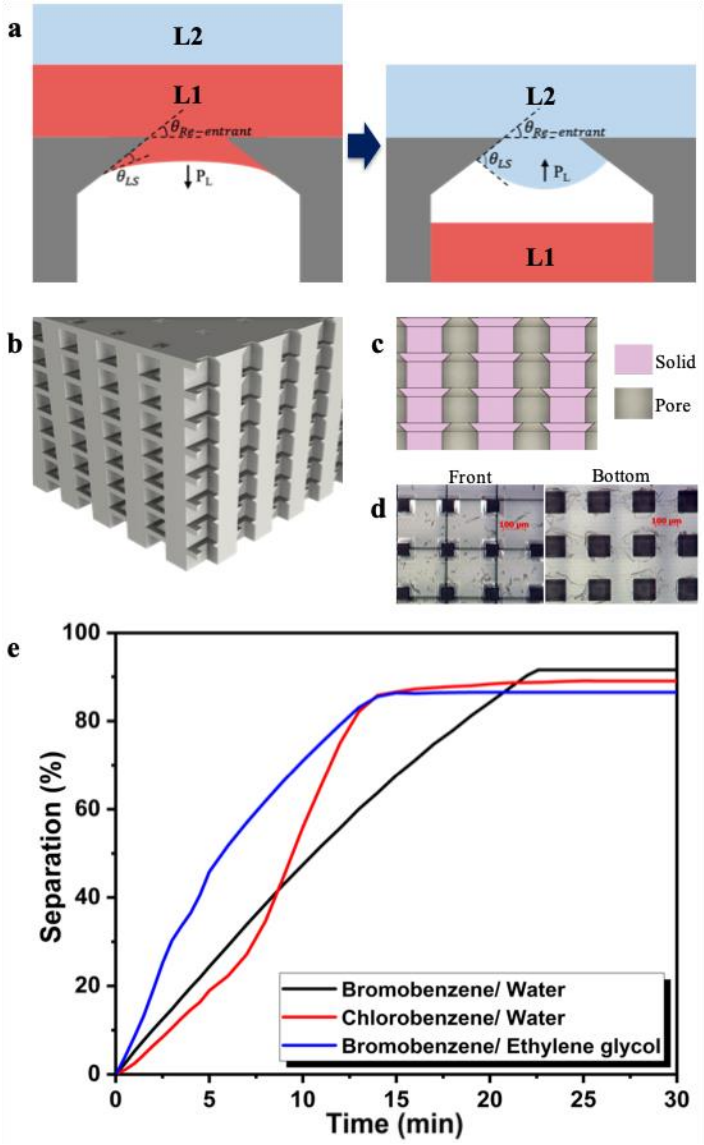

Appendix Figure 5. On-demand separation enabled by the re-entrant topography. (a) Separation of liquid mixture L1/L2 with the re-entrant membrane. (b) CAD image of the 3D cross-section view of the repeating re-entrant membrane. (c) 2D cross-section analysis of the repeating re-entrant membrane. (d) Optical microscope images of the front and bottom of the re-entrant membrane. (e) Separation of bromobenzene and water (θ_{LS}: 19.3º/71.0º), chlorobenzene and water (θ_{LS}: 19.6º/71.0º), and bromobenzene and ethylene glycol (θ_{LS}: 19.3º/52.6º) with the repeating re-entrant membrane ($\theta_{Re-entrant} = 45°$).

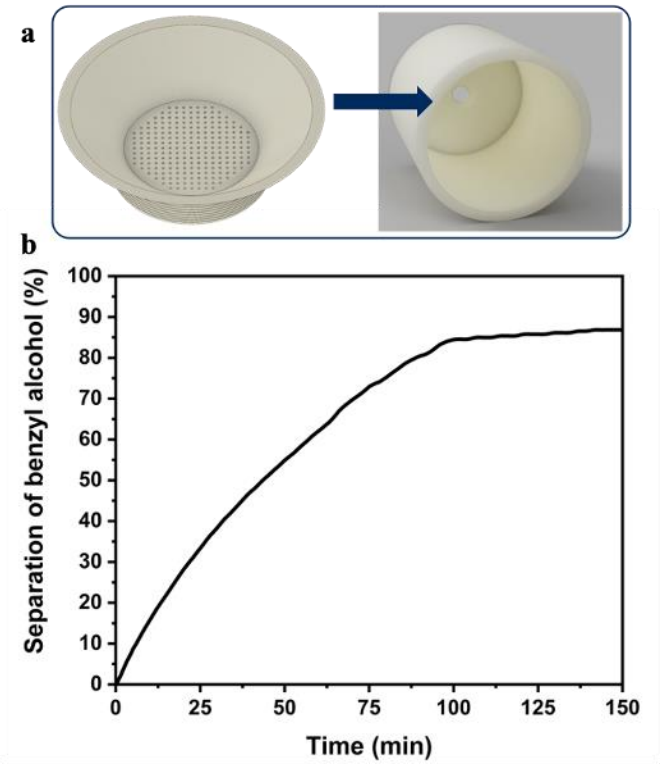

Appendix Figure 6. Separation of partially miscible liquid mixtures with the repeating re-entrant membrane. (a) Design of a 3D-printed repeating re-entrant separation membrane fitted into a 3D-printed liquid container. (b) Separation of partially miscible benzyl alcohol and DI water using the repeating re-entrant membrane.

Appendix A.4 Conclusions

In conclusion, we have developed a novel microscale repeating re-entrant surface topography that can be readily fabricated by 2PP 3D-printing. The fact that 2PP occurs at the laser focal spot guarantees the high resolution for the accurate fabrication of such fine structure. The

wettability of liquids with a wide range of surface tensions can be manipulated on-demand on the smart single re-entrant surface. The liquids with θ_{LS} smaller than $\theta_{Re-entrant}$ wet the re-entrant surface completely, while the liquids with θ_{LS} higher than $\theta_{Re-entrant}$ are fully repelled by the re-entrant surface. The 3D-printable microscopic repeating re-entrant surface, which is challenging to make by conventional techniques, has also been demonstrated to exhibit more robust on-demand wettability compared to the single re-entrant surface. Last but not least, we fabricated a separation membrane with microscopic repeating re-entrant pores by 2PP 3D-printing. We have achieved efficient on-demand separations of various liquid mixtures with high flux using the repeating re-entrant separation membrane. Our work provides insights into the on-demand manipulation of the surface wettability and the liquid separation using 2PP 3D-printing, which has great potential for applications in wetting, separation, and wastewater treatment.

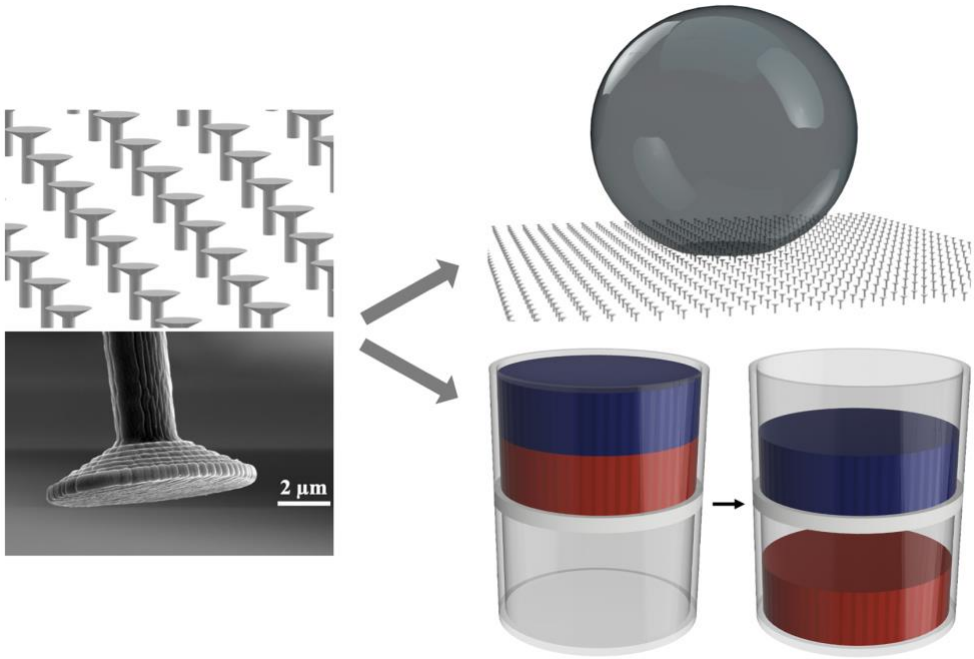

Appendix Figure 7. TOC figure.

Appendix B Uncovering the Underlying Mechanisms of the Fouling in Maleic Anhydride Condensers

The material in this chapter is based upon the published work *Ind. Eng. Chem. Res.* 2019, 58, 9, 3721–3725.

Appendix B.1 Introduction

Condenser fouling is usually referred to as the accumulation of the undesired solid deposits on the surface of the condenser.[183, 184] Clearly, the fouling, i.e., the accumulation of solid deposits, reduces the thermal transfer and flux of the condenser. Moreover, it significantly increases the operational costs of the condenser.[183, 184] For example, the costs resulting from additional fuel requirements and production losses associated with condenser fouling are estimated to be in the range of 0.4-2.2 Million (USD 2009) for thermoelectric power plants.[185] In practice, condenser fouling is a complicated process and the exact mechanism is dependent on the operation temperature, condensing material, condenser material and structure.[183, 184, 186] In terms of mechanisms, there are particulate fouling, precipitation fouling, chemical reaction fouling, corrosion fouling and biological fouling. [183, 184, 187-189] Understanding the governing mechanisms is critically important to developing the mitigating plan in real-life applications.

Maleic anhydride is an important raw material in many chemical reactions.[190-192] Very often, condensation is required to reflux maleic anhydride back to the reactor. Therefore, the fouling of the maleic anhydride condenser could be a serious issue. However, very little research

has been conducted to uncover the fouling mechanisms. For example, Lubrizol corporation has a continuing problem with fouling of maleic anhydride condensers on very large reactors. These reactors are used to make the largest volume material produced within Lubrizol. The condensers have 250 tubes that are 1 inch in diameter and 12 feet in length. Condensation of the maleic anhydride occurs inside the tubes. The state-of-the-art material of construction of the tubes is Monel for material compatibility reasons. The vapor feed to the condenser consists of maleic anhydride vapor containing trace amounts of water (ppm level), accompanied by a large amount of non-condensable gas. The system of interest to Lubrizol operates at an inlet vapor temperature of 200°C and a condensing media temperature of 100°C. Water content is approximately 100 ppm. The condensers are mounted vertically and the vapor feed is fed from the bottom in one instance and from the top in another. As shown in Figure S8, severe fouling occurs inside the tubes of the condensers after a short time, e.g., days to weeks, of operation, which imposes serious issues in the operation. Although the clogging of microreactors due to the photodimerization of maleic anhydride has been reported,[193] to date the fouling of the maleic anhydride condenser has not been reported and the underlying mechanisms remain unclear.

Appendix Figure 8. Severe fouling in the maleic anhydride condenser in Lubrizol.

In the current paper, we report our experimental efforts in: 1) uncovering the underlying mechanisms of the maleic anhydride condenser fouling and, 2) developing the strategy to combat

the fouling. We found that the condensed maleic anhydride, which is a liquid, reacts with the trace amounts of water to make maleic acid, which is a solid. This solid accumulates on the tube surface and, over a short period of time, i.e., days to weeks, will plug the tubes. The key enabler of the above-mentioned process is that the maleic anhydride droplets are pinned on the tube surface and do not roll off the surface. The pinning results from the high contact angle hysteresis, which can be attributed to the high surface roughness of the tube surface. After the surface roughness is reduced by machining, the maleic anhydride droplets roll off the tube surface much more easily, indicating this is a promising approach to reduce the condenser fouling.

Appendix B.2 Experimental Section

Appendix B.2.1 Materials

Monel 400, Duplex 2205, Hastelloy C-276, stainless steel 316 L and carbon steel (plain carbon) were purchased from a local metal shop and utilized as received. Three finishes were provided on the Monel samples that were tested. The first was simply 'as received'. The second was 'ground' which was simply a surface grinder. That is an abrasive material passed through a horizontal wheel. The result is a grain in a parallel direction to smooth the surface. The third was 'polished' using an end-mill or a fly-cutter device. The net result is circular surface effect which is more irregular than a 'ground' surface. All the surfaces of the metal samples were rinsed with ethanol and then dried under 13.3 Pa in a vacuum oven at 200 °C for 2 hours. The chemical compositions of the metal samples, which was determined by energy-dispersive X-ray (EDX) spectroscopy, is shown in Table S1.

Appendix Table 1. Chemical compositions of the alloys by energy-dispersive X-ray (EDX) spectroscopy (15kV accelerating voltage)

Wt%	Fe	Ni	Cr	Cu	Mo	Mn	C	O
Monel 400	2.04%	52.61%	0.04%	31.14%	5.65%	0.99%	11.17%	2.00%
Duplex 2205	52.24%	5.36%	16.08%	0%	2.65%	0.77%	16.88%	4.97%
Hastelloy C-276	5.48%	23.38%	26.46%	0%	5.65%	0%	5.6%	31.92%
Stainless steel 316L	55.25%	8%	14.16%	0%	1.62%	1.27%	15.71%	3.13%
Carbon steel	63.65%	0.09%	0.25%	0%	0%	0.52%	33.44%	1.71%

Appendix B.2.2 Modification of Surface Chemistry

To experimentally uncover the possible physical and chemical process at the interface between the condenser tube material and maleic anhydride under the same condition as during the condensation, we have built an in-situ characterization apparatus as shown in Figure S9. A temperature-controlling chamber and a heating syringe has been added on an AST VCA Optima contact angle testing system to mimic the condensation of maleic anhydride in the condenser. In this way, the maleic anhydride was heated to above the melting temperature (i.e., 52-55 °C),[194] and then loaded into the heating syringe and placed on the desired solid substrate, e.g., a Monel plate. This is all located inside the temperature-controlling chamber and preheated to the desired temperature. The heated interface was imaged with a CCD camera in situ. To measure the roll-off angle of a droplet on a tilted substrate, a tilting plate is placed beneath the apparatus. In this test,

A drop of maleic anhydride was deposited on the solid substrate at ~100°C and ambient humidity. The platform was tilted until the drop rolled off the surface and this tiling angle is recorded as the roll-off angle.

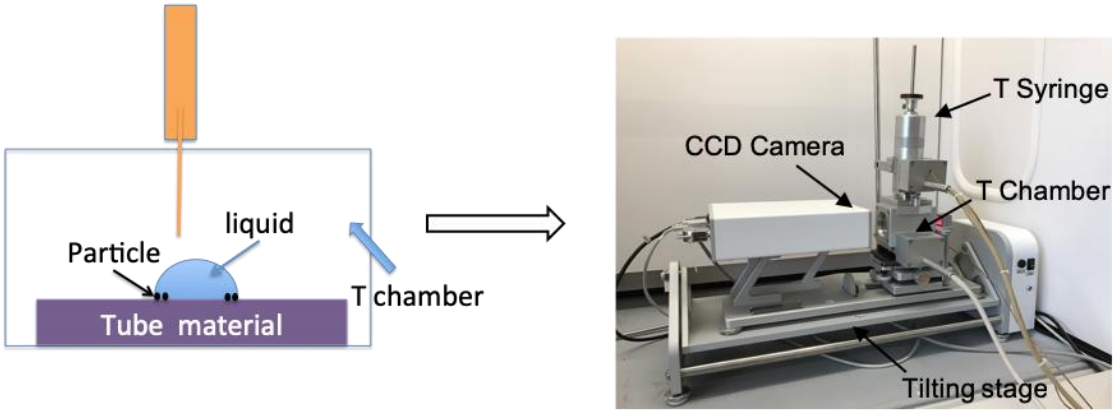

Appendix Figure 9. In-situ interface characterization apparatus.

The ^{1}H NMR spectrum was recorded on a Bruker Avance III 500 MHz spectrometer with a BBF/1H probe at 30°C. DMSO-d_6 was utilized as the NMR solvent. All chemical shifts were measured in parts per million (ppm) by frequency, and the solvent (i.e., DMSO-d_6) peak at 2.50 ppm[143] was used as the reference.

Optical microscopy was conducted using a Carl Zeiss Axio Lab A1 microscope with a Zeiss AxioCam ERc5s camera. The optical images of the metal surfaces were taken under 10x and 20x objectives.

Appendix B.3 Results and Discussions

Appendix B.3.1 Mechanisms of Fouling

Figure S10 shows the evolution of a drop of maleic acid on a stainless steel surface at 102 °C. The initial contact angle is ~70 °, After ~ 1 min, significant evaporation occurs and the contact angle decreases. It is noteworthy that the contact line is pinned and the diameter of the drop does not change. Interestingly, in ~ 3 mins, the liquid drop completely disappears and solid particles are formed. Indeed, similar solidification processes were observed on glass, Teflon and Monel, indicating this behavior, i.e., the liquid maleic anhydride droplet becomes the solid particle, is independent of the substrate materials.

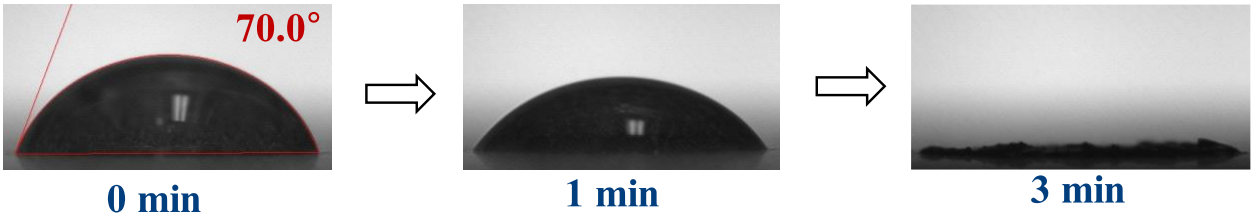

Appendix Figure 10. Evolution of the maleic anhydride-stainless steel interface at 102 °C.

To uncover the chemical structure of the solid particles formed, the ^{1}H NMR spectra was taken on the solid particles dissolved in DMSO-d_6 solvent. As shown in Figure S11, the NMR spectra is dominated by the peak (~ 6.27 ppm) corresponding to -CH=CH- in maleic acid[195]. Two tiny peaks, located at ~ 6.63 ppm and ~7.45 ppm, are also detected, and they are attributed to -CH=CH- in fumaric acid and unreacted maleic anhydride respectively[195, 196]. The NMR results

indicate that the solid particle is mainly maleic acid, whose melting temperature is ~134-138 °C[194]. As a result, the droplet becomes solid at ~ 102 °C.

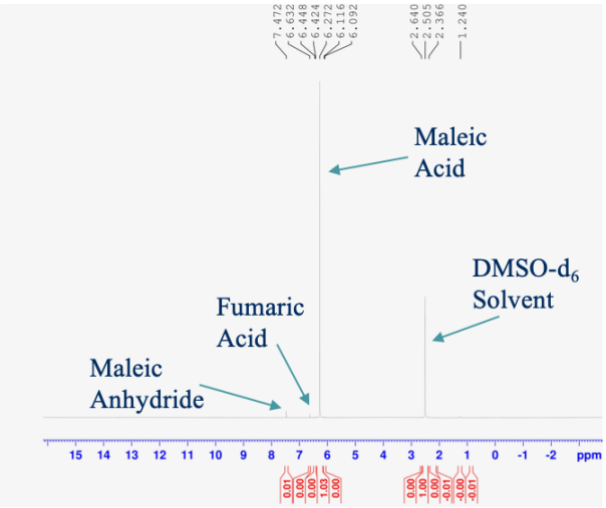

Appendix Figure 11. ^{1}H NMR spectra of the solid particles (as shown in Figure S8) dissolved in DMSO-d$_6$.

To further confirm that the solid particles are maleic acid, the particles were reheated. As shown in Figure S12, the solid particles melt at ~ 133 °C, which is very close to the melting point of maleic acid. Since the melting temperature of fumaric acid is ~ 287 °C (decomposition),[194] this result further supports the conclusion that the solid particle formed is mainly maleic acid.

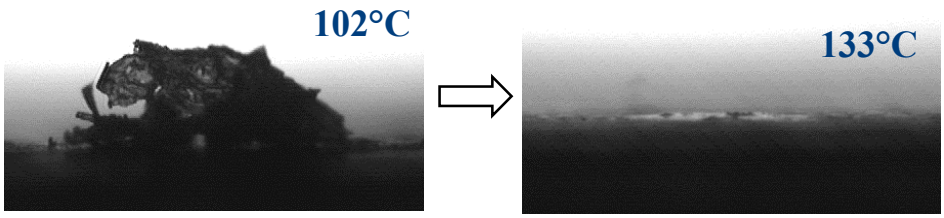

Appendix Figure 12. The melting of the solid particles from Figure S8.

The proposed reaction scheme to form maleic acid is shown in Figure S13. It is known that maleic anhydride reacts with water to form either maleic acid or fumaric acid.[197] Previous study showed that mild hydrolysis of maleic anhydride favors maleic acid rather than fumaric acid structure. In our experiment, the heating chamber has ambient atmosphere and, therefore, contains moisture. As a result, maleic anhydride reacts with the water and produces maleic acid, which are solid particles.

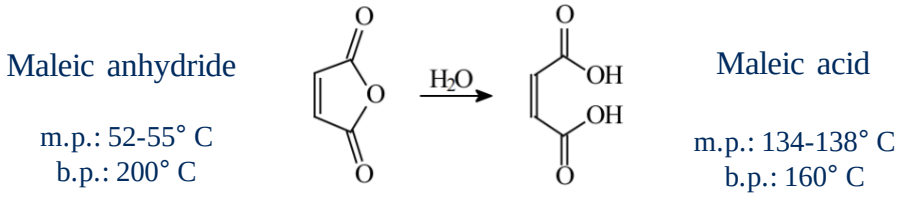

Appendix Figure 13. Possible reaction scheme to form maleic acid.

Based on the above discussion, the fouling mechanism of maleic anhydride condenser is schematically shown in Figure S14. First, maleic anhydride is condensed on the condenser surface and forms droplets, which are pinned on the surface and do not roll off the surface. Then the maleic anhydride droplet reacts with the water to form maleic acid, which is solid at the operation temperature. The maleic acid solid particles are deposited on the condenser surface. When the above-mentioned steps repeat again and again, more and more maleic acid particles accumulate in the condenser. Eventually, as shown in Figure S8, the condenser is completely clogged. It is noteworthy that, with longer reaction time and/or higher reaction temperature, it is possible to form fumaric acid, which is also solid under operation temperature and thus contributes to the fouling.

Since it is extremely difficult to completely remove the water from the condenser, the fouling and clogging of the maleic anhydride pose serious challenge to the operation of the chemical plant.

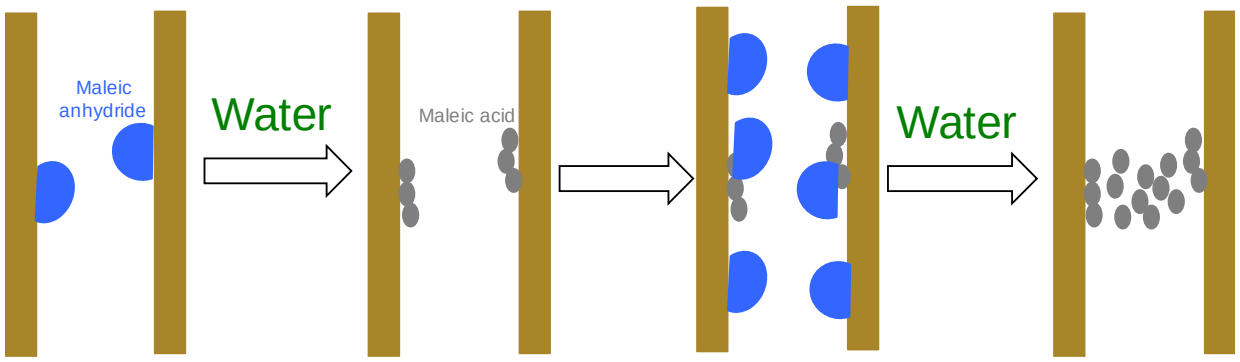

Appendix Figure 14. Proposed fouling mechanism of maleic anhydride condenser.

Appendix B.3.2 Surface Engineering

B.3.2.1 Pinning of the Droplet

As illustrated in Figure S11, if our proposed mechanism is true, one of the key enablers of the condenser fouling is that the maleic acid droplet is pinned on the condenser surface. If the droplet rolls off the surface easily, the fouling will be significantly reduced. This idea is supported by the results of the tilting experiment. As shown in Figure S15, for all four metal samples, the maleic anhydride droplet does not roll off the metal surface even at a tilting angle of 88°, which is the upper limit of the instrument and nearly vertical. The result indicates that, in real-life condensing process, the maleic anhydride droplets will not roll off the surface of the vertical tube. Instead, the droplets react with the water and initiate the fouling process.

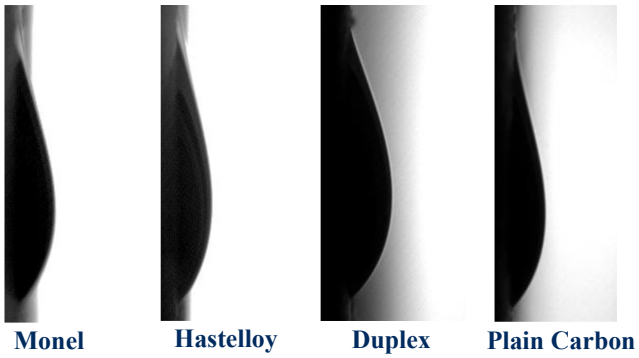

Appendix Figure 15. No roll-off of the maleic anhydride droplet at 88° tilting angle (100 °C).

The roll-off of a droplet on a tilt surface can be rationalized with a dynamic contact angle model as illustrated in Figure S16. Based on the force balance of a droplet on a tilted plane, the condition of the drop to be pinned can be given by the equation[198] shown in Figure S16.

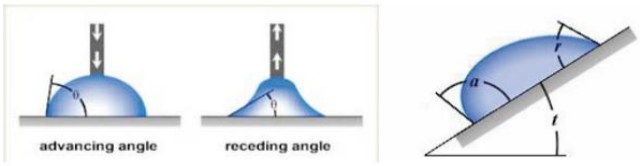

$$\rho r g(\cos\theta_r - \cos\theta_a)^3 \; r \; V g \sin t$$

Appendix Figure 16. Effect of dynamic contact angles on the roll-off angle.

Here r is the radius of the contact line, θ_a, θ_r and α is the advancing, receding and tilt angle, respectively. γ, ρ and V are the surface tension, density and volume of the drop, and g is the gravity acceleration. The drop is pinned on the tilted plane as long as the surface force exceeds the gravity force. When the difference between the advancing and the receding angle, which is often referred to as the contact angle hysteresis ($\theta_H = \theta_a - \theta_r$), is large, the surface force is large. As a result, the drop is pinned and will not roll off the tilted plane. Though the exact mechanism is still under

debate, it is generally accepted that the contact angle hysteresis is due to surface roughness and chemical heterogeneity.[199-203] For an ideally smooth and chemically homogeneous surface, the contact angle hysteresis is expected to be zero. Therefore, surface roughness is a key parameter to the roll-off of the maleic anhydride droplet and thus to the fouling of maleic anhydride condenser.

B.3.2.2 Effect of Surface Roughness

The surface topography of Monel with different finishes was characterized with optical microscope. Monel was primarily investigated since it is the state-of-the-art condenser material. The optical microscope images are shown in Figure S17. As-received Monel shows a very rough and heterogeneous feature. In contrast, ground, polished and machined Monel are much smoother and more homogeneous.

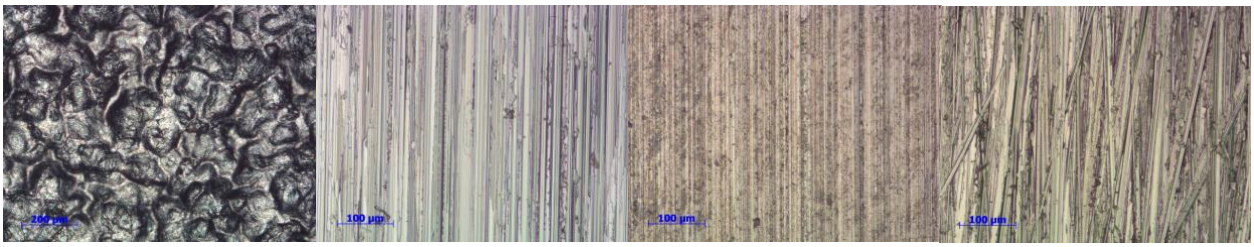

Appendix Figure 17. Optical microscope images of as-received, polished, ground, and machined Monel.

Appendix Table 2. Roll-off angles of maleic anhydride drops on Monel with different surface textures

Humidity	Sample	Initial Contact Angle	Roll-off angle
59%	As received	38.5°	Never moved (88° max)
50%	Ground	35.6°	51°
50%	Polished	41.5°	50°
50%	Machined	34.0°	38°

The roll-off angle results on Monel with different finishes, i.e., as-received, polished, ground, and machined, are shown in Table S2. For as-received Monel, maleic anhydride droplets never moved, even when tilted to a maximum of 88°, as shown previously in Figure S15. Droplets can therefore react with water to form solid maleic acid on the surface in the vertical position. Textured Monel samples prepared by grinding, machining and polishing were also tested. The difference in roll-off angle was drastic. Instead of remaining on the surface at 88° tilting angle, maleic anhydride droplets on textured Monel consistently moved at roll-off angles ranging from 38-51°. These droplets would not stick to the surface in the vertical position. The difference in roll-off angle can be attributed to different surface roughness. While the as-received Monel is highly heterogeneous, the difference between advancing and receding contact angle is large. As a result, the droplet is pinned. After texturing, e.g., grinding and machining, the surface is more homogeneous and the difference between the advancing and receding contact angle is smaller. Therefore, the droplet is not pinned anymore and rolls off the surface.

Tilting experiments were also carried out on textured Duplex and stainless steel. The results were similar to Monel in that texturing always caused drops to roll off at relatively low tilt angles,

whereas drops stuck to the non-textured metals. These results indicate that surface texturing is effective to reduce the pinning of the maleic anhydride droplet on the condenser surface. Therefore, surface texturing is a promising approach to reduce the fouling of the maleic anhydride condenser.

Appendix B.4 Conclusions

In this paper, we have uncovered the governing mechanisms of the fouling in maleic anhydride condensers and developed a promising strategy to combat the condenser fouling. Our in-situ interface characterization result showed that, in contact with moisture, maleic anhydride droplets become solid particles. ^{1}H NMR and reheating experimental results indicated that the solid particles are maleic acids. Based on these results, we have proposed that the fouling of the maleic anhydride condenser has the following mechanisms: First, maleic anhydride is condensed on the condenser surface and forms droplets, which are pinned on the surface and do not roll off the surface. Then the maleic anhydride droplet reacts with the water to form maleic acid, which is solid at the operation temperature and deposited on the condenser surface. When the above-mentioned steps repeat again and again, more and more maleic acid particles accumulate in the condenser, resulting in the fouling. We also found that, after the surface roughness of the condenser metal is reduced by machining, the maleic anhydride droplets roll off the tube surface much more easily, indicating that this is a promising approach to reduce the condenser fouling.

Bibliography

1. Lei, Z.; Chen, B.; Koo, Y.-M.; MacFarlane, D. R., Introduction: ionic liquids. *Chemical Reviews* **2017,** *117* (10), 6633-6635.

2. Zhang, S.; Zhang, J.; Zhang, Y.; Deng, Y., Nanoconfined ionic liquids. *Chemical Reviews* **2017,** *117* (10), 6755-6833.

3. Hayes, R.; Warr, G. G.; Atkin, R., Structure and nanostructure in ionic liquids. *Chemical reviews* **2015,** *115* (13), 6357-6426.

4. Plechkova, N. V.; Seddon, K. R., Applications of ionic liquids in the chemical industry. *Chem Soc Rev* **2008,** *37* (1), 123-150.

5. Lozano, L.; Godínez, C.; De Los Rios, A.; Hernández-Fernández, F.; Sánchez-Segado, S.; Alguacil, F. J., Recent advances in supported ionic liquid membrane technology. *Journal of Membrane Science* **2011,** *376* (1-2), 1-14.

6. Welton, T., Room-temperature ionic liquids. Solvents for synthesis and catalysis. *Chemical reviews* **1999,** *99* (8), 2071-2084.

7. Hallett, J. P.; Welton, T., Room-temperature ionic liquids: solvents for synthesis and catalysis. 2. *Chemical reviews* **2011,** *111* (5), 3508-3576.

8. Liu, L.; Wang, J.; Xu, X.; Wang, B., Supramolecular capsules of cucurbit [6] uril and controlled release. *Journal of Inclusion Phenomena and Macrocyclic Chemistry* **2014,** *80* (3-4), 437-441.

9. Watanabe, M.; Thomas, M. L.; Zhang, S.; Ueno, K.; Yasuda, T.; Dokko, K., Application of ionic liquids to energy storage and conversion materials and devices. *Chemical reviews* **2017,** *117* (10), 7190-7239.

10. Jónsson, E., Ionic liquids as electrolytes for energy storage applications–A modelling perspective. *Energy Storage Materials* **2020,** *25*, 827-835.

11. Gong, X.; West, B.; Taylor, A.; Li, L., Study on Nanometer-Thick Room-Temperature Ionic Liquids (RTILs) for Application as the Media Lubricant in Heat-Assisted Magnetic Recording (HAMR). *Industrial & Engineering Chemistry Research* **2016,** *55* (22), 6391-6397.

12. Zhou, F.; Liang, Y.; Liu, W., Ionic liquid lubricants: designed chemistry for engineering applications. *Chemical Society Reviews* **2009,** *38* (9), 2590-2599.

13. Wang, B.; Moran, C.; Lin, D.; Tang, H.; Gage, E.; Li, L., Nanometer-Thick Fluorinated Ionic Liquid Films as Lubricants in Data-Storage Devices. *ACS Applied Nano Materials* **2019,** *2* (8), 5260-5265.

14. Wang, B.; Moran, C.; Tang, H.; Li, L., Highly Fluorinated Ionic Liquid Films as Nanometer-Thick Media Lubricants for Hard Disk Drives. *ACS Applied Nano Materials* **2020,** *3* (9), 8803-8809.

15. Lertola, A. C.; Wang, B.; Li, L., Understanding the Friction of Nanometer-Thick Fluorinated Ionic Liquids. *Industrial & Engineering Chemistry Research* **2018,** *57* (34), 11681-11685.

16. Zhang, X.; Zhang, X.; Dong, H.; Zhao, Z.; Zhang, S.; Huang, Y., Carbon capture with ionic liquids: overview and progress. *Energy & Environmental Science* **2012,** *5* (5), 6668-6681.

17. Bates, E. D.; Mayton, R. D.; Ntai, I.; Davis, J. H., CO2 capture by a task-specific ionic liquid. *Journal of the American Chemical Society* **2002,** *124* (6), 926-927.

18. Zhang, Q.; Zhang, S.; Deng, Y., Recent advances in ionic liquid catalysis. *Green Chemistry* **2011,** *13* (10), 2619-2637.

19. Pârvulescu, V. I.; Hardacre, C., Catalysis in ionic liquids. *Chemical Reviews* **2007,** *107* (6), 2615-2665.

20. Atkin, R.; Warr, G. G., Structure in confined room-temperature ionic liquids. *The Journal of Physical Chemistry C* **2007,** *111* (13), 5162-5168.

21. Bovio, S.; Podesta, A.; Lenardi, C.; Milani, P., Evidence of Extended Solidlike Layering in [Bmim][NTf2] Ionic Liquid Thin Films at Room-Temperature. *J. Phys. Chem. B* **2009,** *113* (19), 6600-6603.

22. Liu, Y. D.; Zhang, Y.; Wu, G. Z.; Hu, J., Coexistence of liquid and solid phases of Bmim-PF6 ionic liquid on mica surfaces at room temperature. *J. Am. Chem. Soc.* **2006,** *128* (23), 7456-7457.

23. Yokota, Y.; Harada, T.; Fukui, K. I., Direct observation of layered structures at ionic liquid/solid interfaces by using frequency-modulation atomic force microscopy. *Chem. Commun.* **2010,** *46* (45), 8627-8629.

24. Payal, R. S.; Balasubramanian, S., Effect of cation symmetry on the organization of ionic liquids near a charged mica surface. *J. Phys.-Condens. Mat.* **2014,** *26* (28).

25. Perkin, S.; Albrecht, T.; Klein, J., Layering and shear properties of an ionic liquid, 1-ethyl-3-methylimidazolium ethylsulfate, confined to nano-films between mica surfaces. *Physical chemistry chemical physics* **2010,** *12* (6), 1243-1247.

26. Perkin, S.; Crowhurst, L.; Niedermeyer, H.; Welton, T.; Smith, A. M.; Gosvami, N. N., Self-assembly in the electrical double layer of ionic liquids. *Chemical Communications* **2011,** *47* (23), 6572-6574.

27. Perkin, S., Ionic liquids in confined geometries. *Physical Chemistry Chemical Physics* **2012,** *14* (15), 5052-5062.

28. Smith, A. M.; Lovelock, K. R.; Perkin, S., Monolayer and bilayer structures in ionic liquids and their mixtures confined to nano-films. *Faraday discussions* **2013,** *167*, 279-292.

29. Bovio, S.; Podesta, A.; Lenardi, C.; Milani, P., Evidence of extended solidlike layering in [Bmim][NTf2] ionic liquid thin films at room-temperature. *The journal of physical chemistry B* **2009,** *113* (19), 6600-6603.

30. Yokota, Y.; Harada, T.; Fukui, K.-i., Direct observation of layered structures at ionic liquid/solid interfaces by using frequency-modulation atomic force microscopy. *Chemical communications* **2010,** *46* (45), 8627-8629.

31. Deyko, A.; Cremer, T.; Rietzler, F.; Perkin, S.; Crowhurst, L.; Welton, T.; Steinruck, H. P.; Maier, F., Interfacial Behavior of Thin Ionic Liquid Films on Mica. *J. Phys. Chem. C* **2013,** *117* (10), 5101-5111.

32. Liu, Y.; Zhang, Y.; Wu, G.; Hu, J., Coexistence of liquid and solid phases of Bmim-PF6 ionic liquid on mica surfaces at room temperature. *Journal of the American Chemical Society* **2006,** *128* (23), 7456-7457.

33. Butt, H.-J.; Graf, K.; Kappl, M., *Physics and chemistry of interfaces*. John Wiley & Sons: 2013.

34. Bhushan, B., *Introduction to tribology*. John Wiley & Sons: 2013.

35. Palacio, M.; Bhushan, B., A review of ionic liquids for green molecular lubrication in nanotechnology. *Tribology Letters* **2010,** *40* (2), 247-268.

36. Bhushan, B., Nanotribology and nanomechanics of MEMS/NEMS and BioMEMS/BioNEMS materials and devices. *Microelectronic Engineering* **2007,** *84* (3), 387-412.

37. Gong, X.; Li, L., Nanometer-Thick Ionic Liquids as Boundary Lubricants. *Advanced Engineering Materials* **2018,** *20* (5), 1700617.

38. Waltman, R.; Khurshudov, A.; Tyndall, G., Autophobic dewetting of perfluoropolyether films on amorphous-nitrogenated carbon surfaces. *Tribology Letters* **2002,** *12* (3), 163-169.

39. Palacio, M.; Bhushan, B., Ultrathin wear-resistant ionic liquid films for novel MEMS/NEMS applications. *Advanced Materials* **2008,** *20* (6), 1194-1198.

40. Palacio, M.; Bhushan, B., Nanotribological and nanomechanical properties of lubricated PZT thin films for ferroelectric data storage applications. *Journal of Vacuum Science & Technology A: Vacuum, Surfaces, and Films* **2008,** *26* (4), 768-776.

41. Bhushan, B.; Palacio, M.; Kinzig, B., AFM-based nanotribological and electrical characterization of ultrathin wear-resistant ionic liquid films. *Journal of colloid and interface science* **2008,** *317* (1), 275-287.

42. Kondo, H.; Hatsuda, K.; Tano, N.; Ito, M.; Yun, K.; Watanabe, M., New Ionic Lubricants for Magnetic Thin-Film Media. *IEEE Transactions on Magnetics* **2014,** *50* (11), 1-4.

43. Hatsuda, K.; Tano, N.; Tani, H., Novel Ionic-Liquid-Type Lubricant for Heat-Assisted Magnetic Recording System. *IEEE Transactions on Magnetics* **2019,** *55* (9), 1-7.

44. Gong, X.; Wang, B.; Kozbial, A.; Li, L., From molecular arrangement to macroscopic wetting of ionic liquids on the mica surface: Effect of humidity. *Langmuir* **2018,** *34* (40), 12167-12173.

45. Deyko, A.; Lovelock, K. R. J.; Corfield, J. A.; Taylor, A. W.; Gooden, P. N.; Villar-Garcia, I. J.; Licence, P.; Jones, R. G.; Krasovskiy, V. G.; Chernikova, E. A.; Kustov, L. M., Measuring and predicting Delta H-vap(298) values of ionic liquids. *Phys Chem Chem Phys* **2009,** *11* (38), 8544-8555.

46. Gong, X.; Kozbial, A.; Rose, F.; Li, L., Effect of π–π+ Stacking on the Layering of Ionic Liquids Confined to an Amorphous Carbon Surface. *ACS applied materials & interfaces* **2015,** *7* (13), 7078-7081.

47. Mehnert, C. P.; Cook, R. A.; Dispenziere, N. C.; Afeworki, M., Supported ionic liquid catalysis - A new concept for homogeneous hydroformylation catalysis. *J Am Chem Soc* **2002,** *124* (44), 12932-12933.

48. Wang, Y. L.; Laaksonen, A., Interfacial structure and orientation of confined ionic liquids on charged quartz surfaces. *Phys. Chem. Chem. Phys.* **2014,** *16* (42), 23329-23339.

49. Li, H.; Wood, R. J.; Rutland, M. W.; Atkin, R., An ionic liquid lubricant enables superlubricity to be "switched on" in situ using an electrical potential. *Chemical Communications* **2014,** *50* (33), 4368-4370.

50. Sidhpuria, K. B.; Daniel-da-Silva, A. L.; Trindade, T.; Coutinho, J. A. P., Supported ionic liquid silica nanoparticles (SILnPs) as an efficient and recyclable heterogeneous catalyst for the dehydration of fructose to 5-hydroxymethylfurfural. *Green Chemistry* **2011,** *13* (2), 340-349.

51. Simon, P.; Gogotsi, Y., Capacitive energy storage in nanostructured carbon–electrolyte systems. *Accounts of chemical research* **2012,** *46* (5), 1094-1103.

52. Gebbie, M. A.; Valtiner, M.; Banquy, X.; Fox, E. T.; Henderson, W. A.; Israelachvili, J. N., Ionic liquids behave as dilute electrolyte solutions. *P Natl Acad Sci USA* **2013,** *110* (24), 9674-9679.

53. Perkin, S.; Salanne, M.; Madden, P.; Lynden-Bell, R., Is a Stern and diffuse layer model appropriate to ionic liquids at surfaces? *P Natl Acad Sci USA* **2013,** *110* (44), E4121-E4121.

54. Gong, X.; Kozbial, A.; Li, L., What Causes Extended Layering of Ionic liquids on the Mica Surface? *Chem. Sci.* **2015,** *6*, 3478-3482.

55. Gong, X.; Li, L., Understanding the wettability of nanometer-thick room temperature ionic liquids (RTILs) on solid surfaces. *Chinese Chemical Letters* **2017**.

56. Cheng, H. W.; Stock, P.; Moeremans, B.; Baimpos, T.; Banquy, X.; Renner, F. U.; Valtiner, M., Characterizing the Influence of Water on Charging and Layering at Electrified Ionic-Liquid/Solid Interfaces. *Advanced Materials Interfaces* **2015,** *2* (12).

57. Cheng, H. W.; Dienemann, J. N.; Stock, P.; Merola, C.; Chen, Y. J.; Valtiner, M., The Effect of Water and Confinement on Self-Assembly of Imidazolium Based Ionic Liquids at Mica Interfaces. *Scientific Reports* **2016,** *6*.

58. Barrosse-Antle, L. E.; Bond, A. M.; Compton, R. G.; O'Mahony, A. M.; Rogers, E. I.; Silvester, D. S., Voltammetry in Room Temperature Ionic Liquids: Comparisons and Contrasts with Conventional Electrochemical Solvents. *Chem. Asian J.* **2010,** *5* (2), 202-230.

59. Fedorov, M. V.; Kornyshev, A. A., Ionic liquids at electrified interfaces. *Chemical reviews* **2014,** *114* (5), 2978-3036.

60. Jiang, W.; Wang, Y.; Voth, G. A., Molecular dynamics simulation of nanostructural organization in ionic liquid/water mixtures. *The Journal of Physical Chemistry B* **2007,** *111* (18), 4812-4818.

61. Firestone, M. A.; Dzielawa, J. A.; Zapol, P.; Curtiss, L. A.; Seifert, S.; Dietz, M. L., Lyotropic liquid-crystalline gel formation in a room-temperature ionic liquid. *Langmuir* **2002,** *18* (20), 7258-7260.

62. Sakai, K.; Okada, K.; Uka, A.; Misono, T.; Endo, T.; Sasaki, S.; Abe, M.; Sakai, H., Effects of Water on Solvation Layers of Imidazolium-Type Room Temperature Ionic Liquids on Silica and Mica. *Langmuir* **2015,** *31* (22), 6085-6091.

63. Wang, Z. W.; Li, H.; Atkin, R.; Priest, C., Influence of Water on the Interfacial Nanostructure and Wetting of [Rmim][NTf2] Ionic Liquids at Mica Surfaces. *Langmuir* **2016**.

64. Jurado, L. A.; Kim, H.; Rossi, A.; Arcifa, A.; Schuh, J. K.; Spencer, N. D.; Leal, C.; Ewoldt, R. H.; Espinosa-Marzal, R. M., Effect of the environmental humidity on the bulk, interfacial and nanoconfined properties of an ionic liquid. *Physical Chemistry Chemical Physics* **2016,** *18* (32), 22719-22730.

65. McDonald, S.; Elbourne, A.; Warr, G. G.; Atkin, R., Metal ion adsorption at the ionic liquid–mica interface. *Nanoscale* **2016,** *8* (2), 906-914.

66. Wang, Z.; Shi, F.; Zhao, C., Humidity-accelerated spreading of ionic liquids on a mica surface. *RSC Advances* **2017,** *7* (68), 42718-42724.

67. Young, J. F., Humidity control in the laboratory using salt solutions—a review. *Journal of Applied Chemistry* **1967,** *17* (9), 241-245.

68. Cantrell, W.; Ewing, G. E., Thin film water on muscovite mica. *The Journal of Physical Chemistry B* **2001,** *105* (23), 5434-5439.

69. Beaglehole, D.; Christenson, H., Vapor adsorption on mica and silicon: entropy effects, layering, and surface forces. *The Journal of Physical Chemistry* **1992,** *96* (8), 3395-3403.

70. Balmer, T.; Christenson, H.; Spencer, N.; Heuberger, M., The effect of surface ions on water adsorption to mica. *Langmuir* **2008,** *24* (4), 1566-1569.

71. Voinov, O., Hydrodynamics of wetting. *Fluid dynamics* **1976,** *11* (5), 714-721.

72. Wang, Z.; Priest, C., Impact of nanoscale surface heterogeneity on precursor film growth and macroscopic spreading of [Rmim][NTf2] ionic liquids on mica. *Langmuir* **2013,** *29* (36), 11344-11353.

73. Cheng, T.; Sun, H., Adsorption of Ethanol Vapor on Mica Surface under Different Relative Humidities: A Molecular Simulation Study. *J. Phys. Chem. C* **2012,** *116* (31), 16436-16446.

74. Sakuma, H.; Kondo, T.; Nakao, H.; Shiraki, K.; Kawamura, K., Structure of Hydrated Sodium Ions and Water Molecules Adsorbed on the Mica/Water Interface. *J. Phys. Chem. C* **2011,** *115* (32), 15959-15964.

75. Pashley, R. M., Dlvo and Hydration Forces between Mica Surfaces in Li+,Na+,K+,and Cs+ Electrolyte-Solutions - a Correlation of Double-Layer and Hydration Forces with Surface Cation-Exchange Properties. *J Colloid Interf Sci* **1981,** *83* (2), 531-546.

76. Hu, J.; Ogletree, D.; Salmeron, M., The structure of molecularly thin films of water on mica in humid environments. *Surface science* **1995,** *344* (3), 221-236.

77. Xu, L.; Salmeron, M., An XPS and scanning polarization force microscopy study of the exchange and mobility of surface ions on mica. *Langmuir* **1998,** *14* (20), 5841-5844.

78. Hayes, R.; Warr, G. G.; Atkin, R., At the interface: solvation and designing ionic liquids. *Physical Chemistry Chemical Physics* **2010,** *12* (8), 1709-1723.

79. Cremer, T.; Wibmer, L.; Calderon, S. K.; Deyko, A.; Maier, F.; Steinruck, H. P., Interfaces of ionic liquids and transition metal surfaces-adsorption, growth, and thermal reactions of ultrathin [C(1)C(1)Im][Tf2N] films on metallic and oxidised Ni(111) surfaces. *Phys Chem Chem Phys* **2012,** *14* (15), 5153-5163.

80. Deyko, A.; Cremer, T.; Rietzler, F.; Perkin, S.; Crowhurst, L.; Welton, T.; Steinrück, H.-P.; Maier, F., Interfacial Behavior of Thin Ionic Liquid Films on Mica. *The Journal of Physical Chemistry C* **2013,** *117* (10), 5101-5111.

81. Cremer, T.; Killian, M.; Gottfried, J. M.; Paape, N.; Wasserscheid, P.; Maier, F.; Steinruck, H. P., Physical Vapor Deposition of [EMIM][Tf(2)N]: A New Approach to the Modification of Surface Properties with Ultrathin Ionic Liquid Films. *Chemphyschem* **2008,** *9* (15), 2185-2190.

82. Feng, G.; Jiang, X.; Qiao, R.; Kornyshev, A. A., Water in ionic liquids at electrified interfaces: The anatomy of electrosorption. *ACS nano* **2014,** *8* (11), 11685-11694.

83. Krossing, I.; Slattery, J. M.; Daguenet, C.; Dyson, P. J.; Oleinikova, A.; Weingärtner, H., Why are ionic liquids liquid? A simple explanation based on lattice and solvation energies. *Journal of the American Chemical Society* **2006,** *128* (41), 13427-13434.

84. Christenson, H. K.; Thomson, N. H., The nature of the air-cleaved mica surface. *Surface Science Reports* **2016,** *71* (2), 367-390.

85. Wang, Y.; Li, L., Uncovering the Underlying Mechanisms Governing the Solidlike Layering of Ionic Liquids (ILs) on Mica. *Langmuir* **2020,** *36* (11), 2743-2756.

86. Hu, J.; Xiao, X.-D.; Ogletree, D.; Salmeron, M., Imaging the condensation and evaporation of molecularly thin films of water with nanometer resolution. *Science* **1995,** *268* (5208), 267-269.

87. Wakeham, D.; Hayes, R.; Warr, G. G.; Atkin, R., Influence of temperature and molecular structure on ionic liquid solvation layers. *The Journal of Physical Chemistry B* **2009,** *113* (17), 5961-5966.

88. Merzlikine, A.; Li, L.; Jones, P. M.; Hsia, Y.-T., Lubricant layer formation during the dip-coating process: influence of adsorption and viscous flow mechanisms. *Tribology Letters* **2005,** *18* (3), 279-286.

89. Wang, Y.; Sun, J.; Li, L., What is the role of the interfacial interaction in the slow relaxation of nanometer-thick polymer melts on a solid surface? *Langmuir* **2012,** *28* (14), 6151-6156.

90. Wang, Y.-L.; Li, B.; Sarman, S.; Mocci, F.; Lu, Z.-Y.; Yuan, J.; Laaksonen, A.; Fayer, M. D., Microstructural and dynamical heterogeneities in ionic liquids. *Chemical reviews* **2020,** *120* (13), 5798-5877.

91. Gong, X.; Wang, B.; Li, L., Spreading of Nanodroplets of Ionic Liquids on the Mica Surface. *ACS omega* **2018,** *3* (12), 16398-16402.

92. Cremer, T.; Wibmer, L.; Calderón, S. K.; Deyko, A.; Maier, F.; Steinrück, H.-P., Interfaces of ionic liquids and transition metal surfaces—adsorption, growth, and thermal reactions of ultrathin [C 1 C 1 Im][Tf 2 N] films on metallic and oxidised Ni (111) surfaces. *Physical Chemistry Chemical Physics* **2012,** *14* (15), 5153-5163.

93. Součková, M.; Klomfar, J.; Pátek, J., Temperature dependence of the surface tension and 0.1 MPa density for 1-Cn-3-methylimidazolium tris (pentafluoroethyl) trifluorophosphate with n= 2, 4, and 6. *The Journal of Chemical Thermodynamics* **2012,** *48*, 267-275.

94. Liu, Q.-S.; Tong, J.; Tan, Z.-C.; Welz-Biermann, U.; Yang, J.-Z., Density and surface tension of ionic liquid [C2mim][PF3 (CF2CF3) 3] and prediction of properties [C n mim][PF3 (CF2CF3) 3](n= 1, 3, 4, 5, 6). *Journal of Chemical & Engineering Data* **2010,** *55* (7), 2586-2589.

95. Almeida, H. F.; Freire, M. G.; Fernandes, A. M.; Lopes-da-Silva, J. A.; Morgado, P.; Shimizu, K.; Filipe, E. J.; Canongia Lopes, J. N.; Santos, L. M.; Coutinho, J. o. A., Cation alkyl side chain length and symmetry effects on the surface tension of ionic liquids. *Langmuir* **2014,** *30* (22), 6408-6418.

96. Zhou, Z. B.; Matsumoto, H.; Tatsumi, K., Structure and properties of new ionic liquids based on alkyl-and alkenyltrifluoroborates. *ChemPhysChem* **2005,** *6* (7), 1324-1332.

97. Kolbeck, C.; Lehmann, J.; Lovelock, K.; Cremer, T.; Paape, N.; Wasserscheid, P.; Froba, A.; Maier, F.; Steinruck, H.-P., Density and surface tension of ionic liquids. *The Journal of Physical Chemistry B* **2010,** *114* (51), 17025-17036.

98. Pensado, A. S.; Gomes, M. F. C.; Lopes, J. N. C.; Malfreyt, P.; Pádua, A. A., Effect of alkyl chain length and hydroxyl group functionalization on the surface properties of imidazolium ionic liquids. *Physical Chemistry Chemical Physics* **2011,** *13* (30), 13518-13526.

99. Young, T., III. An essay on the cohesion of fluids. *Philosophical transactions of the royal society of London* **1805,** (95), 65-87.

100. Cheng, H.-W.; Dienemann, J.-N.; Stock, P.; Merola, C.; Chen, Y.-J.; Valtiner, M., The effect of water and confinement on self-assembly of imidazolium based ionic liquids at mica interfaces. *Scientific reports* **2016,** *6* (1), 1-9.

101. Li, H.; Endres, F.; Atkin, R., Effect of alkyl chain length and anion species on the interfacial nanostructure of ionic liquids at the Au (111)–ionic liquid interface as a function of potential. *Physical Chemistry Chemical Physics* **2013,** *15* (35), 14624-14633.

102. Li, H.; Wood, R. J.; Endres, F.; Atkin, R., Influence of alkyl chain length and anion species on ionic liquid structure at the graphite interface as a function of applied potential. *Journal of Physics: Condensed Matter* **2014,** *26* (28), 284115.

103. Zhang, F.; Fang, C.; Qiao, R., Effects of water on mica–ionic liquid interfaces. *The Journal of Physical Chemistry C* **2018,** *122* (16), 9035-9045.

104. Yokota, Y.; Miyamoto, H.; Imanishi, A.; Inagaki, K.; Morikawa, Y.; Fukui, K.-i., Structural and dynamic properties of 1-butyl-3-methylimidazolium bis (trifluoromethanesulfonyl) imide/mica and graphite interfaces revealed by molecular dynamics simulation. *Physical Chemistry Chemical Physics* **2018,** *20* (9), 6668-6676.

105. Kamalakannan, S.; Prakash, M.; Al-Mogren, M. M.; Chambaud, G.; Hochlaf, M., Alkyl methyl imidazolium-based ionic liquids at the Au (111) surface: anions and alkyl chain cations induced interfacial effects. *The Journal of Physical Chemistry C* **2019,** *123* (24), 15087-15098.

106. Watanabe, S.; Nakano, M.; Miyake, K.; Tsuboi, R.; Sasaki, S., Effect of molecular orientation angle of imidazolium ring on frictional properties of imidazolium-based ionic liquid. *Langmuir* **2014,** *30* (27), 8078-8084.

107. Tsuzuki, S.; Tokuda, H.; Hayamizu, K.; Watanabe, M., Magnitude and directionality of interaction in ion pairs of ionic liquids: Relationship with ionic conductivity. *The Journal of Physical Chemistry B* **2005,** *109* (34), 16474-16481.

108. Tsuzuki, S.; Tokuda, H.; Mikami, M., Theoretical analysis of the hydrogen bond of imidazolium C 2–H with anions. *Physical Chemistry Chemical Physics* **2007,** *9* (34), 4780-4784.

109. Tang, F.; Ohto, T.; Hasegawa, T.; Bonn, M.; Nagata, Y., π+–π+ stacking of imidazolium cations enhances molecular layering of room temperature ionic liquids at their interfaces. *Physical Chemistry Chemical Physics* **2017,** *19* (4), 2850-2856.

110. Sides, P. J.; Faruqui, D.; Gellman, A. J., Dynamics of charging of muscovite mica: measurement and modeling. *Langmuir* **2009,** *25* (3), 1475-1481.

111. Gebbie, M. A.; Smith, A. M.; Dobbs, H. A.; Warr, G. G.; Banquy, X.; Valtiner, M.; Rutland, M. W.; Israelachvili, J. N.; Perkin, S.; Atkin, R., Long range electrostatic forces in ionic liquids. *Chemical Communications* **2017,** *53* (7), 1214-1224.

112. Miranda, P.; Xu, L.; Shen, Y.; Salmeron, M., Icelike water monolayer adsorbed on mica at room temperature. *Physical review letters* **1998,** *81* (26), 5876.

113. Kryder, M. H.; Gage, E. C.; McDaniel, T. W.; Challener, W. A.; Rottmayer, R. E.; Ju, G.; Hsia, Y.-T.; Erden, M. F., Heat assisted magnetic recording. *Proceedings of the IEEE* **2008,** *96* (11), 1810-1835.

114. Marchon, B.; Olson, T., Magnetic spacing trends: from LMR to PMR and beyond. *IEEE Transactions on Magnetics* **2009,** *45* (10), 3608-3611.

115. Weller, D.; Parker, G.; Mosendz, O.; Champion, E.; Stipe, B.; Wang, X.; Klemmer, T.; Ju, G.; Ajan, A., A HAMR Media Technology Roadmap to an Areal Density of 4 Tb/in $^ 2$. *IEEE transactions on magnetics* **2013,** *50* (1), 1-8.

116. Marchon, B.; Pitchford, T.; Hsia, Y.-T.; Gangopadhyay, S., The head-disk interface roadmap to an areal density of Tbit/in2. *Advances in Tribology* **2013,** *2013*.

117. Guo, X.-C.; Knigge, B.; Marchon, B.; Waltman, R.; Carter, M.; Burns, J., Multidentate functionalized lubricant for ultralow head/disk spacing in a disk drive. *Journal of applied physics* **2006,** *100* (4), 044306.

118. Guo, X.-C.; Marchon, B.; Wang, R.-H.; Mate, C.; Dai, Q.; Waltman, R.; Deng, H.; Pocker, D.; Xiao, Q.-F.; Saito, Y., A multidentate lubricant for use in hard disk drives at sub-nanometer thickness. *Journal of Applied Physics* **2012,** *111* (2), 024503.

119. Waltman, R., Autophobic dewetting of Z-tetraol perfluoropolyether lubricant films on the amorphous nitrogenated carbon surface. *Langmuir* **2004,** *20* (8), 3166-3172.

120. Henck, S. A., Lubrication of digital micromirrordevices TM. *Tribology Letters* **1997,** *3* (3), 239-247.

121. Kim, H. I.; Mate, C. M.; Hannibal, K. A.; Perry, S. S., How disjoining pressure drives the dewetting of a polymer film on a silicon surface. *Physical review letters* **1999,** *82* (17), 3496.

122. Chen, H.; Li, L.; Merzlikine, A. G.; Hsia, Y.-T.; Jhon, M. S., Surface energy and adhesion of perfluoropolyether nanofilms on carbon overcoat: The end group and backbone chain effect. *Journal of applied physics* **2006,** *99* (8), 08N103.

123. Chen, H.; Guo, Q.; Jhon, M. S., Effects of molecular structure on the conformation and dynamics of perfluoropolyether nanofilms. *IEEE transactions on magnetics* **2007,** *43* (6), 2247-2249.

124. Cotts, P. M., Solution properties of a group of perfluoropolyethers: comparison of unperturbed dimensions. *Macromolecules* **1994,** *27* (22), 6487-6491.

125. Bhushan, B.; Kwak, K. J., Platinum-coated probes sliding at up to 100 mm s− 1 against coated silicon wafers for AFM probe-based recording technology. *Nanotechnology* **2007,** *18* (34), 345504.

126. Van Valkenburg, M. E.; Vaughn, R. L.; Williams, M.; Wilkes, J. S., Ionic liquids as thermal fluids. *ECS Proceedings Volumes* **2002,** *2002*, 112-123.

127. Gong, X.; Frankert, S.; Wang, Y.; Li, L., Thickness-dependent molecular arrangement and topography of ultrathin ionic liquid films on a silica surface. *Chemical Communications* **2013,** *49* (71), 7803-7805.

128. Gong, X.; Kozbial, A.; Li, L., What causes extended layering of ionic liquids on the mica surface? *Chemical Science* **2015,** *6* (6), 3478-3482.

129. Ma, J. C.; Dougherty, D. A., The cation− π interaction. *Chemical reviews* **1997,** *97* (5), 1303-1324.

130. Almantariotis, D.; Stevanovic, S.; Fandino, O.; Pensado, A.; Padua, A. A.; Coxam, J.-Y.; Costa Gomes, M., Absorption of Carbon Dioxide, Nitrous Oxide, Ethane and Nitrogen by 1-Alkyl-3-methylimidazolium (C n mim, n= 2, 4, 6) Tris (pentafluoroethyl) trifluorophosphate Ionic Liquids (eFAP). *The Journal of Physical Chemistry B* **2012,** *116* (26), 7728-7738.

131. Kato, T.; Kawaguchi, M., Durability of perfluoropolyether nanolubricant film fixed on diamond-like carbon surfaces. In *Tribology and Interface Engineering Series*, Elsevier: 2005; Vol. 48, pp 207-212.

132. Zhao, Z.; Karazic, E.; Zhao, Q.; Embree, M.; Trinh, P.; Lam, T., Lubricant bonding, chemical structure, and additive effects on tribological performances at head–disk interfaces. *Microsystem Technologies* **2002,** *9* (1-2), 48-54.

133. Gao, C.; Lee, Y.; Chao, J.; Russak, M., Dip-coating of ultra-thin liquid lubricant and its control for thin-film magnetic hard disks. *IEEE Transactions on Magnetics* **1995,** *31* (6), 2982-2984.

134. Fukushima, T.; Kosaka, A.; Ishimura, Y.; Yamamoto, T.; Takigawa, T.; Ishii, N.; Aida, T., Molecular ordering of organic molten salts triggered by single-walled carbon nanotubes. *Science* **2003,** *300* (5628), 2072-2074.

135. Biresaw, G.; Mittal, K. L., *Surfactants in Tribology, 2 Volume Set*. CRC Press: 2011.

136. Zhao, W.; Wang, Y.; Wang, L.; Bai, M.; Xue, Q., Influence of heat treatment on the micro/nano-tribological properties of ultra-thin ionic liquid films on silicon. *Colloids and Surfaces A: Physicochemical and Engineering Aspects* **2010,** *361* (1-3), 118-125.

137. Zhu, M.; Yan, J.; Mo, Y.; Bai, M., Effect of the anion on the tribological properties of ionic liquid nano-films on surface-modified silicon wafers. *Tribology Letters* **2008,** *29* (3), 177-183.

138. Hollóczki, O.; Macchiagodena, M.; Weber, H.; Thomas, M.; Brehm, M.; Stark, A.; Russina, O.; Triolo, A.; Kirchner, B., Triphilic ionic-liquid mixtures: fluorinated and non-fluorinated aprotic ionic-liquid mixtures. *ChemPhysChem* **2015,** *16* (15), 3325.

139. Lo Celso, F.; Appetecchi, G. B.; Simonetti, E.; Zhao, M.; Castner Jr, E. W.; Keiderling, U.; Gontrani, L.; Triolo, A.; Russina, O., Microscopic structural and dynamic features in triphilic room temperature ionic liquids. *Frontiers in chemistry* **2019,** *7*, 285.

140. Hettige, J. J.; Araque, J. C.; Margulis, C. J., Bicontinuity and multiple length scale ordering in triphilic hydrogen-bonding ionic liquids. *The Journal of Physical Chemistry B* **2014,** *118* (44), 12706-12716.

141. Jones, P. M.; Yan, X.; Li, L.; Kiely, J. D.; Platt, C. L.; Stirniman, M. J.; Yang, J.; Hsia, Y.-T., Covalently bound monolayer for a protective carbon overcoat. Google Patents: 2015.

142. Yeo, R. J., *Ultrathin carbon-based overcoats for extremely high density magnetic recording*. Springer: 2017.

143. Gottlieb, H. E.; Kotlyar, V.; Nudelman, A., NMR chemical shifts of common laboratory solvents as trace impurities. *The Journal of organic chemistry* **1997,** *62* (21), 7512-7515.

144. Bhushan, B., *Springer handbook of nanotechnology*. Springer: 2017.

145. Li, L.; Wang, Y.; Gallaschun, C.; Risch, T.; Sun, J., Why can a nanometer-thick polymer coated surface be more wettable to water than to oil? *Journal of Materials Chemistry* **2012,** *22* (33), 16719-16722.

146. Kreder, M. J.; Daniel, D.; Tetreault, A.; Cao, Z.; Lemaire, B.; Timonen, J. V.; Aizenberg, J., Film dynamics and lubricant depletion by droplets moving on lubricated surfaces. *Physical Review X* **2018,** *8* (3), 031053.

147. Wang, Y.; Knapp, J.; Legere, A.; Raney, J.; Li, L., Effect of end-groups on simultaneous oleophobicity/hydrophilicity and anti-fogging performance of nanometer-thick perfluoropolyethers (PFPEs). *Rsc Advances* **2015,** *5* (39), 30570-30576.

148. Cassie, A., Contact angles. *Discussions of the Faraday society* **1948,** *3*, 11-16.

149. Bhushan, B.; Israelachvili, J. N.; Landman, U., Nanotribology: friction, wear and lubrication at the atomic scale. *Nature* **1995,** *374* (6523), 607-616.

150. Mate, C. M.; Carpick, R. W., *Tribology on the Small Scale: A Modern Textbook on Friction, Lubrication, and Wear*. Oxford University Press, USA: 2019.

151. Barthlott, W.; Neinhuis, C., Purity of the sacred lotus, or escape from contamination in biological surfaces. *Planta* **1997,** *202* (1), 1-8.

152. Liu, Y.; Li, G., A new method for producing "Lotus Effect" on a biomimetic shark skin. *Journal of colloid and interface science* **2012,** *388* (1), 235-242.

153. Gao, X.; Jiang, L., Water-repellent legs of water striders. *Nature* **2004,** *432* (7013), 36-36.

154. Kreder, M. J.; Alvarenga, J.; Kim, P.; Aizenberg, J., Design of anti-icing surfaces: smooth, textured or slippery? *Nature Reviews Materials* **2016,** *1* (1), 1-15.

155. Bellanger, H.; Darmanin, T.; Taffin de Givenchy, E.; Guittard, F., Chemical and physical pathways for the preparation of superoleophobic surfaces and related wetting theories. *Chemical reviews* **2014,** *114* (5), 2694-2716.

156. Cassie, A.; Baxter, S., Wettability of porous surfaces. *Transactions of the Faraday society* **1944,** *40*, 546-551.

157. Truby, R. L.; Lewis, J. A., Printing soft matter in three dimensions. *Nature* **2016,** *540* (7633), 371-378.

158. Zhang, Y.; Zhang, F.; Yan, Z.; Ma, Q.; Li, X.; Huang, Y.; Rogers, J. A., Printing, folding and assembly methods for forming 3D mesostructures in advanced materials. *Nature Reviews Materials* **2017,** *2* (4), 1-17.

159. Yang, Y.; Li, X.; Zheng, X.; Chen, Z.; Zhou, Q.; Chen, Y., 3D-printed biomimetic super-hydrophobic structure for microdroplet manipulation and oil/water separation. *Advanced materials* **2018,** *30* (9), 1704912.

160. Liu, X.; Gu, H.; Wang, M.; Du, X.; Gao, B.; Elbaz, A.; Sun, L.; Liao, J.; Xiao, P.; Gu, Z., 3D printing of bioinspired liquid superrepellent structures. *Advanced Materials* **2018,** *30* (22), 1800103.

161. Li, Y.; Mao, H.; Hu, P.; Hermes, M.; Lim, H.; Yoon, J.; Luhar, M.; Chen, Y.; Wu, W., Bioinspired functional surfaces enabled by multiscale stereolithography. *Advanced Materials Technologies* **2019,** *4* (5), 1800638.

162. Kozbial, A.; Guan, W.; Li, L., Manipulating the molecular conformation of a nanometer-thick environmentally friendly coating to control the surface energy. *Journal of Materials Chemistry A* **2017,** *5* (20), 9752-9759.

163. Wang, Y.; You, C.; Kowall, C.; Li, L., A Nanometer-Thick, Mechanically Robust, and Easy-to-Fabricate Simultaneously Oleophobic/Hydrophilic Polymer Coating for Oil–Water Separation. *Industrial & Engineering Chemistry Research* **2018,** *57* (45), 15395-15399.

164. Cao, L.; Hu, H.-H.; Gao, D., Design and fabrication of micro-textures for inducing a superhydrophobic behavior on hydrophilic materials. *Langmuir* **2007,** *23* (8), 4310-4314.

165. Tuteja, A.; Choi, W.; Ma, M.; Mabry, J. M.; Mazzella, S. A.; Rutledge, G. C.; McKinley, G. H.; Cohen, R. E., Designing superoleophobic surfaces. *Science* **2007,** *318* (5856), 1618-1622.

166. Wenzel, R. N., Resistance of solid surfaces to wetting by water. *Industrial & Engineering Chemistry* **1936,** *28* (8), 988-994.

167. Lafuma, A.; Quéré, D., Superhydrophobic states. *Nature materials* **2003,** *2* (7), 457-460.

168. He, G. S.; Tan, L.-S.; Zheng, Q.; Prasad, P. N., Multiphoton absorbing materials: molecular designs, characterizations, and applications. *Chemical reviews* **2008,** *108* (4), 1245-1330.

169. Xing, J.-F.; Zheng, M.-L.; Duan, X.-M., Two-photon polymerization microfabrication of hydrogels: an advanced 3D printing technology for tissue engineering and drug delivery. *Chemical Society Reviews* **2015,** *44* (15), 5031-5039.

170. Pawlicki, M.; Collins, H. A.; Denning, R. G.; Anderson, H. L., Two-photon absorption and the design of two-photon dyes. *Angewandte Chemie International Edition* **2009,** *48* (18), 3244-3266.

171. Liu, T.; Kim, C.-J., Turning a surface superrepellent even to completely wetting liquids. *Science* **2014,** *346* (6213), 1096-1100.

172. Murakami, D.; Jinnai, H.; Takahara, A., Wetting transition from the Cassie–Baxter state to the Wenzel state on textured polymer surfaces. *Langmuir* **2014,** *30* (8), 2061-2067.

173. Werber, J. R.; Osuji, C. O.; Elimelech, M., Materials for next-generation desalination and water purification membranes. *Nature Reviews Materials* **2016,** *1* (5), 1-15.

174. Xue, Z.; Wang, S.; Lin, L.; Chen, L.; Liu, M.; Feng, L.; Jiang, L., A novel superhydrophilic and underwater superoleophobic hydrogel-coated mesh for oil/water separation. *Advanced Materials* **2011,** *23* (37), 4270-4273.

175. Xue, Z.; Cao, Y.; Liu, N.; Feng, L.; Jiang, L., Special wettable materials for oil/water separation. *Journal of Materials Chemistry A* **2014,** *2* (8), 2445-2460.

176. Lv, J.; Gong, Z.; He, Z.; Yang, J.; Chen, Y.; Tang, C.; Liu, Y.; Fan, M.; Lau, W.-M., 3D printing of a mechanically durable superhydrophobic porous membrane for oil–water separation. *Journal of Materials Chemistry A* **2017,** *5* (24), 12435-12444.

177. Femmer, T.; Kuehne, A. J.; Torres-Rendon, J.; Walther, A.; Wessling, M., Print your membrane: Rapid prototyping of complex 3D-PDMS membranes via a sacrificial resist. *Journal of membrane science* **2015,** *478*, 12-18.

178. Yuan, S.; Strobbe, D.; Kruth, J.-P.; Van Puyvelde, P.; Van der Bruggen, B., Super-hydrophobic 3D printed polysulfone membranes with a switchable wettability by self-assembled candle soot for efficient gravity-driven oil/water separation. *Journal of Materials Chemistry A* **2017,** *5* (48), 25401-25409.

179. Chen, Y.; Wang, N.; Guo, F.; Hou, L.; Liu, J.; Liu, J.; Xu, Y.; Zhao, Y.; Jiang, L., A Co 3 O 4 nano-needle mesh for highly efficient, high-flux emulsion separation. *Journal of Materials Chemistry A* **2016,** *4* (31), 12014-12019.

180. Zhang, W.; Shi, Z.; Zhang, F.; Liu, X.; Jin, J.; Jiang, L., Superhydrophobic and superoleophilic PVDF membranes for effective separation of water-in-oil emulsions with high flux. *Advanced Materials* **2013,** *25* (14), 2071-2076.

181. Zeng, M.; Peng, B.; Ybanez, C.; Tan, N. W.; Deeb, E. A.; Bordovsky, E.; Choi, C.-H.; Echols, I.; Nguyen, A.; Ye, A., High-flux underwater superoleophobic hybrid membranes for effective oil–water separation from oil-contaminated water. *RSC advances* **2017,** *7* (15), 9051-9056.

182. Low, Z.-X.; Chua, Y. T.; Ray, B. M.; Mattia, D.; Metcalfe, I. S.; Patterson, D. A., Perspective on 3D printing of separation membranes and comparison to related unconventional fabrication techniques. *Journal of Membrane Science* **2017,** *523*, 596-613.

183. Melo, L.; Bott, T. R.; Bernardo, C. A., *Fouling science and technology*. Springer Science & Business Media: 2012; Vol. 145.

184. Abedin, M. Z.; Kim, N.-H., An experimental study on accelerated fouling of aluminum oxide and ferric oxide particles in internally enhanced tubes. *Journal of Mechanical Science and Technology* **2016,** *30* (12), 5707-5714.

185. Walker, M. E.; Safari, I.; Theregowda, R. B.; Hsieh, M.-K.; Abbasian, J.; Arastoopour, H.; Dzombak, D. A.; Miller, D. C., Economic impact of condenser fouling in existing thermoelectric power plants. *Energy* **2012,** *44* (1), 429-437.

186. Jun, S.; Puri, V., Fouling models for heat exchangers in dairy processing: a review. *Journal of food process engineering* **2005,** *28* (1), 1-34.

187. Bohnet, M., Influence of the transport properties of the crystal/heat transfer surface interfacial on fouling behavior. *Chemical Engineering & Technology: Industrial Chemistry-Plant Equipment-Process Engineering-Biotechnology* **2003,** *26* (10), 1055-1060.

188. Webb, R. L.; Li, W., Fouling in enhanced tubes using cooling tower water: Part I: long-term fouling data. *International Journal of Heat and Mass Transfer* **2000,** *43* (19), 3567-3578.

189. Li, W.; Webb, R. L., Fouling in enhanced tubes using cooling tower water: Part II: combined particulate and precipitation fouling. *International Journal of Heat and Mass Transfer* **2000,** *43* (19), 3579-3588.

190. Trivedi, B., *Maleic anhydride*. Springer Science & Business Media: 2013.

191. De Roover, B.; Sclavons, M.; Carlier, V.; Devaux, J.; Legras, R.; Momtaz, A., Molecular characterization of maleic anhydride-functionalized polypropylene. *Journal of Polymer Science Part A: Polymer Chemistry* **1995,** *33* (5), 829-842.

192. Eren, T.; Küsefoğlu, S. H.; Wool, R., Polymerization of maleic anhydride–modified plant oils with polyols. *Journal of applied polymer science* **2003,** *90* (1), 197-202.

193. Horie, T.; Sumino, M.; Tanaka, T.; Matsushita, Y.; Ichimura, T.; Yoshida, J.-i., Photodimerization of maleic anhydride in a microreactor without clogging. *Organic Process Research & Development* **2010,** *14* (2), 405-410.

194. Conn, J. B.; Kistiakowsky, G.; Roberts, R. M.; Smith, E. A., Heats of organic reactions. XIII. Heats of hydrolysis of some acid anhydrides. *Journal of the American Chemical Society* **1942,** *64* (8), 1747-1752.

195. Li, X.; Ho, B.; Zhang, Y., Selective aerobic oxidation of furfural to maleic anhydride with heterogeneous Mo–V–O catalysts. *Green Chemistry* **2016,** *18* (10), 2976-2980.

196. Rundlöf, T.; Mathiasson, M.; Bekiroglu, S.; Hakkarainen, B.; Bowden, T.; Arvidsson, T., Survey and qualification of internal standards for quantification by 1H NMR spectroscopy. *Journal of pharmaceutical and biomedical analysis* **2010,** *52* (5), 645-651.

197. Wojcieszak, R.; Santarelli, F.; Paul, S.; Dumeignil, F.; Cavani, F.; Gonçalves, R. V., Recent developments in maleic acid synthesis from bio-based chemicals. *Sustainable Chemical Processes* **2015,** *3* (1), 9.

198. Quéré, D.; Azzopardi, M.-J.; Delattre, L., Drops at rest on a tilted plane. *Langmuir* **1998,** *14* (8), 2213-2216.

199. Gao, L.; McCarthy, T. J., "Artificial Lotus Leaf" Prepared Using a 1945 Patent and a Commercial Textile. *Langmuir* **2006,** *22* (14), 5998-6000.

200. Raj, R.; Enright, R.; Zhu, Y.; Adera, S.; Wang, E. N., Unified Model for Contact Angle Hysteresis on Heterogeneous and Superhydrophobic Surfaces. *Langmuir* **2012,** *28* (45), 15777-15788.

201. Gao, L.; McCarthy, T. J., How Wenzel and Cassie Were Wrong. *Langmuir* **2007,** *23* (7), 3762-3765.

202. Eral, H. B.; 't Mannetje, D. J. C. M.; Oh, J. M., Contact angle hysteresis: a review of fundamentals and applications. *Colloid. Polym. Sci.* **2012,** *291* (2), 247-260.

203. Kozbial, A.; Trouba, C.; Liu, H.; Li, L., Characterization of the intrinsic water wettability of graphite using contact angle measurements: effect of defects on static and dynamic contact angles. *Langmuir* **2017,** *33* (4), 959-967.